Dominis

# Impact of manufacturing tolerances on propeller performance

## Investigation 1: 2D foil section in the rectilinear flow

**Project no.** **RD36**

**Report no.:** **RD36-TC-01**

**Contract no.: T8009-180256/001/XLV**

**Prepared for: The Innovation Centre of Transport Canada**

*Financial contribution from*
*Avec le financement de*

Transport Canada Transports Canada

MEMORIAL UNIVERSITY

Canada

Dominis Engineering Ltd.
5515 Canotek Rd., Unit 15
Gloucester, Ontario
Canada K1J 9L1

Tel: (613) 747-0192
Fax: (613) 746-3321
Web site: www.dominis.ca

| | |
|---|---|
| Prepared by: | Dominis Engineering Ltd.<br>5515 Canotek Rd., Unit 15<br>Gloucester, Ontario<br>K1J 9L1<br><br>tel.: (613) 747-0193<br>fax.: (613) 746-3321<br>web site: www.dominis.ca |
| Project title: | Impact of manufacturing tolerances on propeller performance<br>Investigation 1: 2D Foil section in the rectilinear flow |
| Project no.: | RD36 |
| Report no.: | RD36-TC-01 |
| Revision no.: | Final report |
| Submitted to: | Denis Tran, Project Manager<br>Innovation Centre of Transport Canada<br>Place de Ville, Tower C, 25th Floor<br>330 Sparks Street<br>Ottawa, Ontario<br>K1A 0N5 |
| Submission date: | 21 March 2022 |
| Approved by: | S. (Bodo) Gospodnetic, P. Eng. |

Dominis

**Notice:** This report reflects the views of the authors and not necessarily of the Innovation Centre of Transport Canada.

**Acknowledgments:**

The financial support for this project and advice of the Innovation Centre of Transport Canada is gratefully acknowledged.

The generous technical support, advice and encouragement of Dr. James L. Kennedy of Ottawa are gratefully acknowledged.

A preliminary CFD investigation of the behaviour of leading-edge defects was carried out by Dr. David Hally, Defence Scientist at DRDC-Atlantic Research Centre. His guidance and advice in the initial planning of this research project are gratefully acknowledged.

We also gratefully acknowledge the support and advice of R. Adm. (ret.) Simon Page, ADM Defence and Marine Procurement, who encouraged us to pursue and continue this research initiative in 2018 in his former capacity as DGMEPM.

## Executive Summary

Anthropogenic underwater radiated noise is recognized as a worldwide problem and a significant portion of this is generated by ships. It has been shown that at higher speeds propeller noise is most important mainly due to cavitation.

Ship propellers are typically manufactured to meet the ISO 484 (International Organization for Standards) propeller manufacturing tolerance standards. The majority of propellers manufactured today are manually finish-ground from castings that have been rough machined on CNC (Computer Numerically Controlled) milling machines. Robotic and manual grinding of propeller surfaces introduces inaccuracies and deviations from design, which could lead to degradation of propeller performance in terms of efficiency, cavitation and noise. The leading-edge is a very challenging area to manufacture accurately yet it has a strong influence on sheet, streak and vortex cavitation.

There is a lack of scientific literature in the public domain that deals with the subject of manufacturing tolerances of propellers. This gap in scientific knowledge encouraged Dominis Engineering to initiate a thorough investigation of propeller manufacturing tolerances. This report describes the first part of that investigation which was to evaluate the cavitation performance degradation between a typical propeller blade section (“as-designed”) and that same section with a geometric defect (“as-built”).

Propeller cavitation performance will be evaluated in terms of change in cavitation inception speed. The geometric defect examined was a sharp-edged flat adjacent to the leading-edge with a maximum deviation of 0.5 mm from the “as designed” form. This is at the limit of the most stringent tolerances specified by the ISO 484 standard. Typical propeller manufacturing processes lend themselves to creating such defects and they have been observed on propellers in service.

Computational Fluid Dynamics (CFD) methods provided minimum pressure coefficients on the sections from which cavitation performance was predicted. Experimental measurements of cavitation inception on the sections were also made in a cavitation tunnel. The minimum pressure coefficients and Cavitation Numbers for the sections were developed and measured over a wide range of angles of attack and presented in the form of cavitation buckets. The sections’ relative performance was evaluated in terms of the change in cavitation inception speed if these results were applied to a ship propeller.

The results of this investigation into the effect of leading-edge flats on the cavitation of this typical propeller blade section are as follows:

- CFD calculations predict a reduction in the width of the cavitation bucket for a typical propeller blade section with a 0.5 mm defect on the leading-edge. This result provides a warning that such defects have the potential to cause earlier cavitation on propellers and that this subject requires further investigation.
- Cavitation inception was observed visually on models of perfect and defective versions of the typical propeller blade section. The maximum observed loss in cavitation inception speed due to a 0.5 mm defect on the leading-edge was 35%.
- The 0.5 mm defect tested is one of the tightest ISO 484 propeller manufacturing tolerances and it has been demonstrated experimentally that it affects cavitation inception significantly and detrimentally on a typical propeller blade section.

The experimental results obtained so far show that current widely accepted propeller manufacturing tolerances as stated in the ISO 484 standard need to be thoroughly evaluated.

Dominis

## TABLE OF CONTENTS

**List of Figures**

Dominis

## List of Tables

## Glossary of Abbreviations

| | |
|---|---|
| CFD | Computational Fluid Dynamics |
| CNC | Computer Numerically Controlled |
| DRDC-Atlantic | Defence Research and Development Canada – Atlantic Research Centre |
| DTMB | David Taylor Model Basin |
| ISO | International Organization for Standardization |
| MUN | Memorial University of Newfoundland |
| NAVSEA | Naval Sea Systems Command |
| NACA | National Administrative Committee for Aeronautics |
| NSRDC | Naval Ship Research and Development Center |
| RANS | Reynolds Averaged Navier-Stokes (equations) |
| TRANSOM | RANS CFD code developed by DRDC-Atlantic |

## Definitions of Terms

| | |
|---|---|
| As-built | This expression is used to describe objects which are manufactured to comply with a specific manufacturing tolerance. Measured dimensions of these objects vary from the design dimensions but are within the allowable tolerance window. Also referred to as a “defective” or (0.5 mm defect) section. |
| As-designed | This expression is used to describe objects with their design dimensions specified with tolerances of +/- 0.000 mm. Also referred to as a “perfect” or (0.0 mm defect) section. |
| Back of the blade | is the side of the propeller blade or blade section where there is a decrease in water pressure. This side of the propeller blade is also known as the suction side (SS). |
| Best practice setting | is a set of parameters for which research and experience have shown to produce optimum results. |

Dominis

| | |
|---|---|
| Cavitation inception speed | is the speed of the ship at which propeller cavitation starts. |
| Chord line | is the straight line joining the LE to TE of a 2D section. |
| Face of the blade | is the side of the propeller blade or blade section where there is an increase in water pressure. This side of the propeller blade is also known as the pressure side (PS) |
| Leading-edge (LE) | is the edge of the propeller section which enters first into the water |
| Propeller cavitation | is a phenomenon that occurs when the pressure on the propeller blade surface becomes lower than the vapour pressure of water |
| Rectilinear flow | The onset flow is in a straight line |
| Trailing-edge (TE) | is the edge of the propeller section which exits last from the water |

**Nomenclature**

| | |
|---|---|
| a | parameter in the NACA a – series of mean lines |
| c | chord length |
| f | maximum camber |
| $p_a$ | air pressure |
| t | section thickness |
| $C_p$ | pressure coefficient |
| P | local static pressure on section |
| $P_\infty$ | free stream static pressure |
| U | velocity of section |
| v | kinematic viscosity of water |
| ρ | density of water |

# 1.0 INTRODUCTION

The behaviour of the 2D foil section in rectilinear flow described in this report is part of the comprehensive investigation under the working title of “Impact of manufacturing tolerances on propeller performance”. The work described in this report was supported by Transport Canada

## 1.1 Project overview: Impact of manufacturing tolerances on propeller performance

Ship propellers are typically manufactured to meet the ISO 484 tolerance standards. The majority of propellers manufactured today are manually finish-ground from castings that have been rough machined on CNC milling machines. Robotic and manual grinding of propeller surfaces introduces inaccuracies and deviations from design, which could lead to degradation of propeller performance in terms of efficiency, cavitation and noise. The leading-edge (LE) is a very challenging area to manufacture accurately yet it has a strong influence on sheet, streak and vortex cavitation.

The project compares “as-built” propeller blade sections with their ideal “as-designed” counterpart to elucidate the effects of manufacturing defects on cavitation and propulsive performance. This study is investigating the effect of sharp-edged flat regions near the LE, which are within the tolerances of ISO 484 class S. The project is organised into three investigations each carried out on progressively more complex configurations starting with a simple 2-dimensional foil geometry and ending with a full propeller rotating geometry. The investigations are being carried out using RANS CFD simulations supported by experiments with physical models in a cavitation tunnel. For details about project organization see Appendix A.

## 1.2 Underwater radiated noise

Anthropogenic underwater radiated noise is now being recognized as a worldwide problem. A significant portion of underwater noise is generated by ships. Continued growth in the number of ships, quantities of goods transported, and distances travelled will significantly increase the total volume of noise generated by the global shipping fleet. Projections suggest that by the year 2030, the underwater noise level could increase by as much as a factor of 1.9 of the current level [1]. The relationship between the typical ocean ambient noise and modern levels of shipping noise is illustrated in Figure 1. Underwater noise from shipping is increasingly being recognized as a significant and omnipresent pollutant with the potential to impact marine ecosystems on a global scale [2]. The current Covid-19 pandemic crisis together with the economic slowdown that the crisis precipitated will have only a temporary effect on global shipping. The trend of underwater noise increase is expected to continue after the conditions return to the “new normal” after the pandemic.

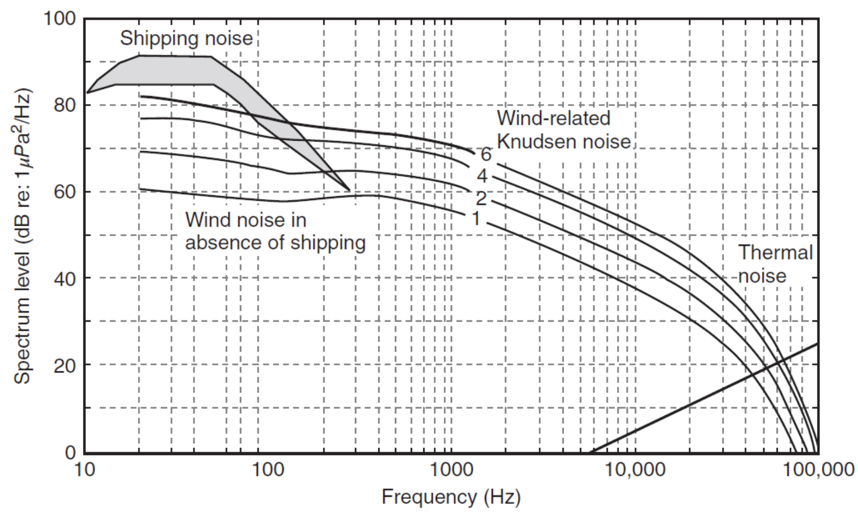


Figure 1: Ocean ambient noise and modern levels of shipping noise [1]

The underwater radiated noise of a ship is caused mainly by the propeller and the main machinery. The European Union’s collaborative research project AQUO (Achieve QUieter Oceans) has provided valuable insight into the relative contribution of each source of noise generated by different types of ships [3]. One of the objectives of that project was to predict and measure underwater noise generated by several types of ships. That study showed that at lower speeds machinery noise is the most important source of noise, however, at higher speeds propeller noise is more important mainly due to cavitation. A significant conclusion of the study is that for ferries and cruise vessels at normal operating speeds, cavitation is the most important source of noise. Research findings of the AQUO project for ferries and cruise vessels are summarized in Figures 2 and 3, which contain graphs of the relative distribution of noise generated by machinery, propeller and cavitation at four different ship speeds.

The noise levels from a ship jump substantially when propeller cavitation begins [4, #10.2]. The ship speed, at which the propeller cavitation starts is denoted as the cavitation inception speed [4, #9.4] and it is a fair but simple measure of a condition beyond which noise can become unacceptable.

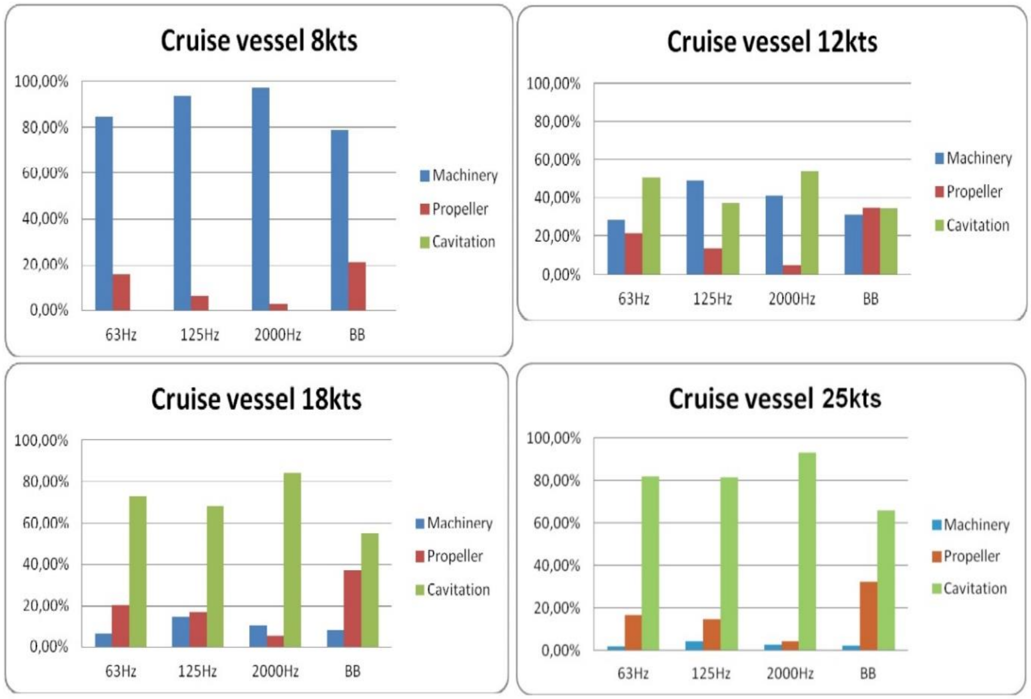


Figure 2: Relative noise levels generated by cruise vessels [3]

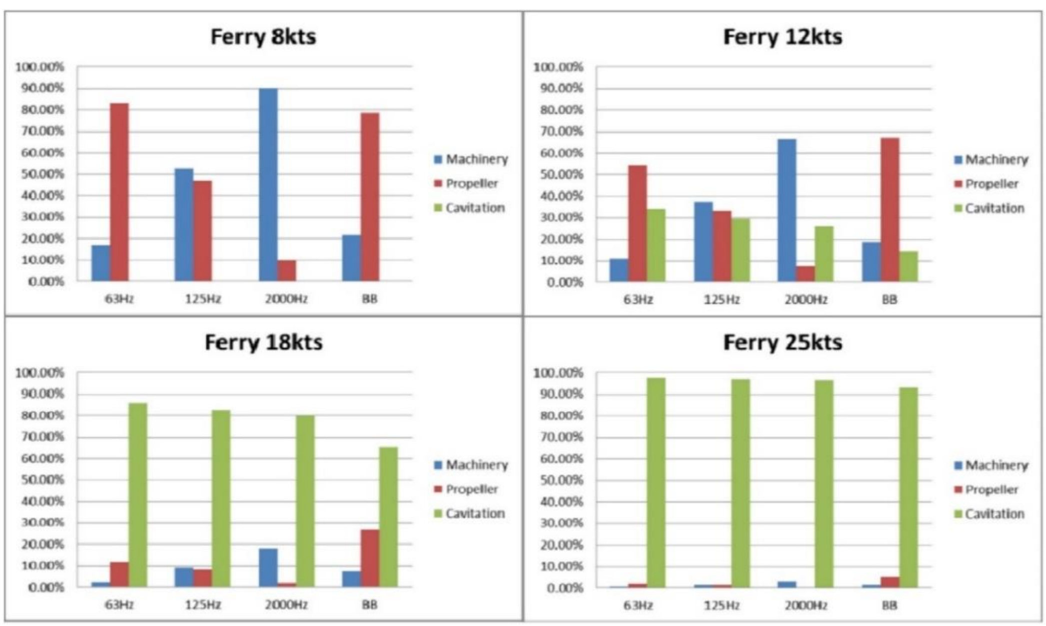


Figure 3: Relative noise levels generated by ferries [3]

Cavitation is frequently described by how it looks and can be divided into three categories: Bubble cavitation; Sheet cavitation and Vortex cavitation [4, #9.2]. A lot is known about how propeller geometries can be varied to control bubble cavitation. Inception speeds for bubble cavitation are usually pushed above a ship's top speed. Sheet cavitation starts at locations along the leading-edge of a propeller blade and spreads like a sheet across the blade surface [5, #6.7; 6, #6]. It could be expected at the highest two speeds of Figures 2 and 3, and perhaps even in the 2nd lowest speed. Vortex cavitation typically starts at the propeller tip and hub and trails downstream. Tip vortex cavitation is often, but not always, the first type of cavitation to form, i.e. it would have the lowest cavitation inception speed [4, #9.2].

### 1.3 Design and manufacturing of propellers

Ship propellers are created by a set of complex design, manufacturing and inspection processes. The ultimate objective of a propeller is to propel a vessel with a desired speed, absorbing specified engine power at a required rate of rotation. This objective should be achieved with optimum efficiency, causing the least amount of noise and vibrations, but also at the lowest possible cost. As with all complex engineering systems, the creation of a new ship propeller is affected by deviations from the ideal design solution due to imperfections in input and experimental data, approximations inherent in the mathematical techniques used in propeller design and manufacturing imperfections inherent in the chosen propeller manufacturing process.

Propellers are typically manufactured today as follows [7, 8]:

- All surfaces of propeller castings are rough machined using CNC milling machines.
- Propeller blade surfaces are finished using robotic or manual grinding.
- Blade edges and tips, the most sensitive parts of a propeller's geometry, are made to conform to templates of their required form using manual grinding.

Robots can grind only flat or gently curved surfaces and they are not as accurate as CNC milling machines. Hand grinding is time-consuming, error-prone and non-repeatable. Robotic and hand grinding could easily introduce unwanted deviations from the design specifications of hydrodynamic surfaces, in particular on the edges and tips of propeller blades. These deviations can result in degradation of propeller propulsion, cavitation and noise performance.

During the past three decades, there have been remarkable improvements in the design techniques for ship propellers. Shipowners are under increasing financial and ecological pressure to improve their propellers' hydrodynamic performance. Propeller designers have responded by more precisely designing propellers to avoid or delay their hydrodynamic limits. This, in turn, has required manufacturers to produce propellers that more closely meet the designers' intent.

During the same period, there have also been tremendous improvements in propeller manufacturing techniques through the introduction of multi-axis CNC milling machines and the development of high-speed machining. Improvements in measurement and inspection of propellers are mainly due to the development of laser scanning systems and large volume gantry CMM (Coordinate Measuring Machines).

### 1.4 Manufacturing tolerances for propellers

Manufacturing tolerances for new ship propellers are governed by two organizations: ISO which controls manufacturing standards for commercial ships and European navies' ship construction, and NAVSEA (Naval Sea Systems Command) which controls manufacturing standards for US Navy's ship construction.

The ISO 484 standard for manufacturing tolerances for ship propellers was established in 1981 by adopting an ISO Recommendation prepared in 1966. ISO 484-1 [9] applies to propellers with diameters greater than 2.5 m, while ISO 484-2 [10] applies to propellers with diameters from 0.8 m to 2.5 m. There are four classes of tolerances in each standard. Each tolerance class is intended for a certain type of vessel. Among the four classes, class S is the most stringent. A list of vessel types and their intended ISO manufacturing tolerance classes is presented in Table 1.

The ISO 484 standard was originally established to allow a significant number of manufacturing companies to manufacture and finish propellers, and that these same companies could establish, by using simple measurement equipment, whether the propellers they have manufactured are within the ISO tolerances. Although the ISO propeller manufacturing standard is widely accepted, it has not kept pace with the improvements in propeller design specifications, manufacturing and inspection. The standard has remained virtually unchanged since the original ISO Recommendation of 1966. Minor cosmetic changes were incorporated in the last update in 2015. At present, ISO 484 seems antiquated.

| ISO 484-1 tolerance class | Ship type |
|---|---|
| S | Naval vessels such as frigates and destroyers<br>Cruise vessels<br>High speed ferries<br>Research vessels<br>Special purpose merchant vessels |
| 1 | General merchant vessels<br>Deep sea trawlers<br>Tugs<br>Ferries<br>Naval auxiliary vessels |
| 2 | Low - power craft<br>Low - speed craft<br>Inshore fishing vessels<br>Work boats |
| 3 | Similar types as Class 2 |

Table 1: ISO tolerance classes for vessel types [4, #25]

NAVSEA propeller manufacturing tolerances originally issued in 1969 are described in the Standard Propeller Drawing no. 810-4435837, Rev. B [11]. There are 4 classes of tolerances each applicable to a particular type of navy vessel. NAVSEA standard is somewhat tighter in geometry precision requirements but the main difference between ISO and NAVSEA standards is the number of surface points on the propeller which have to be measured during an inspection. NAVSEA Standard Propeller Drawing was last updated in 2004.

NAVSEA class I and ISO class S standards have similar demands on precision for most main propeller parameters except for surface roughness and leading-edge form with NAVSEA tolerances being slightly more stringent. NAVSEA standard also requires more points to be measured for propeller inspection than ISO 484. See Table 2 for a comparison of tolerances for LE form and surface roughness between NAVSEA class I and ISO 484-1 class S.

| Propeller dimension | NAVSEA class I | | ISO 484-1 class S | |
|---|---|---|---|---|
| | Imperial | Metric | Metric | Imperial |
| LE form | ±0.015 inch | ±0.38 mm | ±0.50 mm | ±0.020 inch |
| Surface roughness | 63 μinch | 1.6 μm | 2 μm | 79 μinch |

Table 2: NAVSEA class I [11] vs. ISO 484-1 class S [9] tolerances

### 1.5 Project background and preliminary investigation

A survey of scientific literature in the public domain by Dominis in 2017 found only three scientific papers that dealt with the subject of manufacturing tolerances of propellers. All three of these papers originated at Lips – Wartsila in the Netherlands and were published in 1977 [12], 1984 [13] and 2017 [7]. Two studies of tolerance impact on B-series propellers by Dr. James L. Kennedy of Ottawa [14, 15] provided additional insight and importance of the propeller manufacturing tolerances.

Intrigued by the lack of public domain scientific literature that deals with a manufacturing tolerance of propellers and encouraged by the insight gained by two studies on B-series propellers, Dominis has begun to investigate the effects of manufacturing variations at the leading-edges (LE) prompted by two factors:

1) The LE geometry is highly susceptible to manual grinding errors and
2) Basic two-dimensional foil theory points to the sensitivity of the LE pressures to geometric variations. [16].

There are an infinite variety of defects that could be examined. The tightest dimensional tolerances (apart from roughness) on NAVSEA and ISO standards are reserved for the form of the leading-edge, undoubtedly reflecting propeller manufacturers' understanding of the criticality of that region. A flat surface, rather than the desired curved outline, is likely as bad a defect as could be expected, is quite possible given the grinders used, and is what has been observed on a propeller used on an actual vessel in service.

Typical "real-life" defects on the LE of a propeller blade are shown in Figure 4. It is not known if the defects shown in Figure 4 are the results of the original manual grinding of the propeller blade edges or if they are the result of cleaning and polishing of the propeller blade to remove fouling. Regardless of the origin of these flats on the LE, they were found on a propeller used on an operational ship. LE flats shown in Figure 4 were measured and these measurements were used to create 3 versions of defective LE forms used in this study. The location of these flat defects in the current study is fairly typical of sections where LE cavitation is observed on propellers.

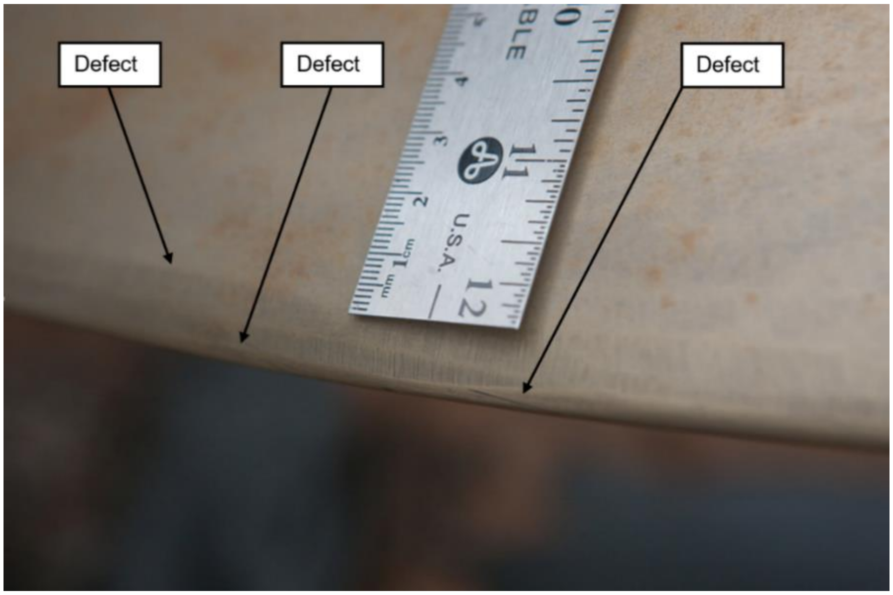


Figure 4: Leading-edge defects on a propeller blade in service.
Photo courtesy of DRDC-Atlantic

The decision was therefore made to initiate the investigation into the impact of manufacturing tolerances on LE of 2D propeller blade sections. According to the ISO 484 standard, the form of the LE contour, when measured with a one-part template, cannot deviate from the design by more than 0.5 mm for class S. CFD simulations using a typical propeller blade section (NACA-66) foil with 1 m chord were conducted by Dr. David Hally of DRDC-Atlantic (Defence Research and Development Canada) [16, 17]. These exploratory CFD simulations demonstrated that small deviations (even smaller than the ISO class S requirements) from the design geometry can have significant effects on the flow near the LE and the pressures that cause cavitation there. Figures 5A and 5B show pressure coefficient distributions and Figure 6 shows pressure peaks near the LE caused by small deviations from true foil form. The relation between pressure coefficient and velocity of the section is defined by the following expression:

$$C_p = \frac{P - P_\infty}{\frac{1}{2}\rho U^2}$$

| | | | |
|---|---|---|---|
| where: | $P$ | = | local static pressure on the section |
| | $P_\infty$ | = | free stream static pressure |
| | $\rho$ | = | density of water |
| | $U$ | = | velocity of section |

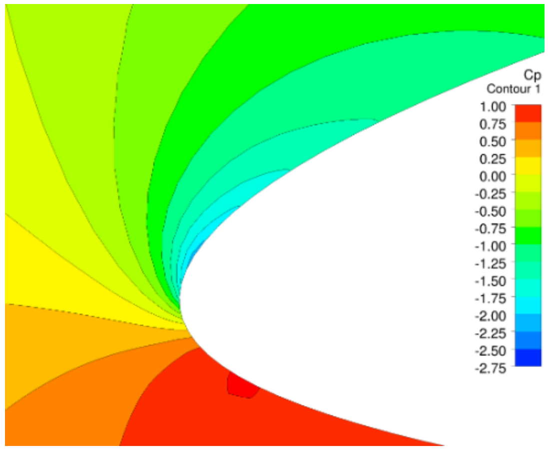


Figure 5A: Pressure near the leading-edge, “as-designed”, no defects, angle 2° [16]

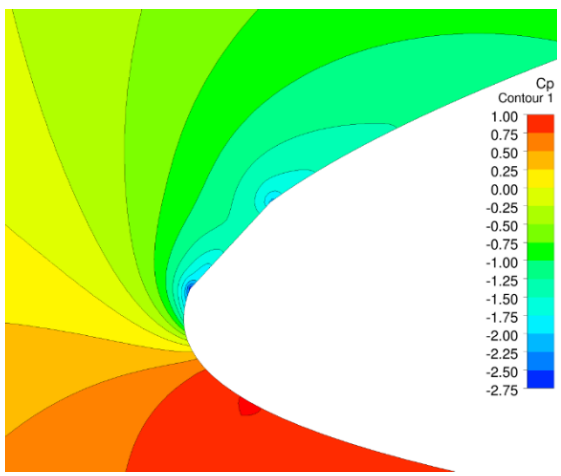


Figure 5B: Pressure near the leading-edge, “as-built”, 0.094mm defect, angle 2° [16]

From pressure peaks in Figure 6, we can calculate the ratio of cavitation inception speeds from the highest points on each of the $C_p$ curves for an ideal (“as-designed”) section and a section with LE flat (“as-built”). For example:

$C_p$ (no flat) = 2.1

$C_p$ (0.25 mm defect) = 2.8

$$Ratio = \sqrt{\frac{2.1}{2.8}} = 0.87$$

Dominis

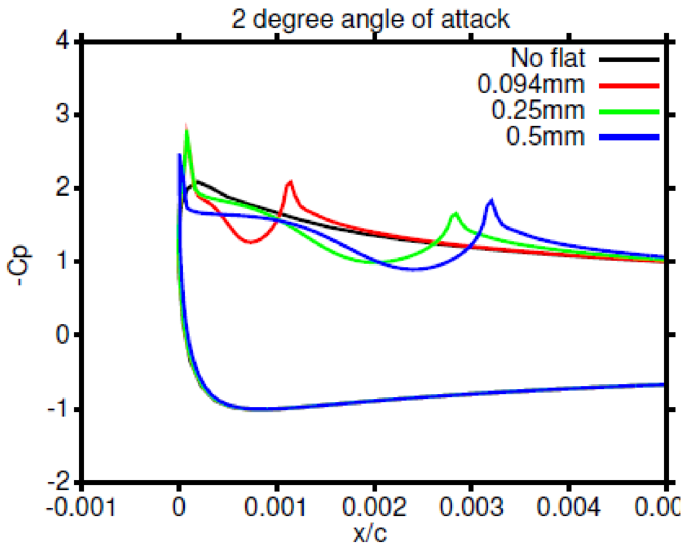


Figure 6: Pressure peaks near the leading-edge. The angle of attack 2°, “as-designed” no flat, “as-built” with 0.094 mm, 0.25 mm and 0.5 mm LE defect. [16]

Cavitation on that section with that flat on the LE will begin at 87% of the cavitation inception speed of the designed section without the flat, or for example at 8.7 knots instead of 10 knots. These preliminary findings suggest that the propeller manufacturing tolerances as specified by ISO 484 should be thoroughly investigated.

## 2.0 PROJECT OBJECTIVE

The objective of this research project was to determine cavitation performance degradation between a typical ideal-geometry propeller blade section (“as-designed”) and that same section with compromised geometries (“as-built”). Propeller cavitation performance was evaluated in terms of change in cavitation inception speed. Geometries of the compromised propeller blade sections studied had sharp-edged LE flat defects which are within the limits of the most accurate manufacturing tolerances specified by ISO 484, that is, class S.

## 3.0 SCOPE OF WORK

The investigation was carried out using Reynolds Averaged Navier-Stokes (RANS) CFD simulations. These CFD simulations computed the cavitation buckets for one ideal geometry and three defective geometry sections. The CFD simulations were performed by graduate students at the Memorial University of Newfoundland (MUN) using STAR-CCM+ and defence scientists at DRDC-Atlantic using ANSYS CFX and TRANSOM software systems. The methods will be validated against known solutions and the results of the solution methods will be compared. The cavitation degradation results for the different geometries will give their relative cavitation inception speeds.

Further CFD simulations of the physical model of foils in a cavitation tunnel were carried out by MUN to provide guidance for the experimental phase of the study.

Results of CFD simulation were compared with the results of experiments with a physical model in the cavitation tunnel at the Brodarski Institut in Zagreb, Croatia. A single model incorporating both the ideal and a defective foil geometry was used for cavitation tunnel experiments. The cavitation was observed visually. The cavitation inception speed was recorded for a range of angles of attack for both the ideal and defective portion of the foil model.

## 4.0 2D FOIL CFD INVESTIGATION IN RECTILINEAR FLOW

The 2D foil cavitation data for "as-designed" sections is well known and is used by propeller designers to ensure high sheet cavitation inception speeds. What is unknown is the corresponding data for defective sections. This investigation will attempt to fill this gap in scientific knowledge.

### 4.1 2D foil CFD simulations

The DTMB modified NACA-66 (a=0.8) foil with t/c = 0.0416 and f/c = 0.014 was selected for this study [19]. Coordinates of the foil are given in Appendix B. This geometry is fairly typical of a propeller blade section at outer radii and it is specifically that at 0.7 radius of the propeller on the "KCS" ship model [20, 21, 22, 23, 24, 25, 26], scaled to have a chord length of 1 m.

CFD simulations were carried out by MUN using the steady RANS solver in STAR-CCM+ on structured grids for 2D foils with and without LE defects in an infinite field. Additional CFD simulations were performed on a NACA-66 (a=0.8) foil with t/c = 0.2 and f/c = 0.02 to compare the steady RANS numerical results with potential-flow solutions of Terry Brocket [19] and numerical solutions carried out by David Hally [27] at DRDC using ANSYS CFX and TRANSOM software systems.

### 4.2 Test foils

The coordinate system for all 2D CFD simulations is depicted in Figure 7. The origin, O of the coordinate system is at the leading-edge of the foil. The x-axis starts at the leading-edge (LE) and runs along the chord line towards the trailing-edge (TE). The y-axis is perpendicular to the x-axis.

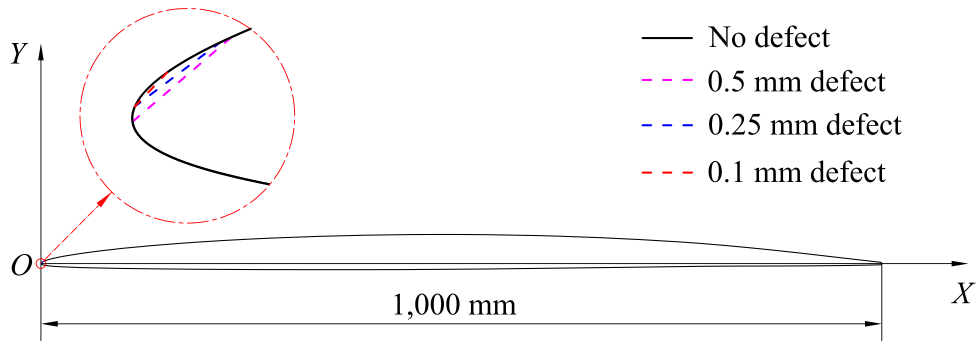


Figure 7: NACA-66 foil (a=0.8, f/c=0.014, t/c=0.0416) with and without defects

Three sizes of LE defects that are within class S tolerance of the ISO 484-1 standard were selected (see Figure 7). According to ISO 484 standard, class S tolerance for leading-edge is 0.5 mm for a 1-part template or 0.25 mm for a 3-part template.

### 4.3 Leading-edge defects

Metal templates of a sort shown in Figure 8 are used for measurement and verification of compliance of manufactured leading-edge form to designed leading-edge form.

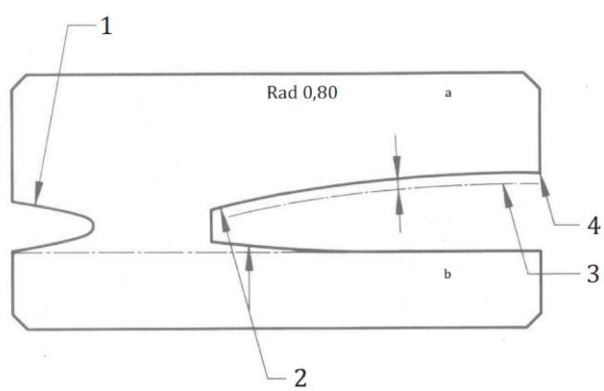


Figure 8: 3-part LE template, ISO 484-1 [9]

Dominis

Drawing in Figure 9 shows the application of the leading-edge template to an "as-designed" leading-edge without defect. Drawing in Figure 10 shows the application of the leading-edge template to an "as-built" leading-edge with a 0.5 mm defect.

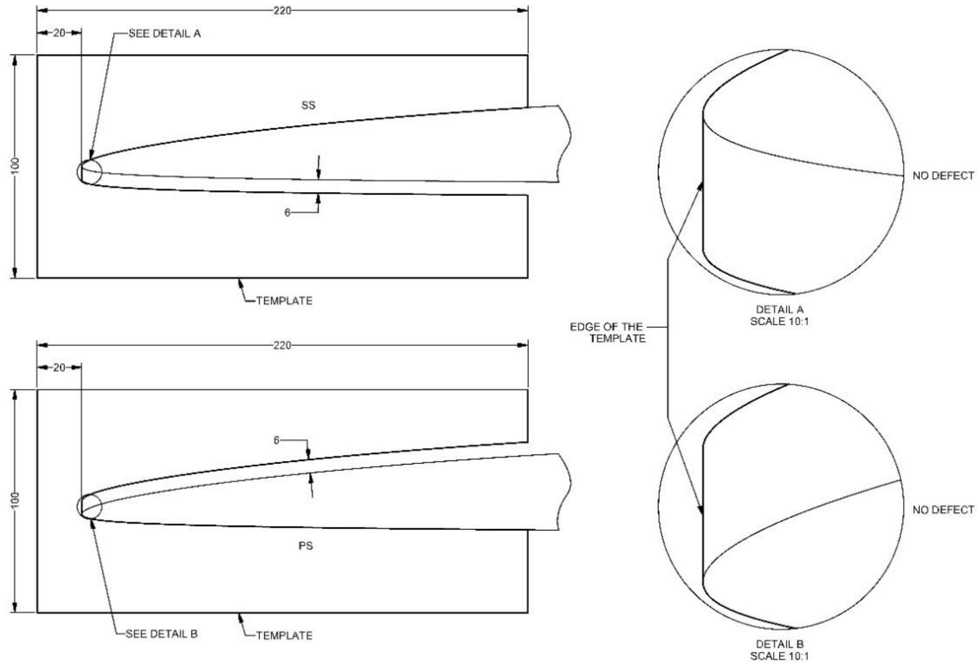


Figure 9: Application of the template to a leading-edge without defect

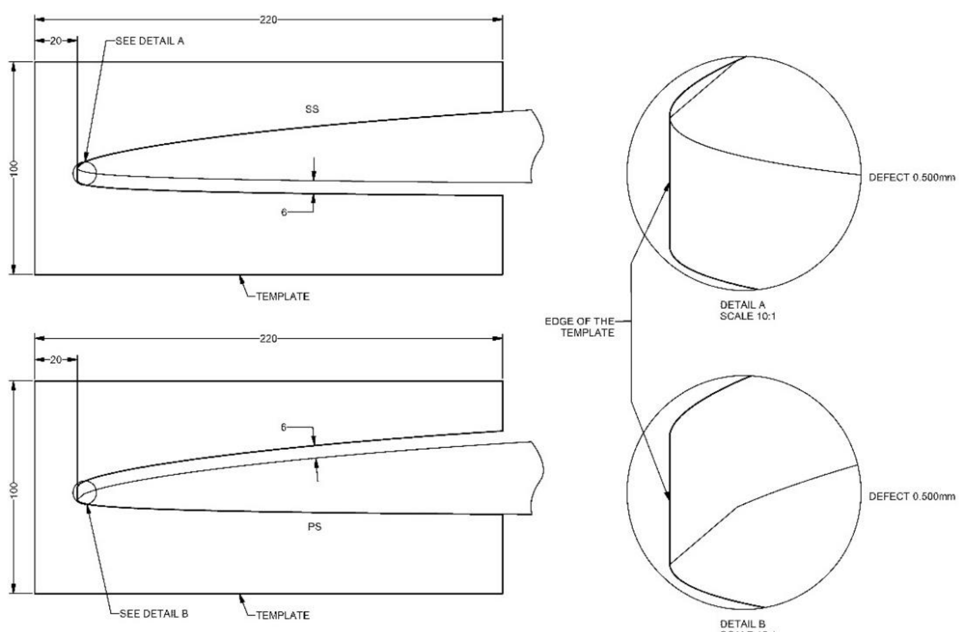


Figure 10: Application of the template to a leading-edge with 0.5 mm defect

The photograph in Figure 11 shows the application of the leading-edge template to a physical model of NACA-66 foil leading-edge with a 0.25 mm defect. This defect is very small and it is visible as a tiny speck of light on the back of the foil, i.e. between the foil and the upper edge of the template. On the rest of the foil back, the contour of the template upper edge fits tightly to the foil without any gaps.

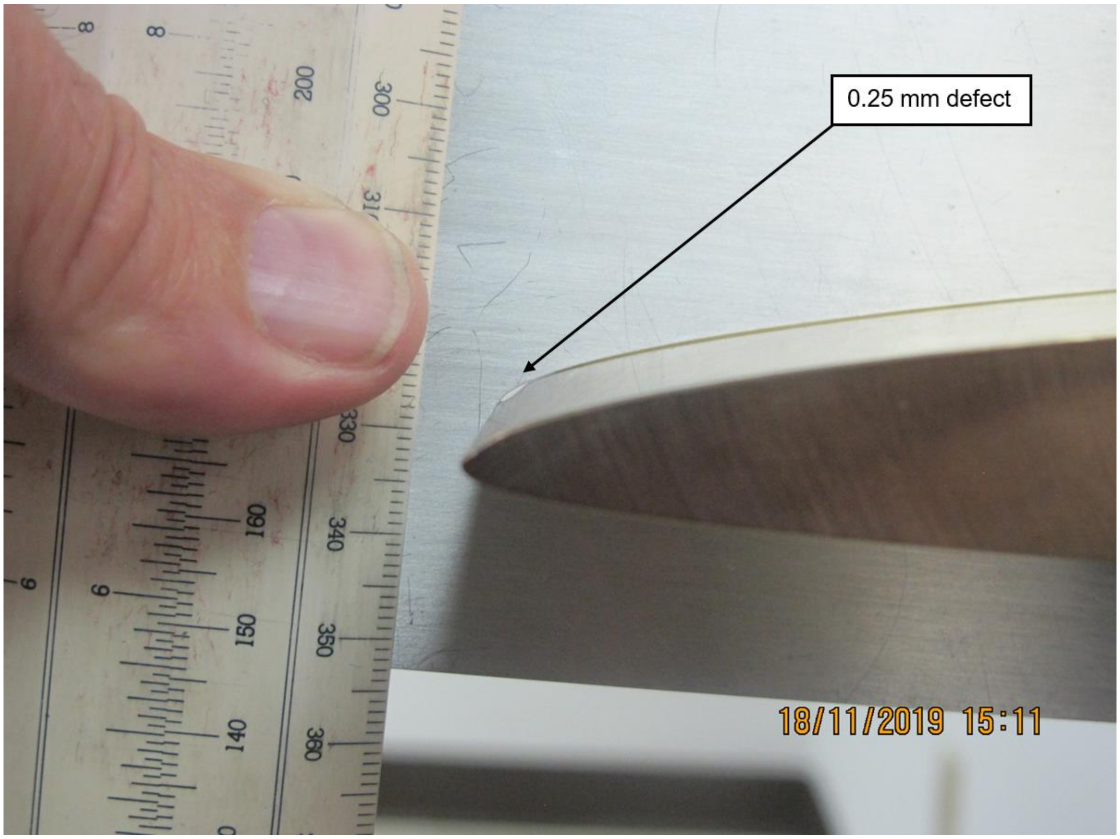


Figure 11: Application of the template to a model leading-edge of NACA-66 foil with a 0.25 mm defect.

Dimensions of the LE defects are given in Table 3 and the geometry of the leading-edge without and with defects is shown in Figures 12, 13, 14 and 15.

| Defect | Point A | | | Point B | | | Length | ΔC |
|---|---|---|---|---|---|---|---|---|
| | X | Y | Angle | X | Y | Angle | | |
| 0.094 | 0.078 | 0.490 | 20.2° | 1.104 | 1.571 | 11.1° | 1.490 | 1.026 |
| 0.250 | 0.078 | 0.489 | 29.8° | 2.796 | 2.531 | 11.5° | 3.390 | 2.718 |
| 0.500 | 0.000 | 0.000 | 57.7° | 3.160 | 2.700 | 16.2° | 4.156 | 3.160 |

Table 3: Dimensions of LE flat defects (units: mm)

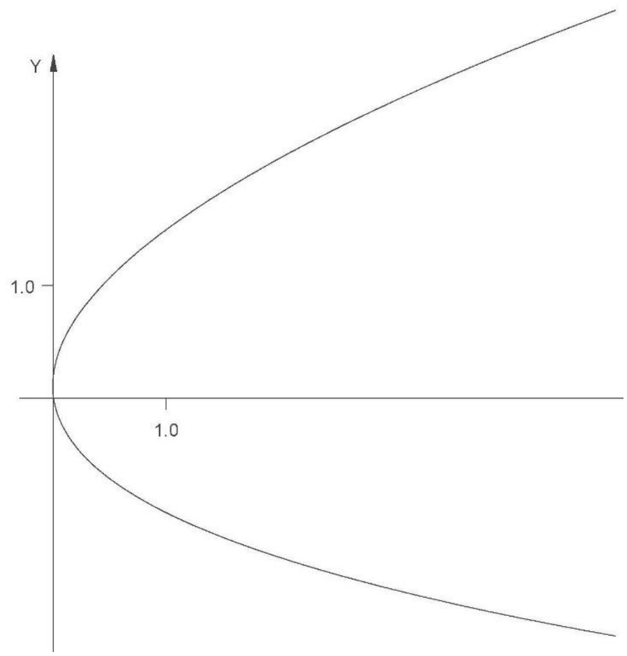


Figure 12: Leading-edge geometry of NACA-66 foil without LE defect

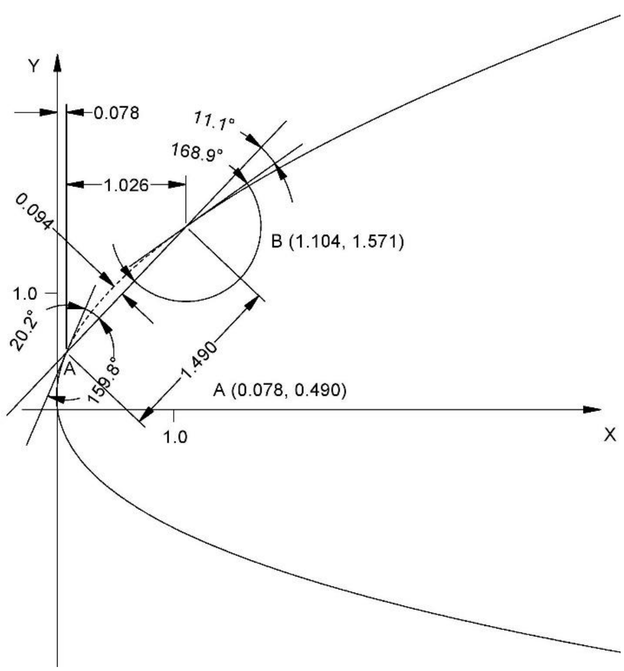


Figure 13: Leading-edge geometry of NACA-66 foil with 0.1 mm defect

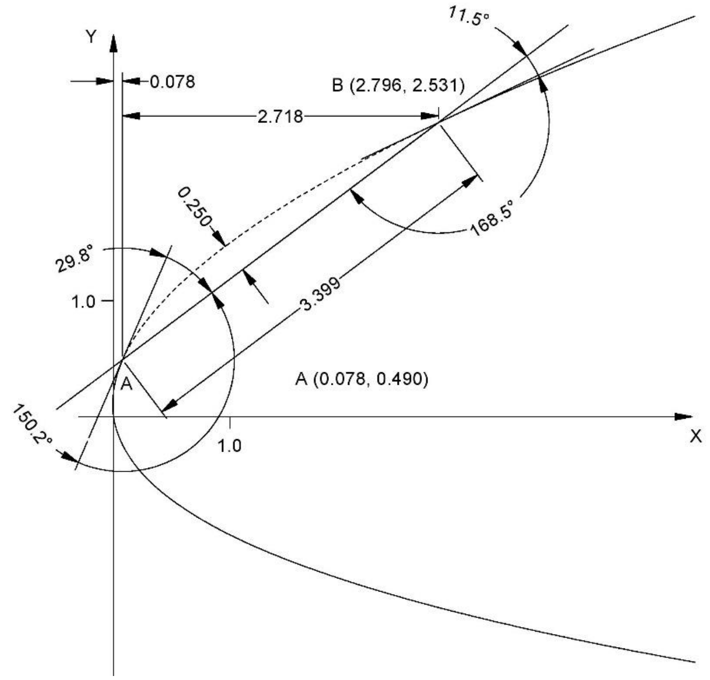


Figure 14: Leading-edge geometry of NACA-66 foil with 0.25 mm defect

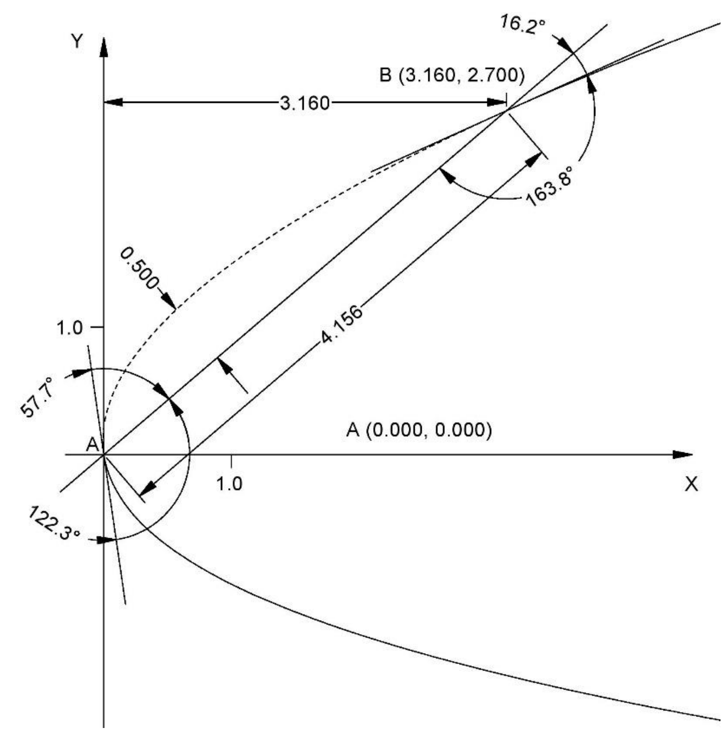


Figure 15: Leading-edge geometry of NACA-66 foil with 0.5 mm defect

### 4.4 Computational domain

The computational domain to be used for CFD simulations had to be sufficiently large to represent an infinite field. The geometry of the computational domain should facilitate the creation of high-quality structured grids. The grids were fully resolved to the foil surface (near wall spacing with $y^+ < 1$) and the cell size was refined near the location of the defects. Since the computational domain is large, to reduce computational requirements, cell size was gradually increased as the boundaries of the domain were approached. Two conflicting requirements had to be satisfied; on one hand, the cells must be as small as possible to resolve the flow with sufficient detail, on the other hand, the total number of cells must also be as small as possible to reduce computational load.

Three types of rectangular domains (H-type, O-type and C-type grid topology) and a circular domain (O-type grid topology) were investigated to compare the grid quality and convergence of the RANS solutions. These investigations showed that the grid quality provided by the circular domain is superior to the quality provided by the rectangular domains. Therefore, the circular domain with the O-type grid topology was chosen for this study [28].

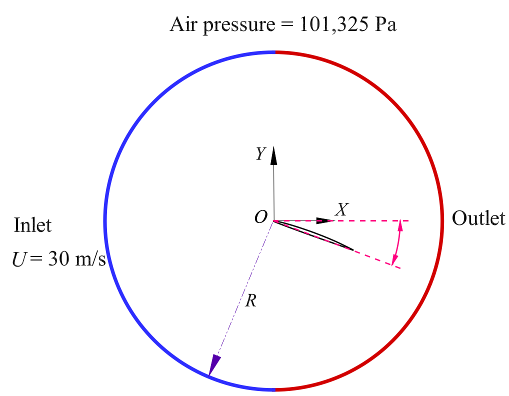


Figure 16: Circular computational domain with boundary conditions

Boundary conditions for the circular computational domain are given in Figure 16. The hydrostatic pressure was not taken into account in the present simulations. The pressure boundary condition with p = 0 was specified on the outlet. A no-slip wall boundary condition was imposed on the surface of the foil section. The Reynolds number for all cases was $Re = 3 \times 10^7$. At the inlet boundary, a uniform velocity of U = 30 m/s was specified.

### 4.5 Grid generation

The generation of structured grids is dependent on three variables: non-dimensional first grid spacing $y^+$, the grid aspect ratio (AR) and the grid stretching ratio (SR). The non-dimensional first grid spacing $y^+$ is estimated by:

$$y^+ = \sqrt{\frac{0.013U^2}{Re^{1/7}}}\frac{\Delta S}{v}$$

where ΔS is the height of the first grid near the wall. It should be noted that, in STAR-CCM+, ΔS is measured from the centre of the grid cell.

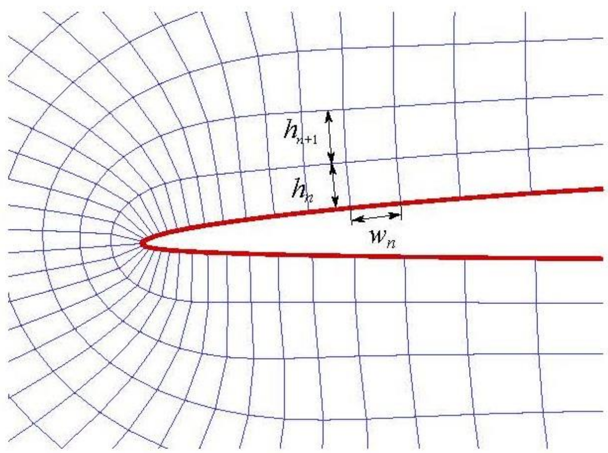


Figure 17: Grid geometry

The cell aspect ratio (AR) is defined as the maximum ratio of cell width to height. As shown in Figure 17, the AR of the n(th) cell is determined as:

$$AR = w_n/h_n$$

where $w_n$ is the grid width and $h_n$ is the grid height.

The grid stretching ratio (SR) is defined as the ratio of the heights of adjacent cells. As shown in Figure 17, the SR of the nth cell is given as

$$SR = h_{n+1}/h_n$$

where $h_n$ and $h_{n+1}$ are the heights of corresponding $n^{th}$ and $(n+1)^{th}$ cells.

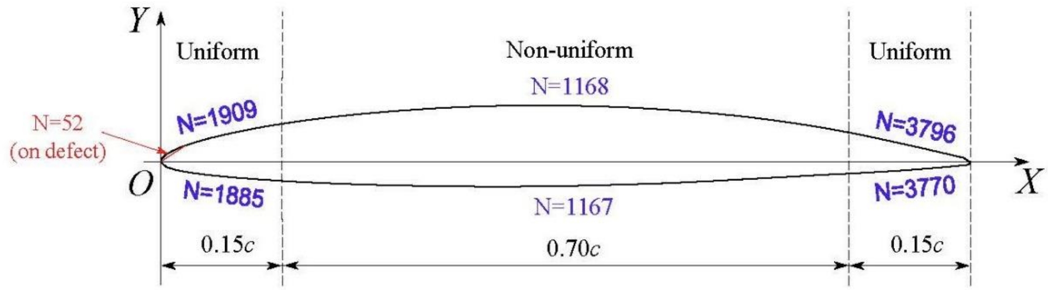


Figure 18: Grid distribution on the foil surface with 0.5 mm LE defect

The cells on the foil surface are generated according to selected first grid spacing $y^+$, aspect ratio AR and grid distribution. As illustrated in Figure 18, the face and the back of the foil were divided into three segments; 0.15c segment for the LE with uniform grids, 0.7c segment for the mid-section with non-uniform grids and 0.15c segment for the TE with uniform grids. In the example illustrated in Figure 18 the total number of nodes on the foil is 13,695, including 1,909/1,885 nodes on the back/face of the leading-edge segment, 1,168/1,167 nodes on the back/face of the middle segment and 3,796/3,770 nodes on the back/face of the trailing-edge segment. In this example, the first grid spacing, $y^+$, is equal to 1.0. The corresponding aspect ratios on the leading-edge, middle and trailing-edge segments are 40, 300 and 20 respectively. The uniform aspect ratio of 20 on the trailing-edge was used to improve the simulation of vortex flow. The number of cells on the defect is 52. Since the linear length of the 0.5 mm defect is 4.156 mm, the length of the cells on the defect is 0.080 mm. See Figures 19 and 20 for grids near the leading-edge and the trailing-edge respectively.

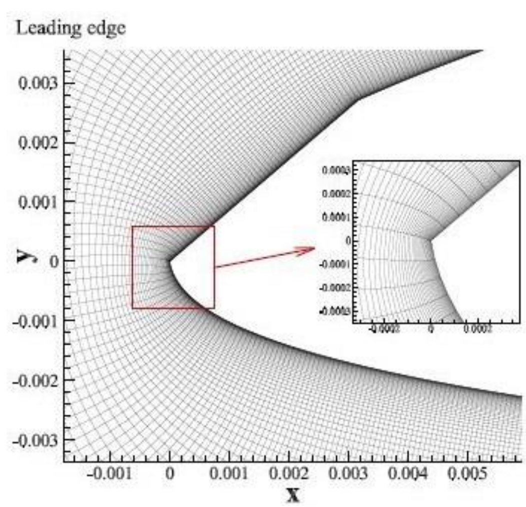


Figure 19: The grid near the leading-edge of the foil

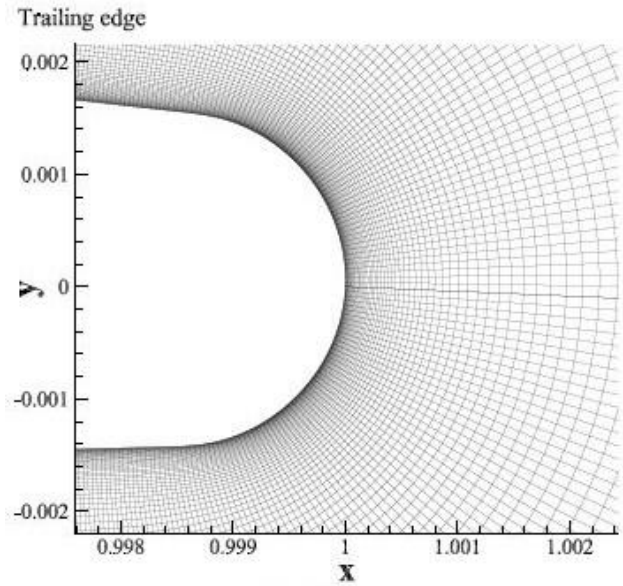


Figure 20: The grid near the trailing-edge of the foil

### 4.6 Convergence criteria

Convergence criteria applied in this study are [28]:

1) Residuals, defined as normalized root-mean-squared values in STAR-CCM+, are used as the first convergence criterion. The acceptable level for convergence is three orders of magnitude reduction in residuals. However, initial values also strongly influence residuals. For example, residuals would not reduce significantly if the initial solution satisfies discretized equations very well. Therefore, it is also necessary to examine the convergence of lift, drag and minimum pressure coefficients.
2) For the convergence of lift, drag and pressure coefficients, the magnitude of change in their values between the current and previous iterations are used as convergence quality indicators after the residual criteria are satisfied. Acceptable magnitudes of change between two iterations are $10^{-6}$ for the lift and drag coefficients and $10^{-5}$ for the minimum pressure coefficient.

The maximum number of iterations for all simulations was set at 40,000. Residuals and changes in lift, drag and pressure coefficients were then checked against the convergence criteria.

Dominis

### 4.7 Simulation parameters and cases

To evaluate the effect different parameters have on the convergence of CFD simulations, over 1,000 CFD simulation cases were run for circular computational domains of several different sizes [28]. Runs also included different combinations of angles of attack, turbulence models, grid stretching ratios, LE and TE grid aspect ratios, and first grid spacing $y^+$. Values of parameters that were kept constant during all these runs are:

| | | | |
|---|---|---|---|
| Air pressure | $p_a$ | = | 101,325 Pa |
| Density of water | $\rho$ | = | 1,000 kg/m$^3$ |
| Kinematic viscosity of water | $\nu$ | = | $1.0 \times 10^{-6}$ m$^2$/s |

In these convergence studies, the number of nodes used was from 791,415 to 2,013,312. The summary of simulation cases and parameters used is presented in Table 4.

| Parameter description | No. of cases | Parameters used in simulations |
|---|---|---|
| Computational domain in terms of radius of domain | 6 | 6 m, 2 m, 8 m<br>24 m, 30 m, 36 m |
| Grid stretching ratio | 2 | 1.1<br>1.2 |
| Grid aspect ratio at LE | 7 | 320.00, 160.00, 113.12<br>80.00, 56.56, 40.00 |
| Grid aspect ratio at TE | 6 | 120.0, 80.0, 60.0<br>40.0, 30.0, 20.0 |
| First grid spacing $y^+$ | 14 | 0.5, 0.707, 1.0, 1.414<br>2.0, 2.828, 4.0, 5.0<br>10.0, 15.0, 30.0, 60.0<br>90.0, 120.0 |
| Turbulence models | 6 | Spalart-Allmaras one-equation model<br>$k$ - $\varepsilon$ two-equation model<br>$k$ - $\omega$ two-equation model<br>SST $k$ - $\omega$ two-equation model<br>elliptic blending model<br>Reynolds stress model |

Table 4: Summary of simulation cases

## 4.8 2D CFD simulations and best practice settings for STAR-CCM+

After extensive convergence studies, the best practice settings for 2D CFD simulations under investigation were determined for steady RANS solver in STAR-CCM+. See Table 5 for the number of grids used for NACA-66 without and with defects. Best practice settings and default parameter settings for STAR-CCM+ are given in Tables 6 and 7 respectively.

| Description | No defect | 0.5 mm defect | 0.25 mm defect | 0.094 mm defect |
|---|---|---|---|---|
| No. of cells over defect | | 52 | 42 | 19 |
| No. of cells on the back | 3,044 | 3,041 | 3,043 | 3,043 |
| No. of cells on the face | 3,014 | 3,014 | 3,014 | 3,014 |
| Total no. of cells on the foil | 6,058 | 6,055 | 6,057 | 6,057 |
| Total no. of cells in the computational domain | 890,526 | 890,085 | 890,379 | 890,379 |

Table 5: No. of cells for the modified NACA-66 (a=0.8, f/c=0.014, t/c=0.0416) without and with LE defects

| Description | Best practice setting |
|---|---|
| Domain type | Circular |
| Domain size | R = 24 m |
| Grid topology | O-type |
| First grid spacing, $y^+$ | 1.0 |
| Grid stretching ratio | 1.1 |
| Grid aspect ratio near LE | 40 |
| Grid aspect ratio near TE | 120 |
| No. of grids over 0.5 mm defect | 52 |
| No. of grids over 0.25 mm defect | 43 |
| No. of grids over 0.0.094 mm defect | 19 |
| Wall treatment | low $y^+$ wall treatment |
| Turbulence model | Standard $k$ - $\omega$ |

Table 6: Best practice settings for STAR-CCM+

| Simulation parameter | Default setting |
|---|---|
| Convection scheme | 2nd order upwind |
| Gradient method | Hybrid Gauss-Least squares method |
| Limiter method | Venkatakrishnan method |
| Custom accuracy level selector | 2nd order |
| Reference pressure | 101,325 Pa |
| Initial turbulence intensity, $I$ | 1% |
| Initial turbulence viscosity ratio, $\mu_t/\mu$ | 10.0 |
| Linear solver | Algebraic multigrid method (AMG) |
| Relaxation scheme | Gauss-Seidel |
| Under-relaxation factor for velocity | 0.4 |
| Under-relaxation factor for pressure | 0.1 |
| Under-relaxation factor for turbulence | 0.8 |
| Convergence tolerance | 0.1 |

Table 7: Default settings used with STAR-CCM+

### 4.9 Cavitation buckets for the modified NACA-66 (a=0.8, f/c=0.02, t/c=0.2)

In his seminal paper from 1966, Terry Brocket [19] used potential-flow theory to compute negative minimum pressure coefficients for modified NACA-66 (a=0.8)

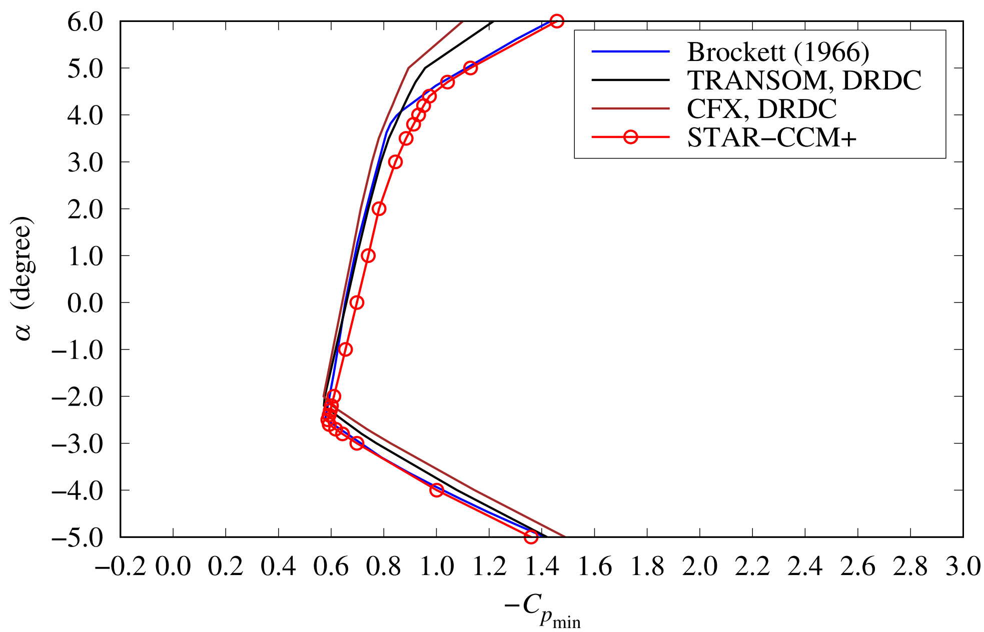


Figure 21: Cavitation buckets for the modified NACA-66 (a=0.8, f/c=0.02, t/c=0.2) foil without LE defects

sections with a wide range of camber and thickness distributions. To verify the numerical results of STAR-CCM+ simulation runs, additional CFD simulations were carried out on the modified NACA-66 (a=0.8, t/c = 0.2, f/c = 0.02) and the results were compared to potential flow solutions by Brocket (1966) and numerical solutions by ANSYS CFX and TRANSOM by DRDC (Hally, 2009) [27]. There is generally a good agreement among the 4 solutions (see Figure 21).

### 4.10 Cavitation buckets for the modified NACA-66 (a=0.8, f/c=0.014, t/c=0.0416) without and with LE defects

Cavitation buckets were computed for NACA-66 (a=0.8, f/c=0.014, t/c=0.0416) without and with three LE defects defined in section 4.2. Table 8 lists all simulation cases. Figure 22 shows the minimum pressure coefficient bucket for the foil without LE defect. Figures 23 through 25 show minimum pressure coefficient buckets for the foils with 0.1 mm, 0.25 mm and 0.5 mm LE defects.

| Description of variable | Variable setting |
|---|---|
| Reynolds number, Re | $3 \times 10^7$ |
| Inflow velocity (m/s) | 30.0 |
| LE defect | no defect<br>0.5 mm defect<br>0.25 mm defect<br>0.094 mm defect |
| Angle of attack, α, (degrees) | 2.75, 3.00, 4.00<br>1.75, 2.00, 2.25, 2.50<br>0.90, 1.00, 1.25, 1.50<br>0.50, 0.60, 0.70, 0.80,<br>0.10, 0.20, 0.30, 0.40<br>0.00<br>-0.10, -0.20, -0.30, -0.40<br>-0.50, -0.60, -0.70, -0.80<br>-0.90, -1.00, -1.25, -1.50<br>-1.75, -2.00, -2.25, -2.50<br>-2.75, -3.00, -4.00 |

Table 8: Simulations for the modified NACA-66 foil (a=0.8, f/c=0.014, t/c=0.0416) without and with LE defects

From Figures 23 through 25 it can be seen that the LE defects have the effect to narrow the cavitation bucket for certain ranges of angles of attack. The following observations can be made: the 0.5 mm defect can narrow the cavitation bucket angles from around -1º to around +2.5º, the 0.25 mm defect can narrow the bucket from 0º to around +2.7º and the 0.1 mm defect can narrow the cavitation bucket for angles great than 0º.

Dashed lines in Figures 23 through 25 show one example in the propeller design range. A narrower cavitation bucket can reduce the cavitation inception speed.

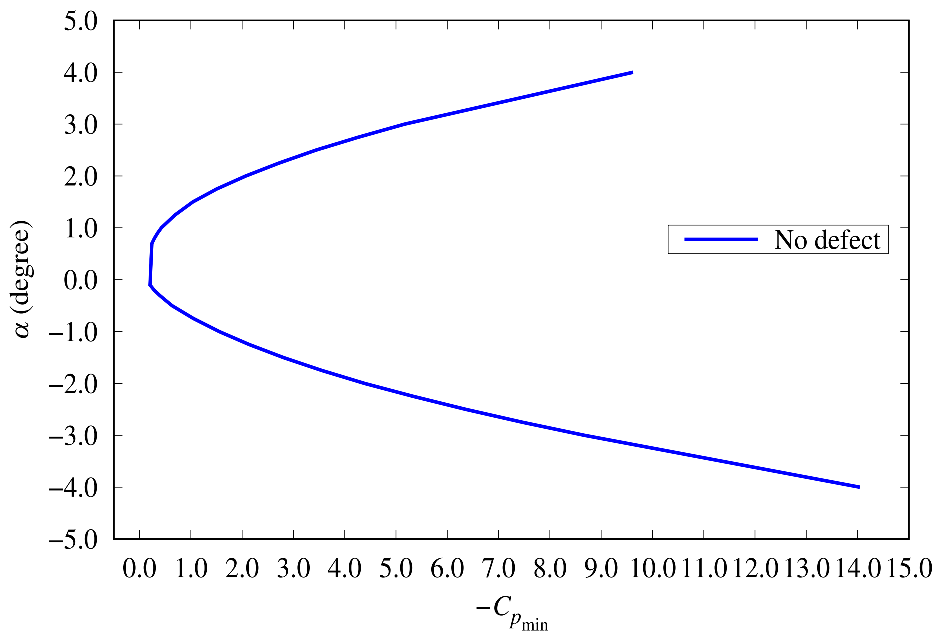


Figure 22: Cavitation bucket, for the modified NACA-66 (a=0.8, f/c=0.014, t/c=0.0416) foil, no LE defect

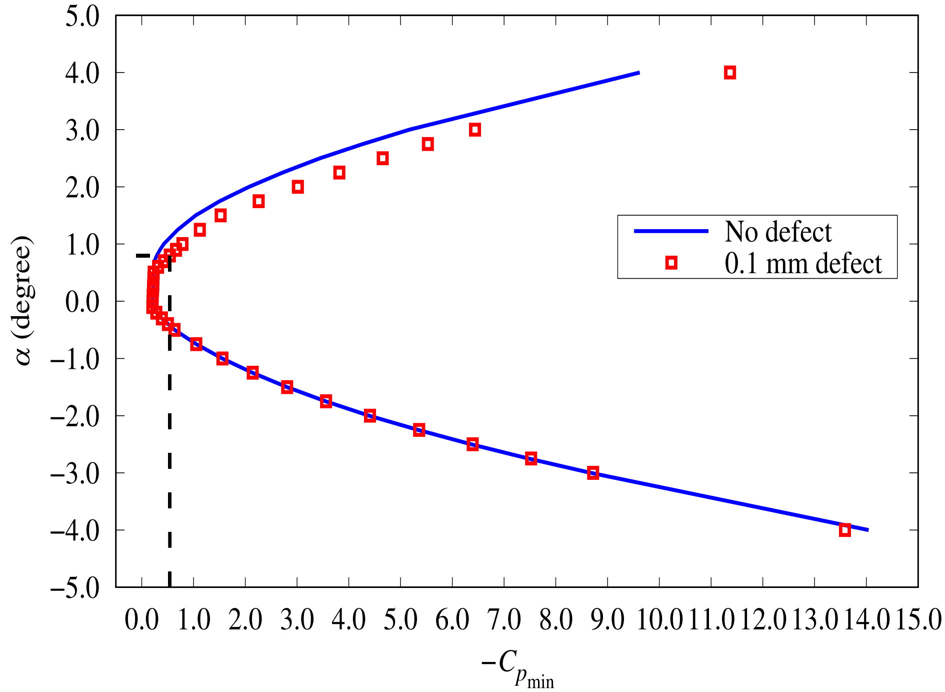


Figure 23: Cavitation bucket, for the modified NACA-66 (a=0.8, f/c=0.014, t/c=0.0416) foil, 0.1 mm LE defect

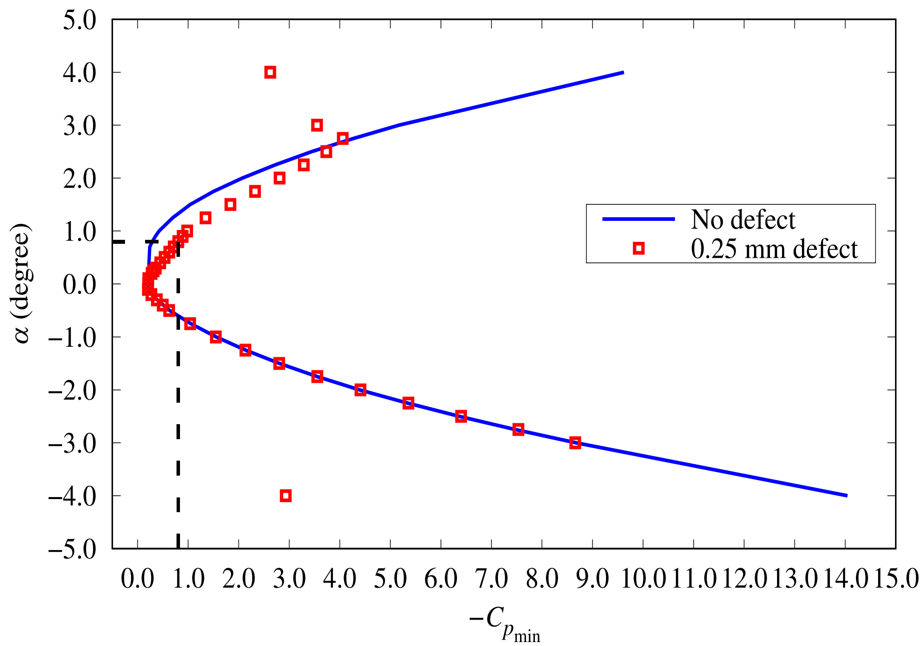


Figure 24: Cavitation bucket, for the NACA-66 (a=0.8, f/c=0.014, t/c=0.0416) foil, 0.25 mm LE defect

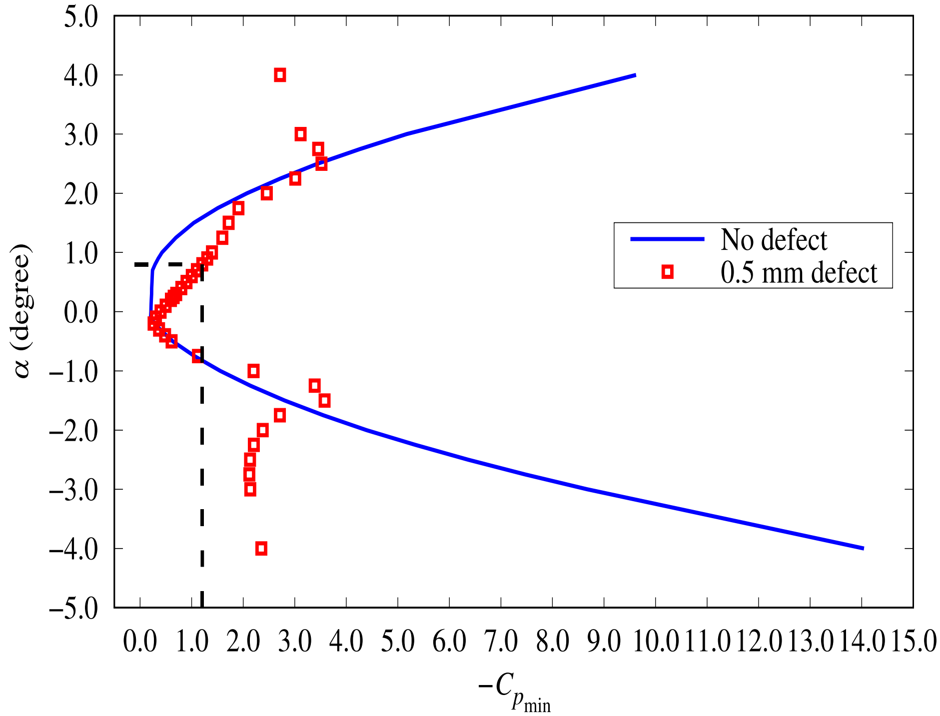


Figure 25: Cavitation bucket, for the modified NACA-66 (a=0.8, f/c=0.014, t/c=0.0416) foil, 0.5 mm LE defect

### 4.11 Effect of LE defects on cavitation inception speed

As an example of the foil performance in the typical propeller design range, Figure 26 presents the contours of pressure coefficient and streamlines near the LE at α = 1.0º for the modified NACA-66 (a=0.8, f/c=0.014, t/c=0.0416) foils without defect and with 0.5 mm, 0.25 mm and 0.1 mm defects. It can be observed that the defect causes lower pressure near the LE. Locations of the minimum pressure depend on the size of the defect and they are located close to the upper end of the defect. For example, the coordinates of the location of the minimum pressure for the foil with 0.5 mm defect is at (0.00324, 0.00266) and the location of the upper end of the defect is at (0.00316, 0.00270). Figure 27 shows pressure distributions on face and back of the modified NACA-66 (a=0.8, f/c=0.014, t/c=0.0416) foil without and with defect at α = 1.0º.

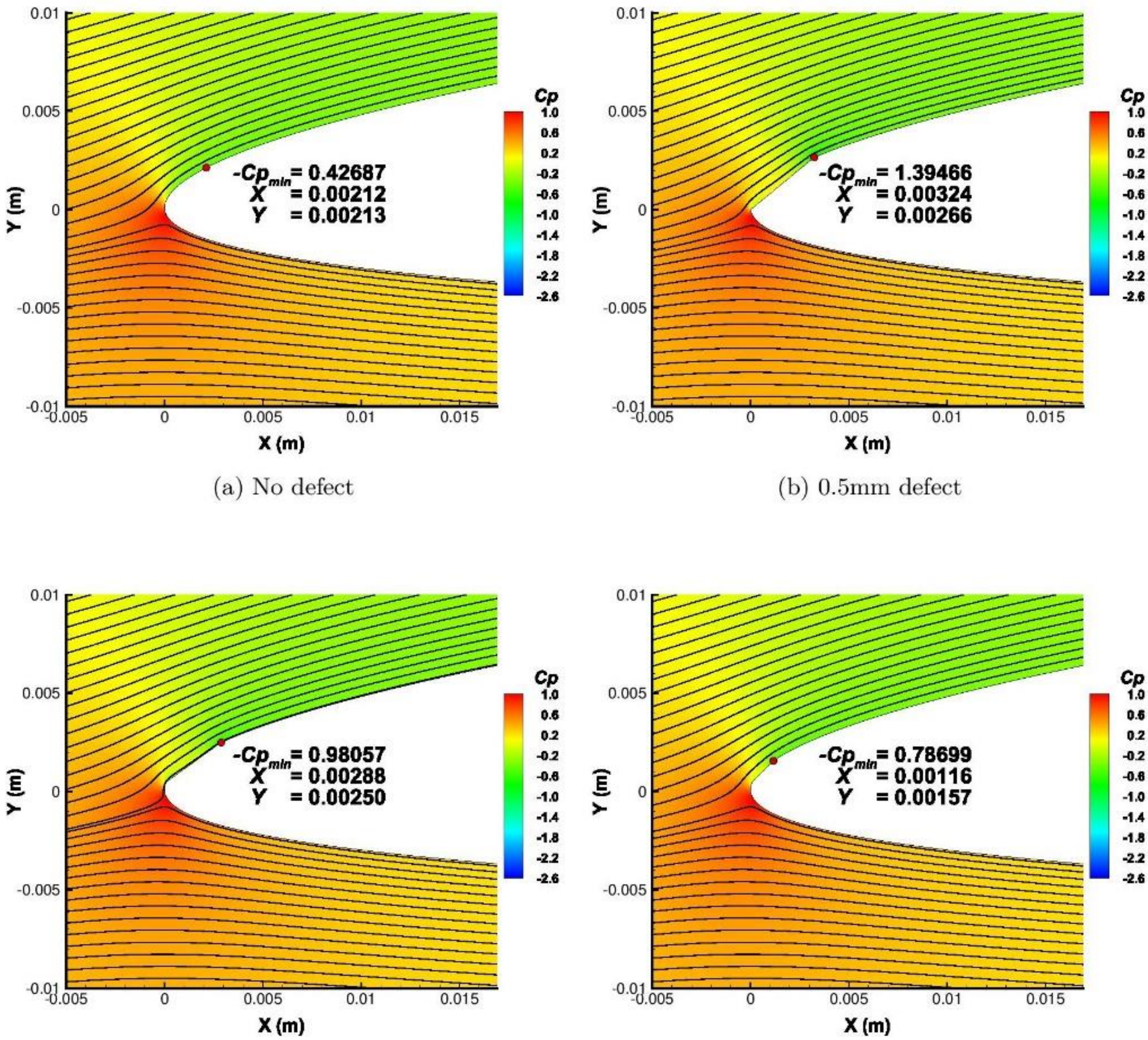


(a) No defect

(b) 0.5mm defect

(c) 0.25mm defect

(d) 0.1mm defect

Figure 26: Pressure coefficient contours and streamlines for the modified NACA-66 (a=0.8, f/c=0.014, t/c=0.0416) foil at α = 1.0º without and with LE defects.

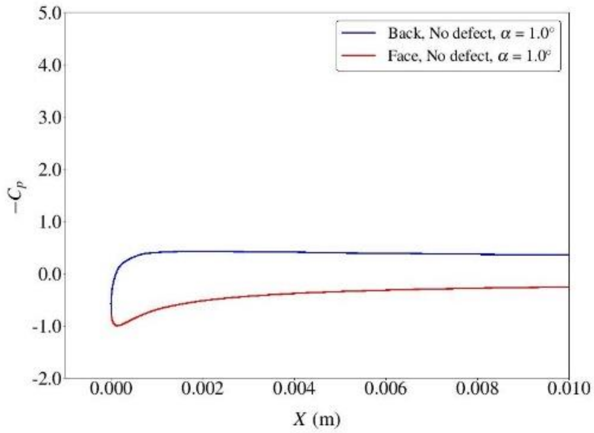


(a) No defect

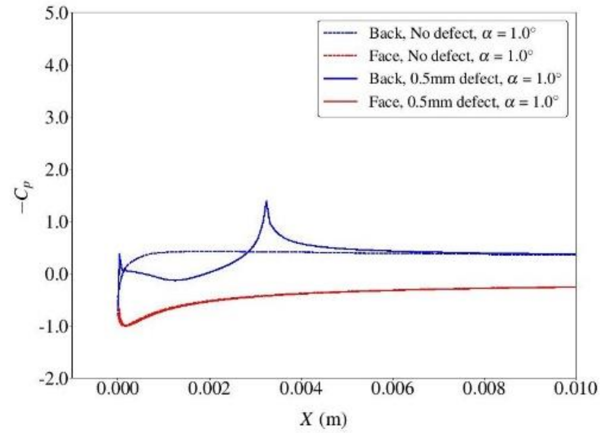


(b) 0.5mm defect

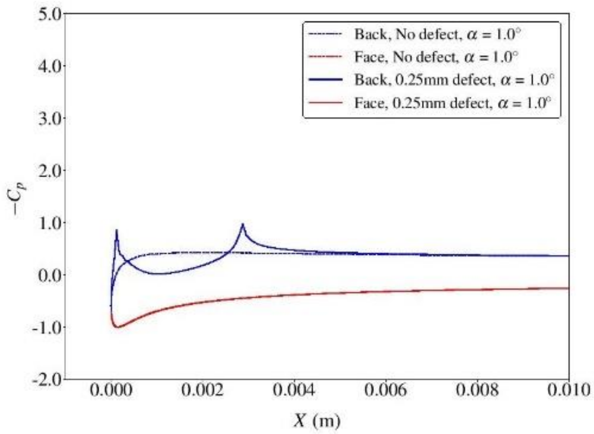


(c) 0.25mm defect

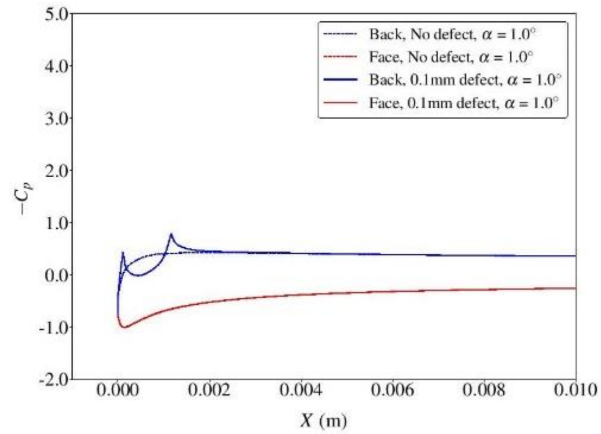


(d) 0.1mm defect

Figure 27: Pressure distributions on face and back for the modified NACA-66 (a=0.8, f/c=0.014, t/c=0.0416) foil at $\alpha = 1.0°$.

Figure 27 shows that the negative pressure peaks for the section are at the ends of the flats and on the side where the defects are located. The flow separates at the furthest forward edge of the defect. When the flow separates the lift of the section decreases and the drag increases. The 0.5 mm defect which started exactly at the leading-edge showed cavitation on both sides of the section.

Minimum pressure coefficients ($-C_{pmin}$) were computed for each CFD simulation. Figure 28 shows differences in computed minimum pressure coefficients for the foil without defects and 3 foils with LE defects. In the range of angles of attack from -2º to +2º which is likely to be of interest to propeller designers who would use this section, the difference in minimum pressure coefficient between the foil without defects and foils with defects is significant.

To quantify the reduction in cavitation inception speed due to LE defects a cavitation Inception Speed Ratio (ISR) can be defined as follows:

$$ISR = \sqrt{\frac{C_{p_{min}}}{C'_{p_{min}}}}$$

where - $C_{p_{min}}$ is the minimum pressure coefficient for the foil without LE defect
- $C'_{p_{min}}$ is the minimum pressure coefficient for the foil with LE defect

Table 9 shows minimum pressure coefficients, cavitation inception speed ratios and percentage inception speed reduction for the modified NACA-66 foils for an angle of attack of 1.0º.

| Defect size | $-C_{pmin}$ | Location of $-C_{pmin}$ (X,Y) (m) | | Cavitation inception speed ratio | Percentage inception speed reduction |
|---|---|---|---|---|---|
| No defect | 0.427 | 0.00212 | 0.00213 | 1 | |
| 0.5 mm | 1.395 | 0.00324 | 0.00266 | 0.553 | 44.7 % |
| 0.25 mm | 0.981 | 0.00288 | 0.00250 | 0.660 | 34.0 % |
| 0.094 mm | 0.787 | 0.00116 | 0.00157 | 0.737 | 26.3 % |

Table 9: Cavitation inception speed reduction for the modified NACA-66 (a=0.8, f/c=0.014, t/c=0.0416) foils without and with 0.5 mm, 0.25 mm and 0.1 mm LE defects at α = 1.0º

Figure 28 shows $C_{pmin}$ distributions for the modified NACA-66 (a=0.8, f/c=0.014, t/c=0.0416) foils without and with LE defects. Figure 29 shows percentage reduction in cavitation inception speed for the modified NACA-66 foils with 0.5 mm, 0.25 mm and 0.1 mm LE defects

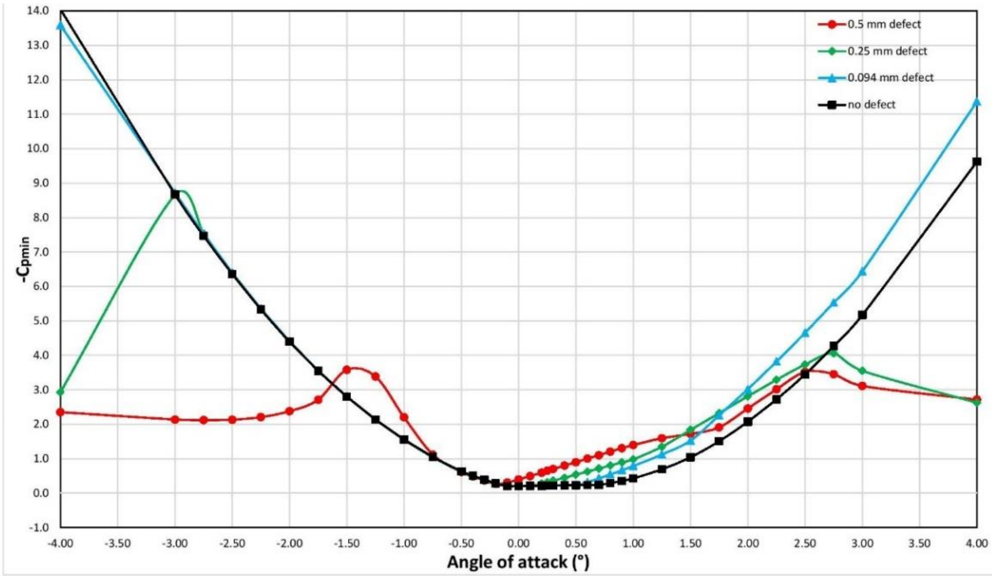


Figure 28: $C_{pmin}$ distributions for the modified NACA-66 (=0.8, f/c=0.014, t/c=0.0416) foils without and with 0.5 mm, 0.25 mm and 0.1 mm LE defects

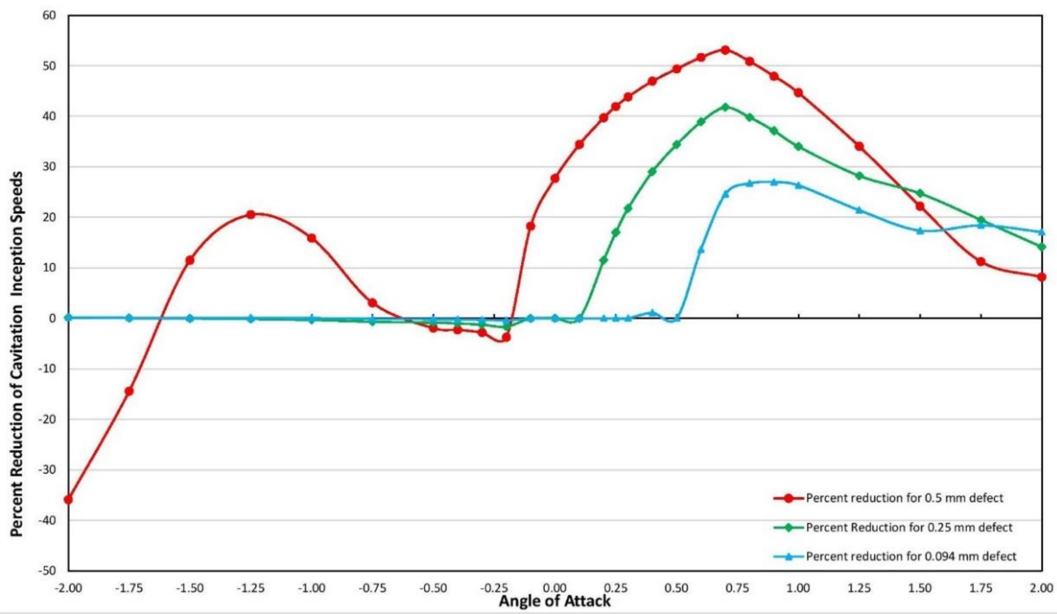


Figure 29: Percentage reduction in cavitation inception speed for the modified NACA-66 (a=0.8, f/c=0.014, t/c=0.0416) foils with 0.5 mm, 0.25 mm and 0.1 mm LE defects

Dominis

### 4.12 Effect of LE defects on efficiency

The ratio of lift coefficient to drag coefficient of a 2D propeller section provides a suitable indicator of the efficiency of the propeller which incorporates the 2D section. The effect LE defects have on the ratio $C_l/C_d$ is shown in Figure 30. In the normal operating range of angles of attack for a moderately loaded propeller, LE defects have little effect on the efficiency. However, at larger angles of attack or for a more heavily loaded propeller or a propeller operating in a highly uneven wakefield, LE defects would reduce the efficiency more significantly.

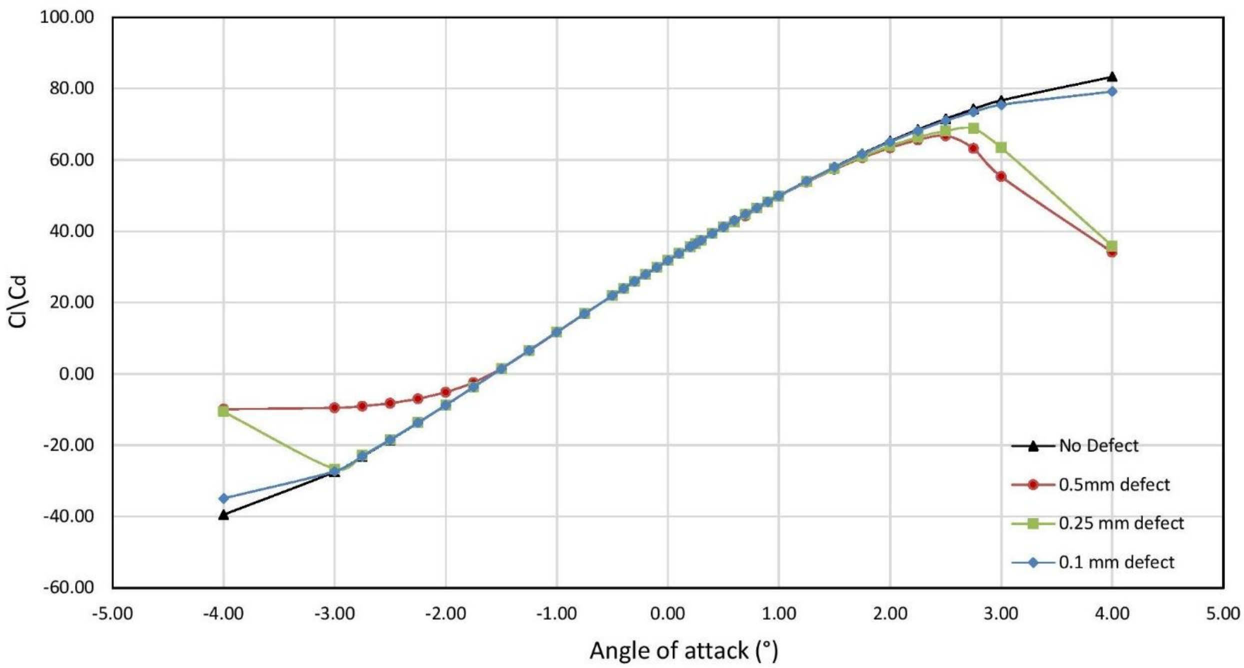


Figure 30: Ratio of lift coefficient to drag coefficient vs. angle of attack

## 5.0 2D FOIL MODEL TESTS IN THE CAVITATION TUNNEL

Physical models of the 2D foils used in the CFD investigations were used in cavitation tunnel experiments. All foil models were manufactured with a chord length of 1 m. The large scale of the model ensures that the Reynolds Number is close to that of a full-scale propeller. Matching the Reynolds Numbers ensures that the viscous and inviscid hydrodynamic forces are in the correct ratio. The large size of the test model also permits the accurate manufacture of relatively small leading-edge defects at full scale.

Dominis

## 5.1 Cavitation tunnel at Brodarski Institut

The large cavitation tunnel at the Brodarski Institut in Zagreb, Croatia was selected as a venue for 2D foil model tests. The working section of the cavitation tunnel is 3.5 m long with a cross-section of 1 m by 1 m. The maximum water velocity and range of pressures that can be achieved in the tunnel are 8.6 m/s and 0.1 to 2 bar respectively. The minimum Cavitation Number which can be achieved in the tunnel is between 0.32 and 0.35. Cavitation Number σ is defined as follows:

$$\sigma = \frac{P_{\infty} - P_{v}}{\frac{1}{2}\rho U^{2}}$$

Dimensions of the measurement section of the cavitation tunnel and the location of the 2D foil model inside the measurement section are shown in Figure 31.

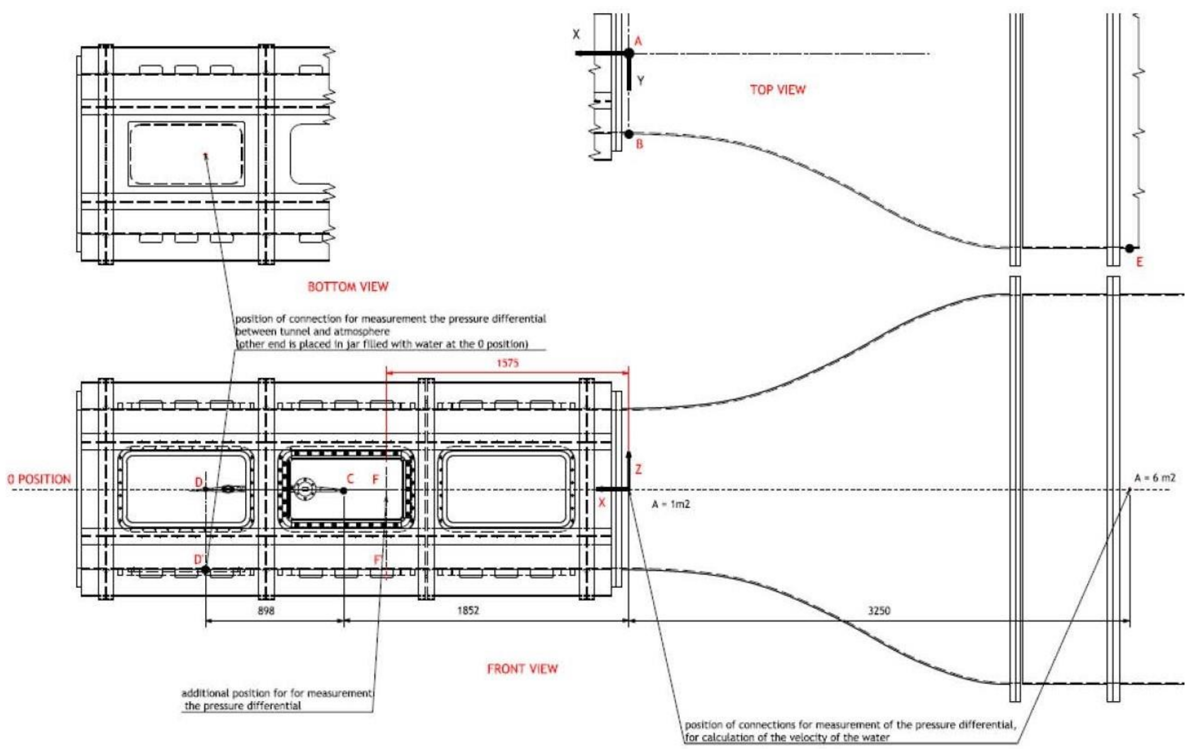


Figure 31: Measurement section of the cavitation tunnel at Brodarski Institut in Zagreb, Croatia

The velocity of the water flow is computed from the measured pressure differential between points E and B. Pressure in the tunnel is measured at points D’ and F’. Pressures at points D and F are computed by subtracting from these two measurements the pressure difference between the bottom and the middle of the tunnel.

### 5.2 2D foil model fabrication

The 2D foil models for cavitation tunnel testing were manufactured in Aluminum 6061-T651. To increase the visibility of the foil inside the tunnel and to protect the model foils from corrosion, the models were anodized. The final size of the model was 1 m chord by 0.525 m span. Originally, it was planned to have the 2D foil models with a span of 1 m so that the models could span from one end to the other end of the tunnel. Unfortunately, the span of the 2D foil models had to be reduced to 525 mm to limit forces acting on the foil flanges and their support bearing and seals mounted in the windows of the tunnel.

This change in the model geometry, from a full wall-to-wall 2D foil to a low-span “wing” model makes a significant difference in the hydrodynamics. Large end-plates were incorporated in the model to produce some semblance of two-dimensional flow over the wing. CFD analysis of the model indicated that the flow was uniform over almost all of the wing and cavitation inception could be expected to be the same at almost all span-wise locations. The calculated inception speed ratios for the “wing” model in the tunnel and the 2D sections are compared in Figure 32. The magnitude and shape of the curves are similar but the “corresponding” angles of attack for the wing are greater than the 2D section’s as they depart further from the section’s zero-lift angle (-1.56°), as might be expected.

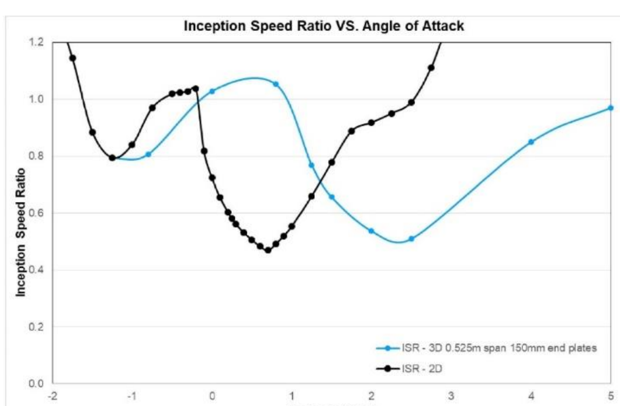


Figure 32: ISR, CFD prediction for 2D and 0.525 m foil model

The 2D foil models were CNC milled from solid blocks of Aluminum. Through holes to reduce the weight of the foil and seats for foil flanges were pre-machined in the foil blank before milling of foil surfaces. Hydrodynamic surfaces were milled using the Dominis process for CNC milling to *“final form and finish”* [29, 30, 31] without hand grinding. Leading-edges and foil surfaces were CNC milled chord-wise. Surface roughness ($R_a$) achieved by the Dominis process was 0.6 µm (24 µinch). Residual scallops with a theoretical height of 0.002 mm are visible on the finished surface after milling. These visual artifacts were removed by gentle manual application of 240 grit sandpaper. Finished foil models were laser scanned and found to be globally accurate within +/- 0.100 mm (+/- 0.004 inch). Figures 33 and 34 show photographs of the 2D foil model after CNC milling to *“final form and finish”* and a close-up of the leading-edge of the defective section of the model respectively. A total of five models were manufactured but only one model was tested in the tunnel.

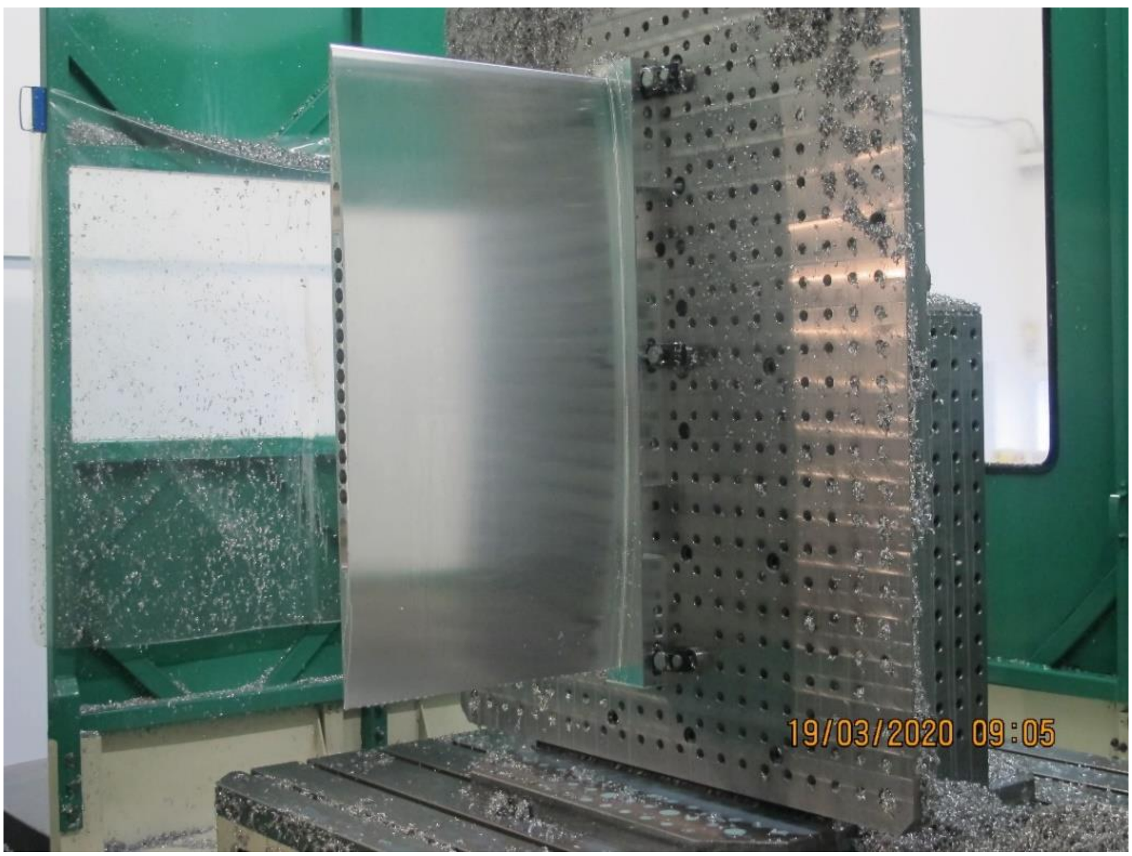


Figure 33: 2D foil model after CNC milling to *“final form and finish”*

To ensure that both the “as-designed” and “as-built” foil containing a LE defect are tested under identical tunnel conditions, it was decided that the foil to be tested in the cavitation tunnel should contain both the “as-designed” and “as-built” sections. Therefore, the foil used for testing consisted of three sections: the “as-designed” section of 250 mm span at one end, the “as-built” section of 250 mm span at the opposite end and a transition section from “as-built” to “as-designed” foil of 25 mm span in the middle. The table with coordinates of the NACA-66 section as modified by Terry Brockett is given in Appendix B. This table contains the coordinates for both the “as-designed” and “as-built” versions of the foil section.

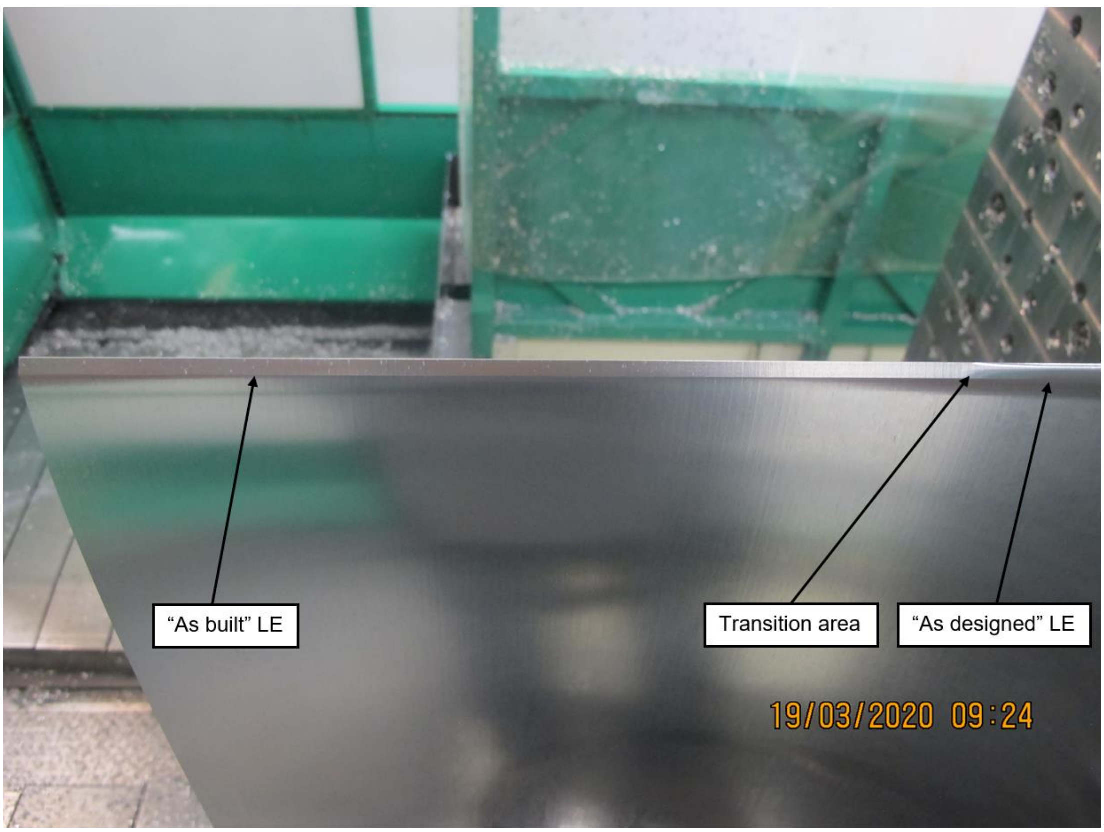


Figure 34: 2D foil model; the leading-edge of the “as-built” section of the foil model containing a 0.5 mm defect

Figure 34A contains a photograph of the complete leading-edge of the anodized experimental foil model. Figures 34B, 34C and 34D contain close-up photographs of “as designed”, “as-built” and transition area of the leading-edge of the experimental foil model.


Figure 34A: View of the leading-edge of the anodized experimental foil model

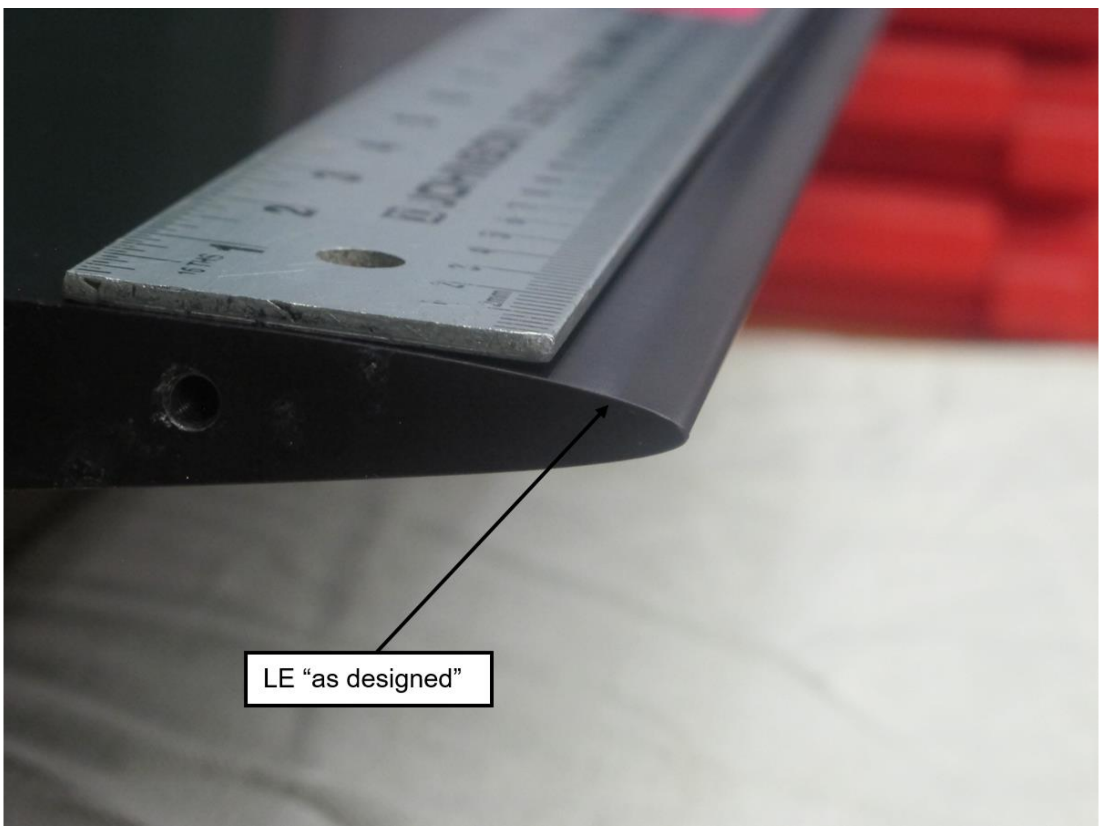


Figure 34B: View of the “as-designed” end of the experimental foil model leading-edge

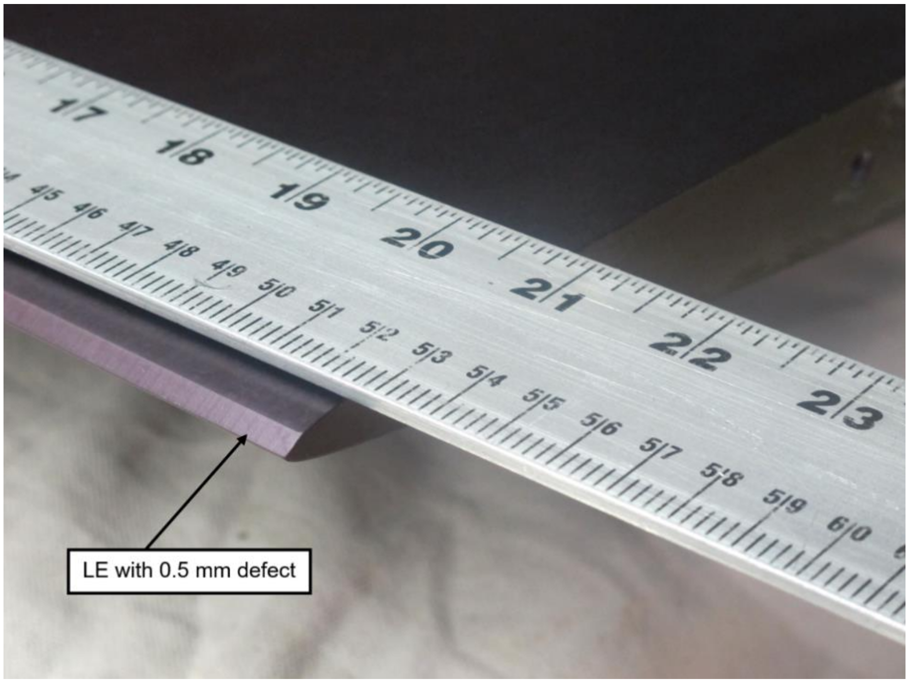


Figure 34C: View of the “as-built” end of the experimental foil model leading-edge with 0.5 mm defect

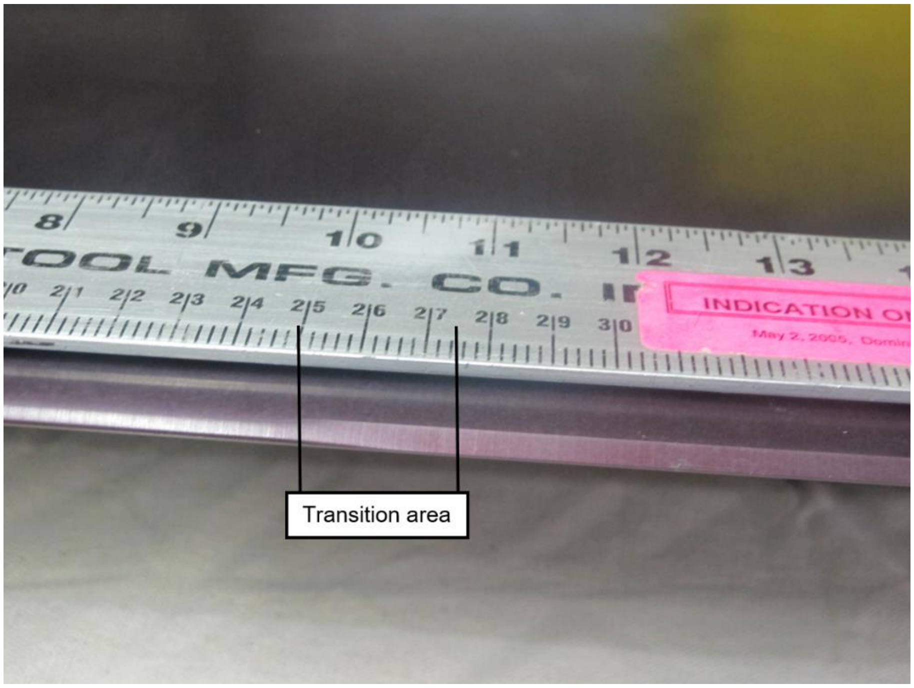


Figure 34D: View of the 25 mm long transition area of the experimental foil model leading-edge.

### 5.3 Experimental set-up in the cavitation tunnel

Four foil flanges are used to mount and secure the 2D foil model in the cavitation tunnel. Flanges are bolted into recessed slots on the sides of the foil. Locations of flanges are at the foil model pivot points located at 25% of the foil chord and at the foil model support points located at 75% of the chord length from the leading-edge. End plates, fabricated in 10 mm thick Lexan, were bolted on each side of the 2D foil model.

The foil model to be tested was positioned in the middle of the measurement section of the cavitation tunnel. Drawings of the foil model with “as-designed” NACA-66 section and with “as-built” (defective) LE section are shown in Appendix C. Drawings of all components of the foil model test assembly in the cavitation tunnel are in Appendix D. See Figure 35 for graphic representation of the test assembly inside the tunnel. Figures 36 through Figure 39 contain photographs of the experimental set-up in the cavitation tunnel. Based on the conclusions from the results of 2D CFD simulations, the experimental set-up in the tunnel was designed to accommodate the range of angles of attack from -2° to +2°.

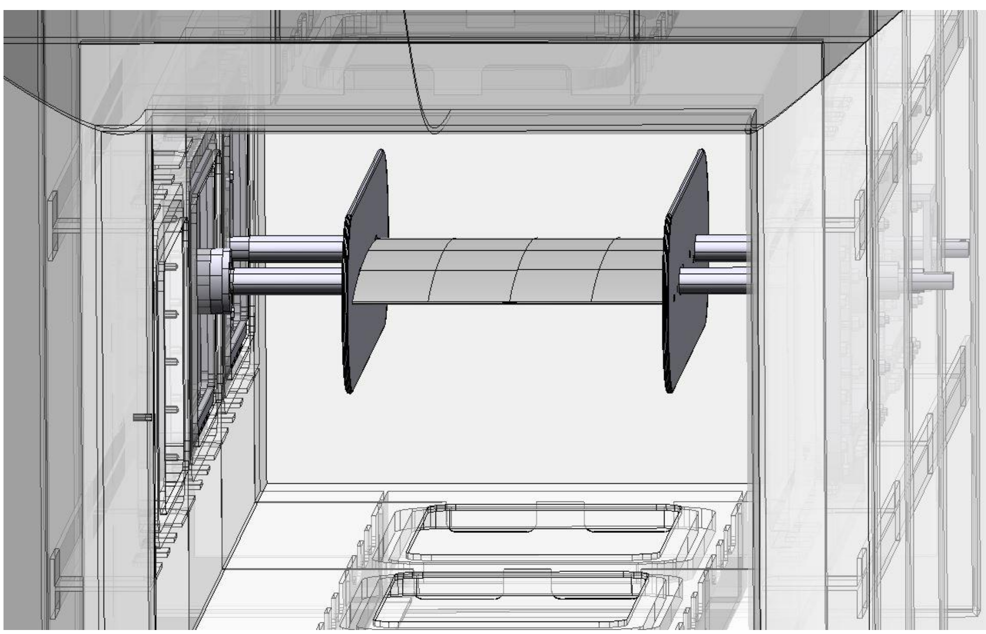

Figure 35: 2D foil with end plates, flanges and sleeves in position inside the cavitation tunnel

Dominis

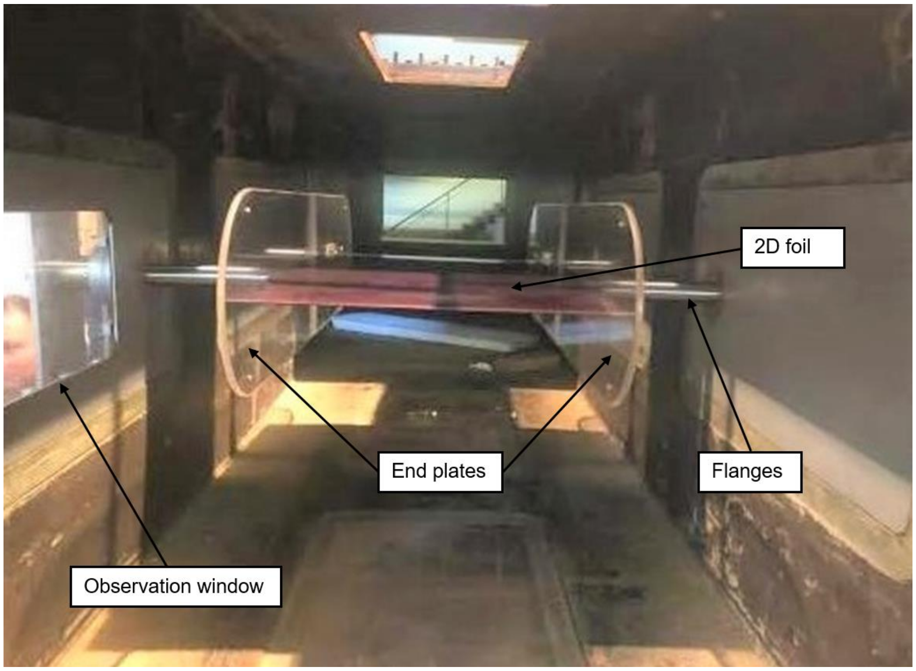


Figure 36: 2D foil test assembly inside the tunnel; looking at the LE


Figure 37: 2D foil in the tunnel; looking through the window in the tunnel ceiling


Figure 38: Measurement section of the cavitation tunnel

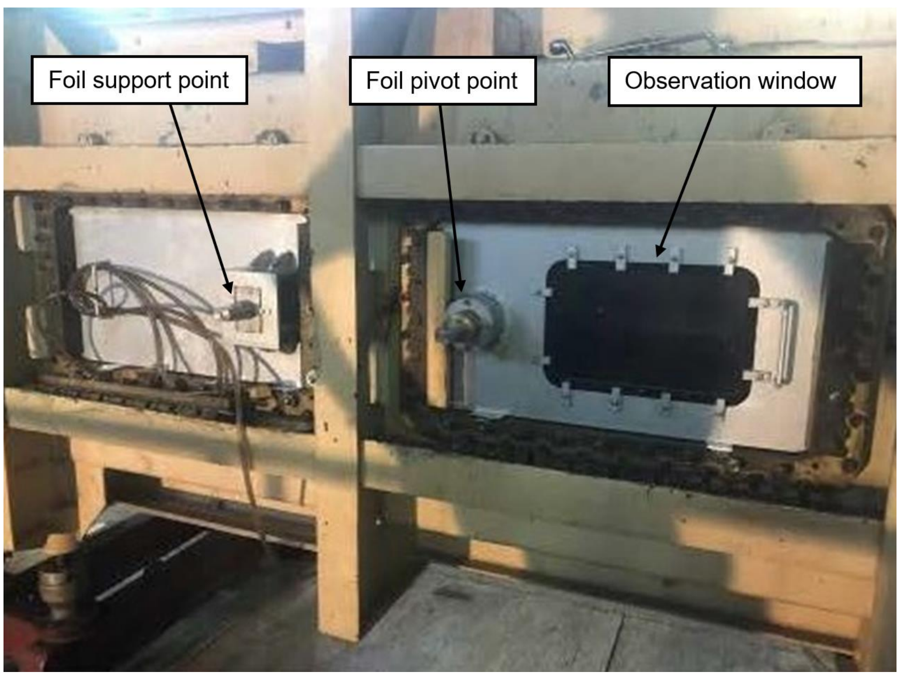


Figure 39: Experiment set-up; observation window, view of the support bearings and seals in the tunnel windows

### 5.4 Description of experiments and tests conducted in the cavitation tunnel

The objective of the experiment was to quantify the cavitation degradation due to defects and to compare these results with those predicted by CFD.

The technique used in the experiments in the cavitation tunnel was to visually observe and record the inception and desinence of cavitation on the LE of the "as-designed" and "as-built" (defective) NACA-66 2D foil models, while the conditions in the tunnel were slowly changing.

All tests in the cavitation tunnel were conducted in the following manner:

- The NACA-66 foil model was rotated to a pre-selected angle of attack and pinned in place at the foil pivot point located at 25% of the chord. After the foil model had assumed its normal position for the current angle of attack, the foil model support point located at 75% of the chord was secured and locked in place.
- The velocity of water in the tunnel was gradually increased up to the maximum of 8.5 m/s, or until the cavitation could be observed on the foil.
- Pressure in the tunnel was also reduced to facilitate the cavitation at the lowest possible cavitation number. Care had to be taken to maintain good visibility for observation in the tunnel.
- The velocity of water was increased and pressure in the tunnel was reduced until cavitation could be observed on both the "as-designed" and defective portions of the foil model. Once this condition was achieved, the velocity of water was alternately decreased and increased until the threshold for inception and desinence of cavitation can be established. Search for this threshold was repeated several times until the confidence in the repeatability of visual observation could be established.
- Readings for the velocity of water, cavitation number and pressure were recorded for each occurrence of cavitation inception and cavitation desinence.

Five experiments and a total of 12 tests were conducted in the cavitation tunnel over the period of five months. A list of experiments and a summary of all tests completed is given in Table 10. Each experiment investigated the performance of the foil for a different range of angles of attack.

All the hardware for rotation of the 2D foil model around the pivot points and for securing the foil model position at the foil support points were designed for testing a 1 m-span test specimen which was originally envisaged. This hardware had a limited angular operating range and had to be refitted in the tunnel for each of the four set-ups to cover different ranges of angles of attack.

| Experiment no. | Set-up | Test no. | Date | Angles of attack (°) | Minimum cav. no. tested |
|---|---|---|---|---|---|
| 1 | 1 | 1 | 4 Sept. 2020 | 0.0 | 0.33 |
| 1 | 1 | 2 | 8 Sept. 2020 | +1.0, -1.0, -2.0 | 0.35 |
| 1 | 1 | 3 | 9 Sept. 2020 | +2.0, +1.0, 0.0 -1.0, -1.5, -2.0 | 0.35 |
| 1 | 1 | 4 | 11 Sept. 2020 | +2.34, -2.34 | 0.30 |
| 1 | 1 | 5 | 17 Sept. 2020 | -0.75 | 0.36 |
| 2 | 2 | 6 | 13 Oct. 2020 | -4.0, -3.5, -3.0 -2.0 | 1.16 |
| 2 | 2 | 7 | 16 Oct. 2020 | -4.0, -3.5, -3.0 -2.5 | 1.39 |
| 3 | 3 | 8 | 23 Oct. 2020 | +3.0, +3.5, +4.0 | 0.22 |
| 3 | 3 | 9 | 5 Nov. 2020 | +3.75, +4.25 +4.50, +4.75 | 0.31 |
| 3 | 3 | 10 | 6 Nov. 2020 | +3.75, +4.0 | 0.29 |
| 4 | 4 | 11 | 18 Dec. 2020 | +5.0, +6.0 +7.0 +7.5,+8.0 | 0.60 |
| 5 | 4 | 12 | 10 Jan. 2021 | +6.0, +8.0 | 1.14 |

Table 10: Summary of experiments and tests conducted in the cavitation tunnel

## 5.5 CFD results for the test set-up

In anticipation of the experimental tests, CFD calculations were made with the test set-up. These indicated that the pressure distributions for span-wise pressures were uniform over ± 40% of the span around the mid-span. Cavitation buckets were developed for the mid-span section for both the “as-designed” (0.0 mm defect) and "as-built" (0.5 mm defect) foil models at an anticipated Reynolds Number of $8*10^6$.

After the experiments were completed mid-span cavitation buckets for the test set-up were developed at the experimental Reynolds Numbers, which ranged from about $2*10^6$ to about $5*10^6$. The cavitation buckets for these cases are given in Figure 40.

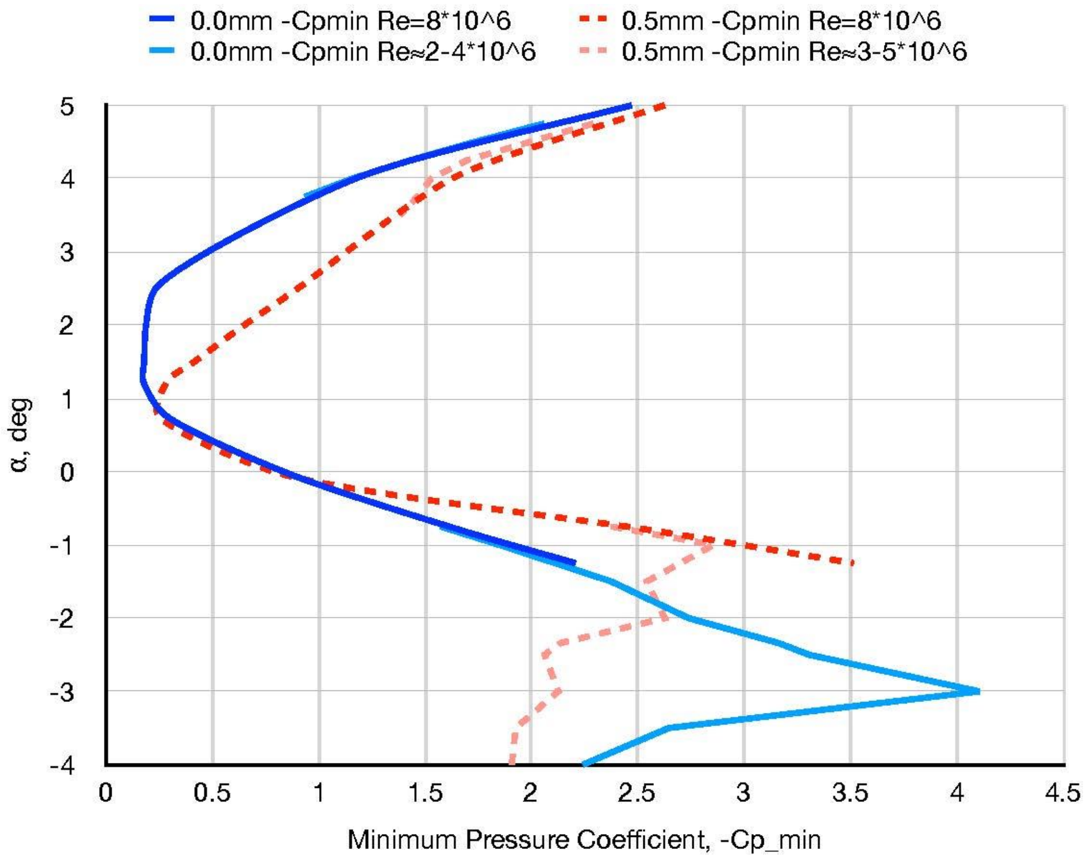


Figure 40: Cavitation buckets for mid-span of test setup foils at Re = $8*10^6$ and at Re used in the experimental tests

Where they overlap, the minimum pressure coefficients for the two different Reynolds Numbers are not significantly different. They would amount to a difference in inception speed of less than 3%. For comparison of CFD and experimental results the results from the experimental Reynolds Numbers will be used where possible and the results at $8*10^6$ only where necessary.

Figure 40 can be compared with Figure 25. The trends are the same. The defect produces a significantly narrower cavitation bucket up to the point where flow separation effects dominate. There is a clear difference in the onset of flow separation effects on the lower surface for the “as-designed” foil at Re ≈ $3*10^6$ and the 2D results at Re ≈ $3*10^7$. The difference for the “as-built” foil is noticeable but less dramatic.

The differences in angles of attack for “equivalent” locations on the bucket arise because the test set-up is a finite wing. Rudimentary finite wing theory predicts that the difference in $Cp_{min}$ should be zero at the zero-lift angle, and that is roughly the case for the “as-designed” foil. To produce the same $Cp_{min}$ at other angles of attack the magnitude of the absolute test set-up angle of attack would be greater than the 2D absolute angle of attack. (The absolute angle is defined here as the difference between the geometric angle of attack and the zero-lift angle of attack.) That absolute angle increase for the same $Cp_{min}$ is clearly seen by comparing Figure 40 and Figure 25.

### 5.6 Experimental results and comparison with CFD

Appendix E contains the record of all observations and measurements taken in the cavitation tunnel. The most relevant measurements for this study are cavitation numbers σ at cavitation inception and desinence for “as-designed” (0.0 mm defect) and “as-built” (0.5 mm defect) foil models.

Cavitation on both portions of the 2D foil model started with streak cavitation at isolated locations. In both cases, the individual cavitation streaks coalesced into sheet cavitation along most of the portion’s span with a very small increase in speed. The cavitation inception condition (speed and pressure) was recorded consistently as being when the individual streaks coalesced into sheet cavitation. The cavitation desinence condition was recorded consistently as being when the sheet cavitation divided into individual streaks. The uniform change from streak to sheet cavitation along most of the span of each portion of the foil suggests that the flow over each portion of the foil was fairly uniform, as the CFD had predicted.

The following observations were made during cavitation tunnel experiments:

1) For all negative angles, cavitation was observed on the face of the 2D foil model. The locations of the onset of cavitation were predicted by the 2D CFD.
2) For all positive angles, cavitation was observed on the back of the 2D foil model. The locations of the onset of cavitation were predicted by the 2D

CFD.

3) The cavitation tunnel cannot produce Cavitation Numbers below about 0.32. For that reason, it was not possible to show cavitation on either the ”as-designed” or the “as-built” portions of the 2D foil model between 0° and 3°, and at 3.5° it could only produce cavitation on the back of the defective portion of the 2D foil model.

Cavitation numbers were recorded for conditions of interest and in this report $\sigma_i$ designates the cavitation number at cavitation inception; $\sigma_d$ designates the cavitation number at cavitation desinence; and $\sigma_m$ designates the mean cavitation number, the mean of all inception and desinence cavitation numbers at a particular angle of attack.

Figure 41 contains the plots of the mean cavitation numbers $\sigma_m$ recorded during the cavitation experiments and CFD predictions of $Cp_{min}$ for the experimental setup.

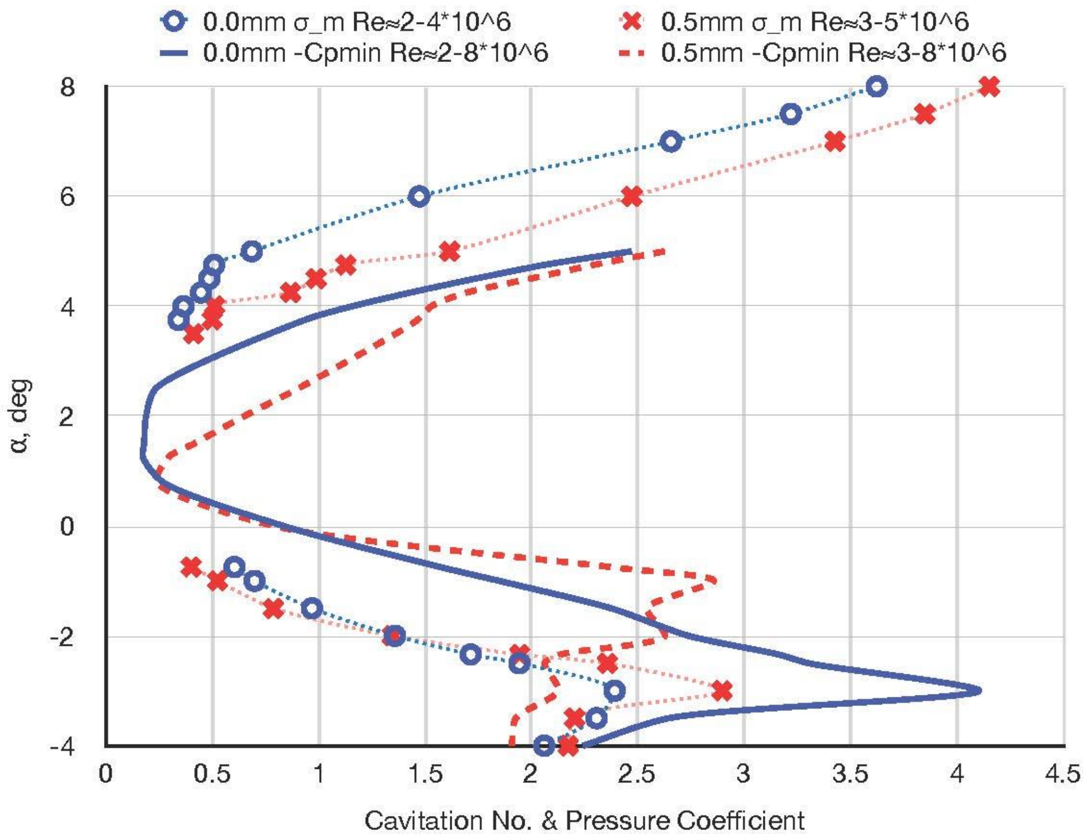


Figure 41: Experimental ($\sigma_m$ ) and CFD-predicted ($-Cp_{min}$) cavitation buckets for the “as-designed” (0.0mm defect) and “as-built” (0.5mm defect) foils.

The simple standard approximation against which cavitation results are compared is that cavitation inception occurs when the local pressure reaches the vapour pressure of water. That is when $\sigma_m = -Cp_{min}$. There are obvious differences between the experimental $\sigma_m$ results and the CFD predictions of $-Cp_{min}$ for both the "as-designed" and "as-built" foils. At this time the causes of the difference are not known but the following possibilities have been identified:

- The CFD predictions of pressure are wrong.
- Possible difference in the determination of $P_\infty$ between CFD and experiment.
- The observed cavitation does not represent the inception condition.
- The simple standard approximation does not adequately model cavitation inception for such foils

These possibilities form a basis for future investigation.

The experimental data gave well-defined cavitation buckets for both the "as-designed" and "as-built" foils models to the limits of the tunnel's abilities. The effects of the defect on the foil are clear. The defect substantially reduces the cavitation-free angle of attack for cavitation on the back. That reduction was predicted by the CFD but its magnitude was not so well predicted. The defect on the back also changes the cavitation-free angle of attack for cavitation on the face. These changes follow those predicted by the CFD. For angles of attack below -3°, flow separation effects are apparent and CFD results are not expected to be reliable there.

For angles of attack where cavitation is on the back of the foil (4° to 8°), the "as-built" portion of the foil model has a lower inception speed than the "as-designed" portion. This effect was predicted by the CFD for both the 2D section and the test foil (see Figure 32).

For angles of attack where cavitation is on the face of the foil (< 0°) there is a small range of angles (0° to -1.5°) where the "as-built" foil has a higher inception speed than the "as-designed" foil. Thit effect was predicted by CFD for both the 2D section and the test foil (see Figure 32).

The ratios of the "as-built" foil's cavitation inception speeds to that of the "as-designed" foil (the Inception Speed Ratios, ISR) are determined by the equation in Section 4.11 with the $Cp_{min}$ replaced by $\sigma_i$, $\sigma_d$ and $\sigma_m$ as appropriate. Table 11 gives relevant cavitation numbers at inception and desinence, ISR and PRCIS (percentage reduction in cavitation inception speed).

| Angle of attack | "As-designed" foil $\sigma_i$ min | $\sigma_i$ max | $\sigma_d$ min | $\sigma_d$ max | $\sigma_m$ | "As-built" foil $\sigma_i$ min | $\sigma_i$ max | $\sigma_d$ min | $\sigma_d$ max | $\sigma_m$ | ISR | PRCIS |
|---|---|---|---|---|---|---|---|---|---|---|---|---|
| -4.00 | 2.00 | 2.16 | 1.90 | 2.11 | 2.04 | 2.09 | 2.28 | 2.11 | 2.21 | 2.17 | 0.97 | 3% |
| -3.50 | 2.21 | 2.35 | 2.21 | 2.40 | 2.29 | 2.12 | 2.27 | 2.11 | 2.29 | 2.20 | 1.02 | -2% |
| -3.00 | 2.34 | 2.46 | 2.33 | 2.43 | 2.39 | 2.83 | 2.86 | 2.78 | 3.10 | 2.89 | 0.91 | 9% |
| -2.50 | 1.91 | 1.96 | 1.91 | 1.96 | 1.94 | 2.41 | 2.44 | 2.26 | 2.28 | 2.35 | 0.91 | 9% |
| -2.34 | 1.68 | 1.76 | 1.67 | 1.73 | 1.71 | 1.90 | 1.99 | 1.91 | 2.00 | 1.95 | 0.94 | 6% |
| -2.00 | 1.31 | 1.41 | 1.33 | 1.38 | 1.36 | 1.32 | 1.38 | 1.32 | 1.38 | 1.35 | 1.00 | 0% |
| -1.50 | 0.96 | 0.98 | 0.94 | 0.99 | 0.97 | 0.76 | 0.79 | 0.77 | 0.81 | 0.78 | 1.11 | -11% |
| -1.00 | 0.68 | 0.72 | 0.68 | 0.72 | 0.70 | 0.49 | 0.55 | 0.52 | 0.54 | 0.53 | 1.15 | -15% |
| -0.75 | 0.61 | 0.61 | 0.60 | 0.60 | 0.61 | 0.38 | 0.40 | 0.42 | 0.42 | 0.41 | 1.22 | -22% |
| 0.00 | | | | | | | | | | | | |
| 3.50 | | | | | | 0.41 | 0.42 | 0.39 | 0.42 | 0.41 | | |
| 3.75 | 0.32 | 0.35 | 0.35 | 0.37 | 0.35 | 0.47 | 0.52 | 0.50 | 0.51 | 0.50 | 0.83 | 17% |
| 4.00 | 0.33 | 0.39 | 0.33 | 0.40 | 0.36 | 0.47 | 0.54 | 0.47 | 0.54 | 0.51 | 0.85 | 15% |
| 4.25 | 0.42 | 0.45 | 0.46 | 0.46 | 0.45 | 0.85 | 0.90 | 0.82 | 0.90 | 0.87 | 0.72 | 28% |
| 4.50 | 0.45 | 0.48 | 0.50 | 0.51 | 0.49 | 0.97 | 0.98 | 1.00 | 1.00 | 0.99 | 0.70 | 30% |
| 4.75 | 0.50 | 0.51 | 0.49 | 0.53 | 0.51 | 1.12 | 1.13 | 1.12 | 1.14 | 1.13 | 0.67 | 33% |
| 5.00 | 0.65 | 0.70 | 0.68 | 0.71 | 0.69 | 1.61 | 1.63 | 1.58 | 1.64 | 1.62 | 0.65 | 35% |
| 6.00 | 1.44 | 1.48 | 1.46 | 1.51 | 1.47 | 2.43 | 2.49 | 2.46 | 2.51 | 2.47 | 0.77 | 23% |
| 7.00 | 2.64 | 2.68 | 2.64 | 2.66 | 2.66 | 2.66 | 3.38 | 3.42 | 3.48 | 3.24 | 0.91 | 9% |
| 7.50 | 3.18 | 3.19 | 3.25 | 3.26 | 3.22 | 3.84 | 3.90 | 3.80 | 3.86 | 3.85 | 0.91 | 9% |
| 8.00 | 3.64 | 3.68 | 3.54 | 3.63 | 3.62 | 4.13 | 4.22 | 4.10 | 4.16 | 4.15 | 0.93 | 7% |

Table 11: Cavitation Numbers at inception and desinence, ISR and PRCIS (percentage reduction in cavitation inception speed)

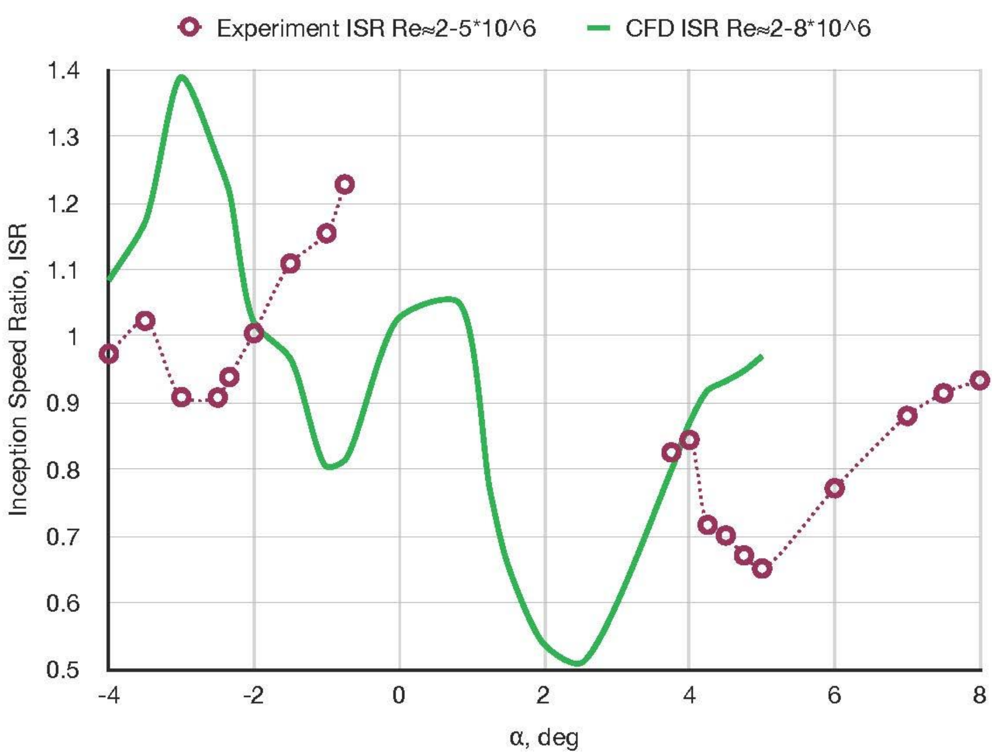


Figure 42: Inception Speed Ratio (ISR) vs. angle of attack for 2D foil model and CFD predictions

The major difference between the experiment and the CFD predictions is in the magnitude of the ISR (Figure 42). The minimum ISR for back cavitation is about 0.65 in the experiment and about 0.5 in the CFD prediction. The maximum ISR for face cavitation is about 1.13 in the experiment and about 1.5 in the CFD prediction. These differences are likely best illustrated by the percent reduction in cavitation inception speed (Figure 43).

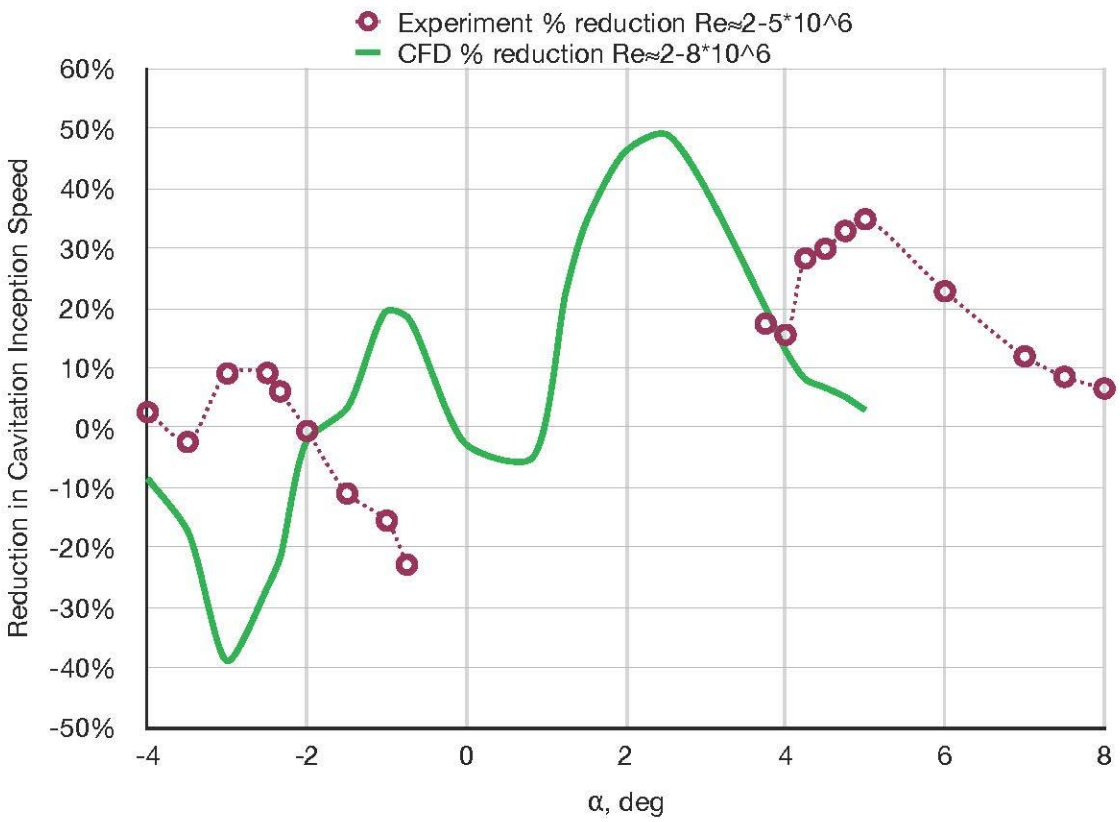


Figure 43: Percentage reduction in cavitation inception speed

The detrimental effects of the defect on inception speed found in the experiment are about one-half of those predicted by the CFD. Further, on the face for a limited range of angles, where the defect seems to provide some advantage, that advantage is about doubled. The detrimental effects are the more important and this experiment indicates that a defect allowed under the class S ISO-484 tolerances, could result in a 30% reduction in cavitation inception speed. By comparison, the CFD analysis indicates a 50% reduction.

Appendix F contains the photographs of cavitation inception on the "as-designed" (0.0 mm defect) and the "as-built" (0.5 mm defect) foil model in the cavitation tunnel. Please note that in the cavitation tunnel, the "as-designed" section of the 2D foil model was closer to the observation window than the "as-built" section.

## 6.0 CONCLUSIONS

Following conclusions can be drawn from the CFD simulations and experiments conducted in the cavitation tunnel:

- CFD calculations predict a reduction in the width of the cavitation bucket for a typical propeller blade section with a 0.5 mm defect on the leading-edge. This result provides a warning that such defects have the potential to cause earlier cavitation on propellers and that this subject requires further investigation.
- Cavitation inception was observed visually on models of perfect and defective versions of the typical propeller blade section. The maximum observed loss in cavitation inception speed due to a 0.5 mm defect on the leading-edge was 35%.
- The 0.5 mm defect tested is one of the tightest ISO 484 propeller manufacturing tolerances and it has been demonstrated experimentally that it affects cavitation inception significantly and detrimentally on a typical propeller blade section.

## 7.0 FUTURE WORK

### 1, Expand the investigation to a 3D wing planform

The cavitation inception speed reduction for sheet cavitation which was demonstrated in this study suggests that leading-edge defects of this and similar sizes will be of interest to ship-owners with requirements to maintain speed while limiting radiated noise. The investigation carried out so far is appropriate for foils of either the infinite span or ones with end-plates but always with its leading-edge perpendicular to the inflow. Propeller blades have leading-edges that range from perpendicular to the inflow, at the mid-span to aligned with the inflow, at the tip. That geometry can lead to both leading-edge vortex cavitation and tip vortex cavitation and the study of the effect of leading-edge defects on these seems a logical next step. A CFD and experimental program investigating the effects of defects within the ISO-484 that looks at the outer reaches of propeller blades is therefore proposed.

**2, Expand the investigation to defects of different sizes**

The scope of this investigation was limited to three leading-edge defects with sharp ends on the back of the 2D foil. Defects of different sizes and at different locations on the back and the face of the 2D foil should be analyzed for their effect on cavitation. Also, the effect of rounding the corners on the leading-edge defect should be investigated. A comprehensive study to determine what types of defects and at which locations on the section have the most detrimental effect on the cavitation performance of the section is therefore proposed.

**3, Validation of CFD**

There are many studies of the performance of 2D sections which are “as-designed” i.e. perfect in shape and we can say with confidence that CFD computation of pressure distributions for 2D sections has been validated. However, there are no validation data in the open literature for 2D sections with small LE defects such as those that we were studying. Measuring pressure on and around a 4 mm long flat LE defect on a 2D foil model presents the experimental team with several problems. CFD predicts a high-pressure peak at the fwd end of the defect and a smaller one at the aft end (see Figure 6). To measure the pressure peak accurately we would need to measure about 10 pressure points inside the length of 1 mm. Measuring pressure as it is traditionally done with pressure taps is not feasible because the minimum diameter of pressure taps available for wind tunnel or cavitation tunnel experiments is 0.5 mm. The use of PSP (Pressure Sensitive Paint) techniques to measure pressure was discussed with the researchers at the National Research Counsel’s (NRC) wind tunnel. At the moment the resolution of the system in use at NRC is not high enough for our application. However, the researchers at NRC are developing a new system that will have the resolution required for our application. This new capability at NRC’s wind tunnel will be available by early 2023. When the new capability is available at NRC, an experiment to validate the CFD on several different LE defects is therefore being proposed.

Dominis

## 8.0 REFERENCES


1. Southall, Brandon L., Scholik-Schlomer, Amy R., Hatch, Leila, Bergmann, Trisha, Jasny, Michael, Metcalf, Kathy, Weilgart, Lindy, and Wright, Andrew J.: “Underwater noise from large commercial ships – International Collaboration for Noise Reduction”, Encyclopedia of Maritime and Offshore Engineering. John Wiley and Sons Ltd., 2017.

2. “Shipping Noise and Marine Mammals. A Background Paper” Produced by Participants of the International Workshop on Shipping Noise and Marine Mammals Held By Okeanos: Foundation for the Sea, Hamburg, Germany, 21st – 24th April 2008. or website http://whitelab.biology.dal.ca/lw/publications/OKEANOS.%20Wright%20(ed)%202008.%20Shipping%20noise.pdf

3. AQUO Project no. 314227, WP 2: Noise sources, Impact of propeller noise on global URN, Task T2.5, D2.8, Rev. 1, 16 July 2015.

4. Carlton, John: “Marine Propellers and Propulsion”, Third Edition, Elsevier Ltd., 2012.

5. “Principles of Naval Architecture, Vol. II: Resistance, Propulsion and Vibration”, Second revision, SNAME, 1988.

6. Kerwin, Justin E. & Hadler, Jacques B.: “Propulsion”, SNAME 2010.

7. Janssen, André, Leever, Sylvia: “Propeller manufacture and tolerances”, Encyclopedia of Maritime and Offshore Engineering. John Wiley and Sons Ltd. 2017.

8. Beek, Teus van, Janssen, André: “An integrated design and production concept for ship propellers”. 34th WEGEMT at University of Delft, 19 - 23 June 2000.

9. ISO 484-1: 2015 (E). Shipbuilding – Ship screw propellers – Manufacturing tolerances – Part 1: Propellers of diameter greater than 2.5 m, 2015.

10. ISO 484-2: 2015 (E). Shipbuilding – Ship screw propellers – Manufacturing tolerances – Part 2: Propellers of diameter between 0.80 and 2.5 m inclusive, 2015.

11. NAVSEA, Standard Propeller Drawing no. 810-4435837, Rev. B, 2004.

12. Wiegant, W.W.: “Tolerances in propeller design and manufacturing”, Hydrodynamics of Ship and Propulsion Systems, Hovik, Norway March 20 – 25, 1977.

13. Cole, Gregory V., Vorus, William S., Kress, Robert F.: A rational approach to propeller manufacturing tolerances, SNAME Propellers ‘84 Symposium, Virginia Beach, May 15 – 16, 1984.

14. Kennedy, James L.: “Tolerance impact on B-series propellers”, Ottawa, January 2018. (Private communication)

15. Kennedy, James L.: “Tolerance impact on B-series propellers; Variation of design conditions”, Ottawa, April 2018. (Private communication)

16. Hally, David: “Preliminary calculation of the effect of geometric anomalies on the NACA-66 airfoil”, 24 Nov. 2017. (Private communication)

17. Hally, David: “The effect of manufacturing defects on propeller performance”, DRDC, DNPS brief, 20 February 2018.

18. Hally, David: “Specification of test cases for a study into the effects of propeller geometry variations”, DRDC D21-0201-04666.

19. Brockett, Terry: “Minimum pressure envelopes for modified NACA-66 sections with NACA a = 0.8 camber and Buships Type I and Type II sections”, DTMB Report no. 1780, February 1966.

20. J. Fujisawa, Y. Ukon, K. Kume, and H. Takeshi (2000) "Local Velocity Field Measurements around the KCS Model (SRI M.S. No. 631) in the SRI 400m Towing Tank", Ship Research Institute, Ministry of Transport, Japan, SPD Report No.00-003-2.

21. "KRISO Container Ship (KCS) [https://t2015.nmri.go.jp/kcs.html](https://t2015.nmri.go.jp/kcs.html) (access date 2021-03-24)

22. L. Larsson, F. Stern and V. Bertram (Eds.), (2002) "Gothenburg 2000, A Workshop on Numerical Ship Hydrodynamics", Chalmers University of Technology.

23. Hino, T. (2005). Proc. of CFD Workshop Tokyo 2005, Tokyo, Japan.

24. L. Larsson, F. Stern, M. Visonneau (Eds.), (2013) "Numerical Ship Hydrodynamics: An assessment of the Gothenburg 2010 workshop", Springer.

25. T. Hino, F. Stern, L. Larsson, M. Visonneau, N. Hirata, J. Kim (Eds.), (2021) "Numerical Ship Hydrodynamics: An Assessment of the Tokyo 2015 Workshop", Springer.

26. https://www.nmri.go.jp/institutes/fluid_performance_evaluation/cfd_rd/cfdws05/Detail/KCS/kcs_g&c.htm

27. Hally, David: "Grid dependence of RANS codes for flows past propeller blade sections", Defence R&D Atlantic, DRDC Atlantic TM 2008-262, 2009.

28. Jin, Shanqin, Zha, Ruosi, Peng, Heather, Qiu, Wei and Gospodnetic, S: "2D CFD studies on the effects of leading-edge propeller manufacturing defects on cavitation performance, SNAME Maritime Convention 2020, 29 Sept. – 2 Oct. 2020.

29. Gospodnetic, D. and Gospodnetic S.: "Integrated propeller manufacturing system"; Shipbuilding symposium "Sorta", Zagreb, Croatia, May 1996.

30. Gospodnetic, S.: "CNC milling of monoblock propellers to final form and finish", Ottawa Marine Technical Symposium, Ottawa, February 2013.

31. Gospodnetic, S.: "CNC machining of propellers to better than class S tolerances", SNAME 14th Propeller & Shafting Symposium, Norfolk, Virginia, Sept. 2015.

Dominis

## APPENDIX A: Impact of manufacturing tolerances on propeller performance Project overview

Project organization:

- Investigation 1: 2D foil section in the rectilinear flow
- Investigation 2: 3D wing planform in the rectilinear flow
- Investigation 3: 3D full propeller (rotating)

Project partners:

- Dominis Engineering: Project lead, coordination, managing experimental program, manufacturing of models and reporting
- Defence Research and Development Canada (DRDC) – Atlantic Research Centre: RANS CFD modelling
- Memorial University of Newfoundland (MUN): RANS CFD modelling
- Brodarski Institut, Zagreb, Croatia: Cavitation tunnel experiments for Investigation 1.

Project financing:

- Transport Canada Innovation Centre: Direct financial support to the project. (www.tc.gc.ca/en/initiatives/innovation-centre.html)
- DRDC – Atlantic Research Centre: In-kind support to the project (www.drdc-rddc.gc.ca)
- Mathematics of Information Technology and Complex Systems (MITACS): Financial support to MUN researchers. (www.mitacs.ca)
- Dominis Engineering Ltd.: In-kind and financial support to the project. (www.dominis.ca)

Project timeline:

| | |
|---|---|
| Preliminary investigation: | January 2016 – December 2018 |
| Project start: | January 2019 |
| Investigation 1: | January 2019 to March 2022 |
| Investigation 2: | April 2022 to TBD |
| Investigation 3: | TBD |

Dominis

## APPENDIX B: Coordinates of the NACA-66 section (a=0.8, t/c=0.0416, f/c=0.014)

| Chord (mm) | Back (mm) | Face (mm) |
|---|---|---|
| 0.000 | 0.216 | 0.000 |
| 0.313 | 0.862 | -0.557 |
| 0.625 | 1.190 | -0.802 |
| 1.250 | 1.672 | -1.132 |
| 2.500 | 2.387 | -1.562 |
| 5.000 | 3.447 | -2.114 |
| 7.500 | 4.293 | -2.492 |
| 12.500 | 5.689 | -3.028 |
| 25.000 | 8.384 | -3.844 |
| 50.000 | 12.443 | -4.774 |
| 75.000 | 15.668 | -5.366 |
| 100.000 | 18.404 | -5.804 |
| 150.000 | 22.891 | -6.422 |
| 200.000 | 26.446 | -6.846 |
| 250.000 | 29.225 | -7.085 |
| 300.000 | 31.831 | -7.205 |
| 350.000 | 32.980 | -7.225 |
| 400.000 | 34.057 | -7.150 |
| 450.000 | 34.621 | -6.975 |
| 500.000 | 34.632 | -6.652 |
| 550.000 | 34.109 | -6.209 |
| 600.000 | 33.052 | -5.664 |
| 650.000 | 31.437 | -5.030 |
| 700.000 | 29.239 | -4.339 |
| 750.000 | 26.406 | -3.655 |
| 800.000 | 22.799 | -3.095 |
| 850.000 | 18.160 | -2.931 |
| 900.000 | 12.860 | -2.778 |
| 950.000 | 7.172 | -2.350 |
| 975.000 | 4.271 | -1.960 |
| 1000.000 | 0.000 | 0.000 |

Coordinates according to Terry Brockett [19] with corrections by David Hally. Personal communication; D. Hally to S. Gospodnetic 2017.

Dominis

## Appendix C: Drawing of 2D foil model for cavitation tunnel testing

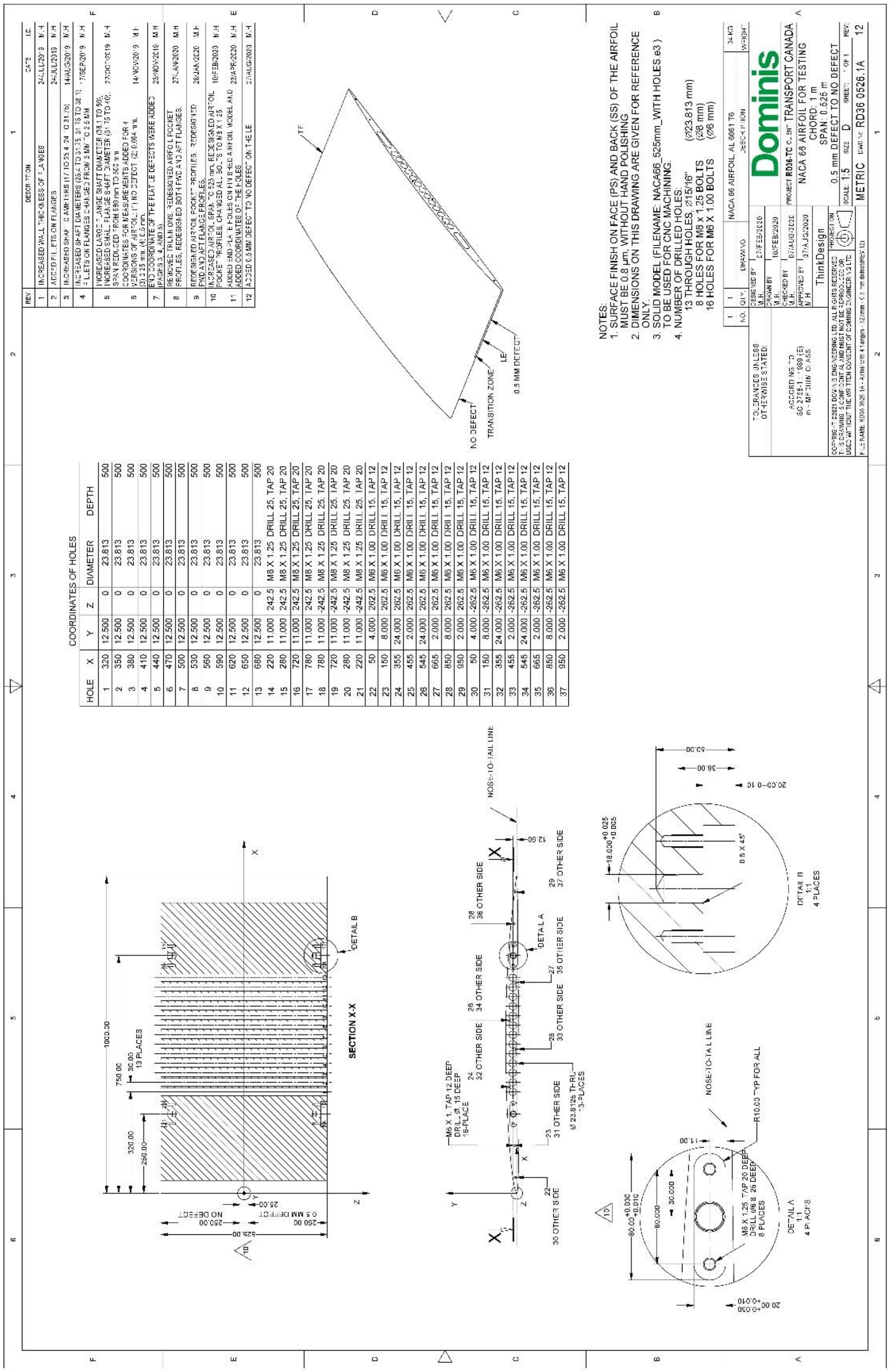

## Appendix D: Drawings of 2D foil model assembly for cavitation tunnel testing

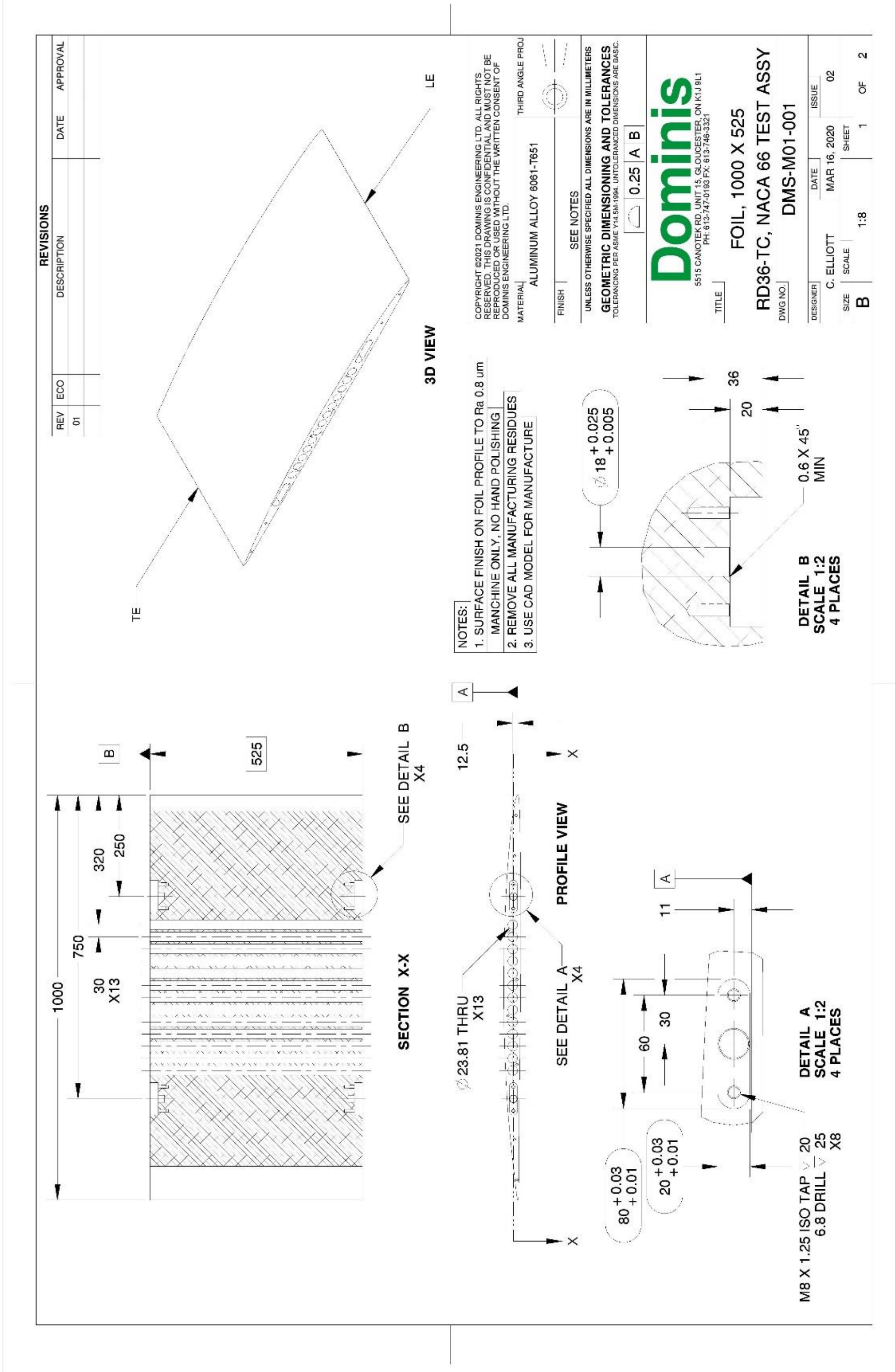

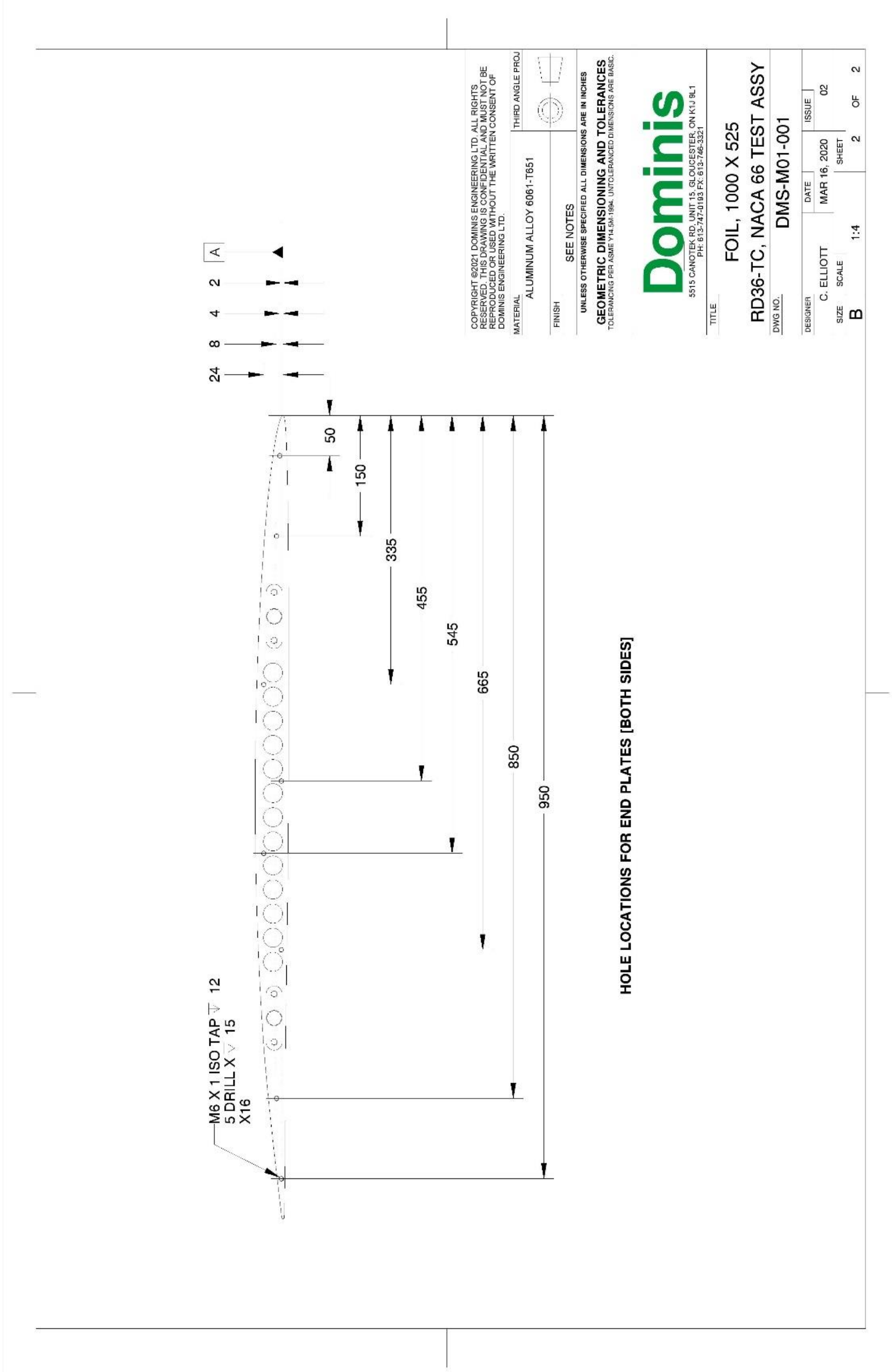
COPYRIGHT ©2021 DOMINIS ENGINEERING LTD. ALL RIGHTS RESERVED. THIS DRAWING IS CONFIDENTIAL AND MUST NOT BE REPRODUCED OR USED WITHOUT THE WRITTEN CONSENT OF DOMINIS ENGINEERING LTD.
MATERIAL
ALUMINUM ALLOY 6061-T651
THIRD ANGLE PROJ
FINISH
SEE NOTES
UNLESS OTHERWISE SPECIFIED ALL DIMENSIONS ARE IN INCHES
GEOMETRIC DIMENSIONING AND TOLERANCES
TOLERANCING PER ASME Y14.5M-1994. UNTOLERANCED DIMENSIONS ARE BASIC.
Dominis
5515 CANOTEK RD, UNIT 15, GLOUCESTER, ON K1J 9L1
PH: 613-747-0193 FX: 613-746-3321
TITLE
FOIL, 1000 X 525
RD36-TC, NACA 66 TEST ASSY
DWG NO.
DMS-M01-001
DESIGNER
C. ELLIOTT
DATE
MAR 16, 2020
ISSUE
02
SIZE
B
SCALE
1:4
SHEET
2
OF
2
24
8
4
2
A
50
150
335
455
545
665
850
950
M6 X 1 ISO TAP ↧ 12
5 DRILL X ↧ 15
X16
HOLE LOCATIONS FOR END PLATES [BOTH SIDES]

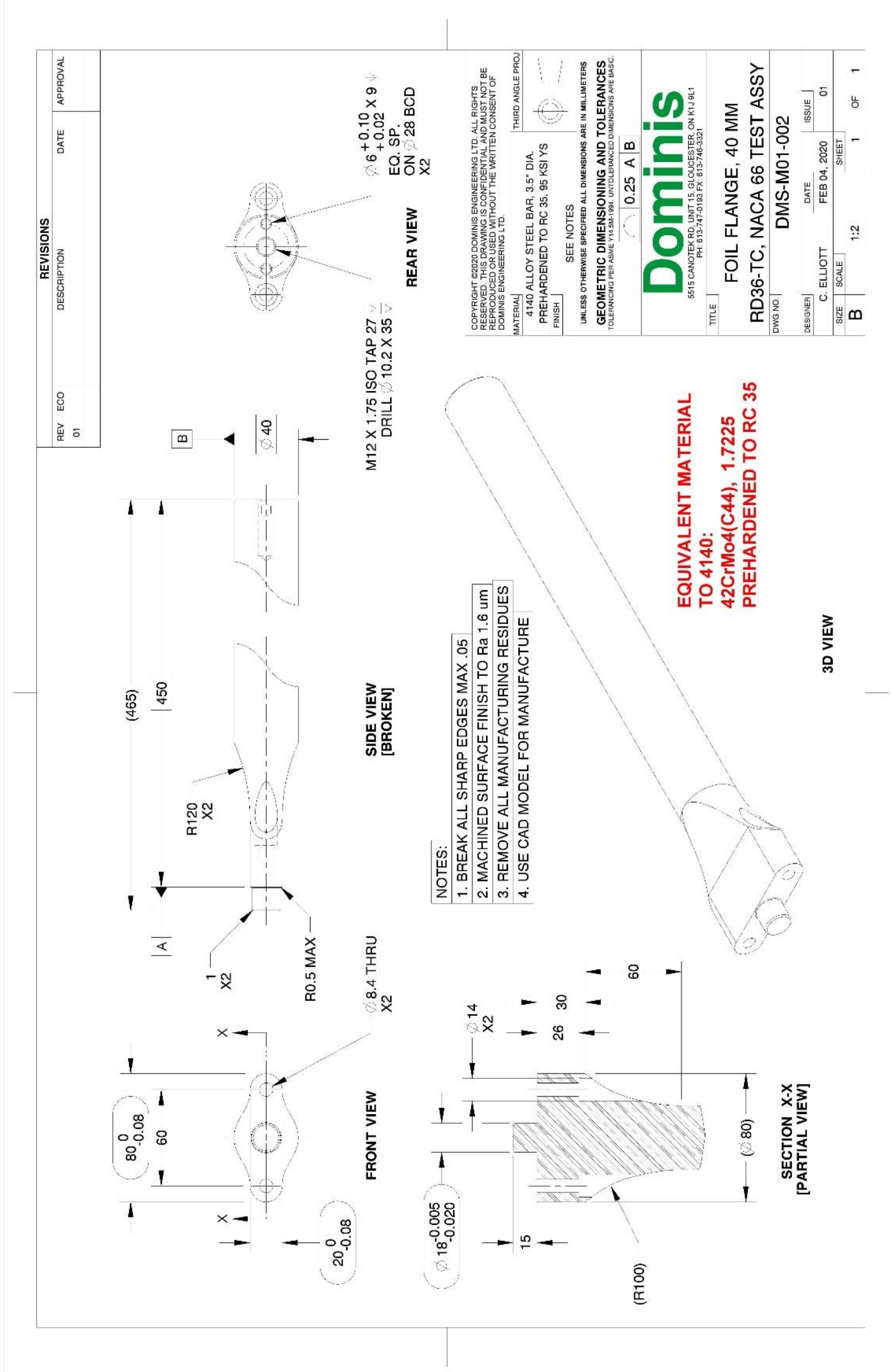
REVISIONS
REV ECO DESCRIPTION DATE APPROVAL
01
FRONT VIEW
SIDE VIEW [BROKEN]
REAR VIEW
3D VIEW
SECTION X-X [PARTIAL VIEW]
NOTES:
1. BREAK ALL SHARP EDGES MAX .05
2. MACHINED SURFACE FINISH TO Ra 1.6 um
3. REMOVE ALL MANUFACTURING RESIDUES
4. USE CAD MODEL FOR MANUFACTURE
EQUIVALENT MATERIAL TO 4140: 42CrMo4(C44), 1.7225 PREHARDENED TO RC 35
M12 X 1.75 ISO TAP 27
DRILL ⌀10.2 X 35
⌀8.4 THRU X2
R0.5 MAX
R120 X2
(465)
450
⌀40
(R100)
(⌀80)
4140 ALLOY STEEL BAR, 3.5" DIA.
PREHARDENED TO RC 35, 95 KSI YS
SEE NOTES
GEOMETRIC DIMENSIONING AND TOLERANCES
THIRD ANGLE PROJ
Dominis
5515 CANOTEK RD, UNIT 15, GLOUCESTER, ON K1J 9L1
FOIL FLANGE, 40 MM
RD36-TC, NACA 66 TEST ASSY
DMS-M01-002
C. ELLIOTT
FEB 04, 2020
SCALE 1:2
SIZE B

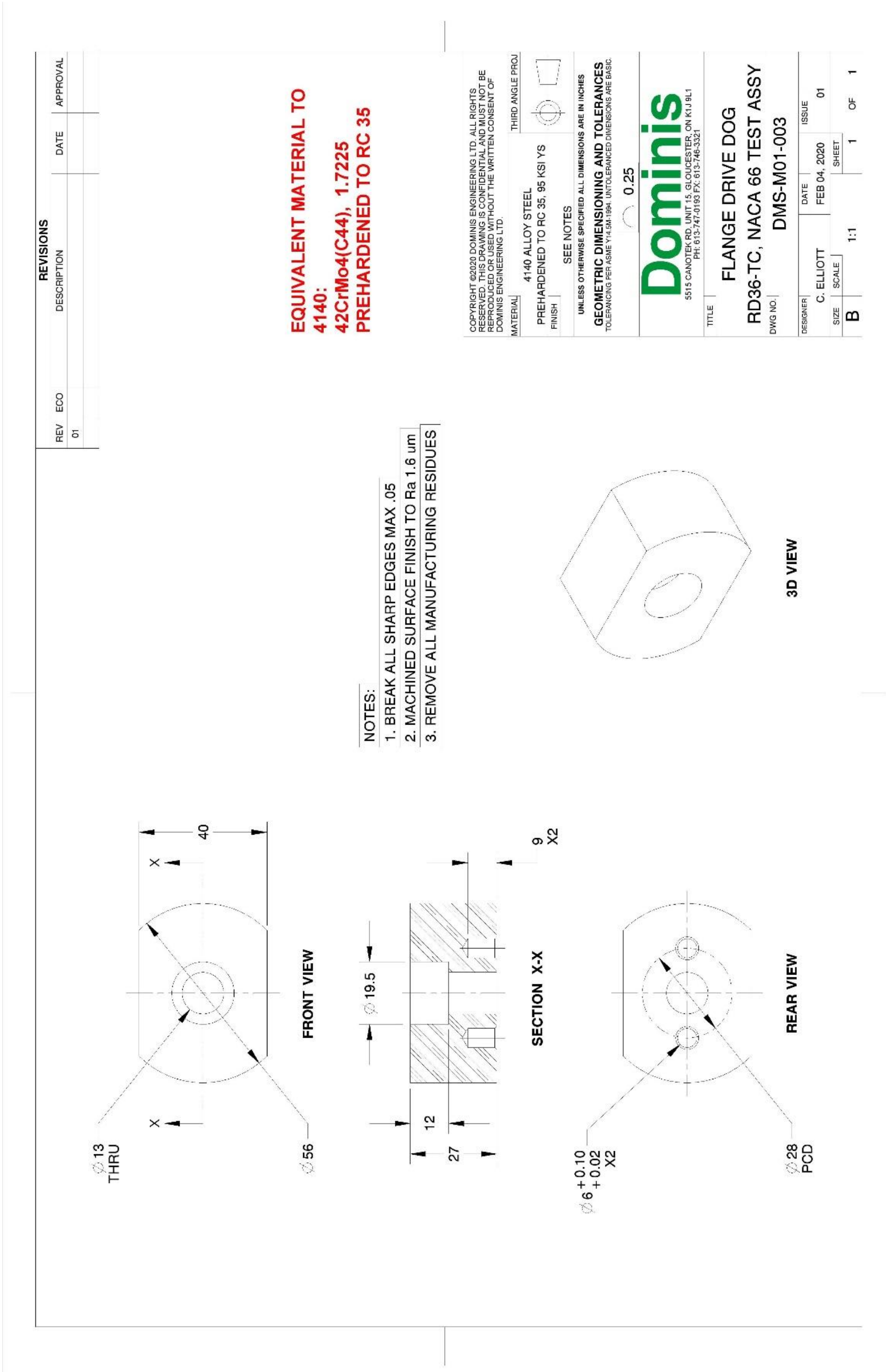
REVISIONS
REV ECO DESCRIPTION DATE APPROVAL
01
EQUIVALENT MATERIAL TO 4140:
42CrMo4(C44), 1.7225
PREHARDENED TO RC 35
NOTES:
1. BREAK ALL SHARP EDGES MAX .05
2. MACHINED SURFACE FINISH TO Ra 1.6 um
3. REMOVE ALL MANUFACTURING RESIDUES
3D VIEW
FRONT VIEW
SECTION X-X
REAR VIEW
⌀13 THRU
⌀56
40
⌀19.5
12
27
9 X2
⌀6 +0.10 +0.02 X2
⌀28 PCD
MATERIAL 4140 ALLOY STEEL
FINISH PREHARDENED TO RC 35, 95 KSI YS
SEE NOTES
THIRD ANGLE PROJ.
UNLESS OTHERWISE SPECIFIED ALL DIMENSIONS ARE IN INCHES
GEOMETRIC DIMENSIONING AND TOLERANCES
0.25
Dominis
5515 CANOTEK RD, UNIT 15, GLOUCESTER, ON K1J 9L1
PH: 613-747-0193 FX: 613-746-3321
TITLE
FLANGE DRIVE DOG
RD36-TC, NACA 66 TEST ASSY
DWG NO. DMS-M01-003
DESIGNER C. ELLIOTT
DATE FEB 04, 2020
ISSUE 01
SIZE B
SCALE 1:1
SHEET 1 OF 1

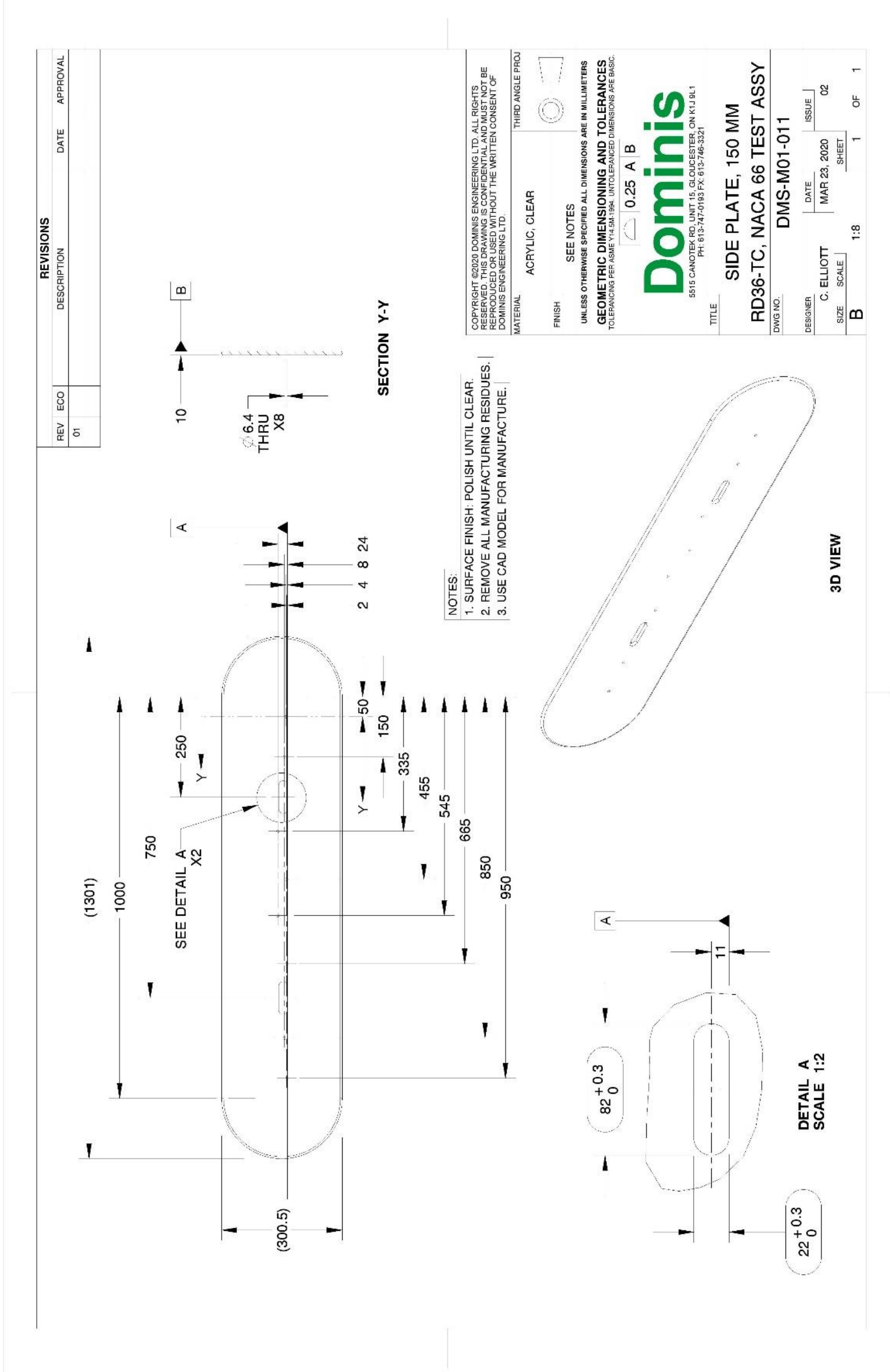
REVISIONS
REV
ECO
DESCRIPTION
DATE
APPROVAL
01
SECTION Y-Y
NOTES:
1. SURFACE FINISH: POLISH UNTIL CLEAR.
2. REMOVE ALL MANUFACTURING RESIDUES.
3. USE CAD MODEL FOR MANUFACTURE.
3D VIEW
DETAIL A
SCALE 1:2
SEE DETAIL A
X2
∅6.4
THRU
X8
COPYRIGHT ©2020 DOMINIS ENGINEERING LTD. ALL RIGHTS RESERVED. THIS DRAWING IS CONFIDENTIAL AND MUST NOT BE REPRODUCED OR USED WITHOUT THE WRITTEN CONSENT OF DOMINIS ENGINEERING LTD.
MATERIAL
ACRYLIC, CLEAR
FINISH
SEE NOTES
THIRD ANGLE PROJ.
UNLESS OTHERWISE SPECIFIED ALL DIMENSIONS ARE IN MILLIMETERS
GEOMETRIC DIMENSIONING AND TOLERANCES
Dominis
5515 CANOTEK RD, UNIT 15, GLOUCESTER, ON K1J 9L1
PH: 613-747-0193 FX: 613-746-3321
TITLE
SIDE PLATE, 150 MM
RD36-TC, NACA 66 TEST ASSY
DWG NO.
DMS-M01-011
DESIGNER
C. ELLIOTT
DATE
MAR 23, 2020
ISSUE
02
SIZE
B
SCALE
1:8
SHEET
1
OF
1

Dominis

## Appendix E: Observations and measurements recorded in the cavitation tunnel

### E1: Measurements for the "as-designed" (0.0 mm defect) 2D foil model

**NACA 66 Cavitation tunnel tests**
**Testes performed from 8 Sept. 19 to Dec. 2020**

**Prepared by Sanja Goles**
**Received 22 Jan. 2021**

| No defect start | | | | | |
|---|---|---|---|---|---|
| α [deg] | -Cpmin | $t_w$ [°C] | Δhp [mm] | p [Pa] | v [m/s] |
| -0.75 | | | | | |
| -0.75 | | | | | |
| -0.75 | 0.61 | 22.90 | 654.00 | 19,919 | 7.51 |
| | | | | | |
| -1.00 | 0.68 | 22.50 | 666.00 | 18,399 | 6.78 |
| -1.00 | 0.69 | 22.50 | 683.00 | 16,315 | 6.23 |
| -1.00 | 0.72 | 22.90 | 681.00 | 16,636 | 6.19 |
| -1.00 | 0.70 | 22.90 | 684.00 | 16,325 | 6.23 |
| -1.00 | 0.68 | 22.90 | 685.00 | 16,109 | 6.27 |
| | | | | | |
| -1.50 | 0.96 | 22.50 | 669.00 | 18,944 | 5.81 |
| -1.50 | 0.98 | 22.50 | 669.00 | 18,976 | 5.75 |
| -1.50 | 0.96 | 22.50 | 670.00 | 18,802 | 5.80 |
| -1.50 | 0.98 | 22.50 | 669.00 | 18,996 | 5.78 |
| | | | | | |
| -2.00 | 1.38 | 22.50 | 633.00 | 23,350 | 5.46 |
| -2.00 | 1.34 | 22.50 | 636.00 | 23,076 | 5.51 |
| -2.00 | 1.31 | 22.50 | 653.00 | 20,904 | 5.28 |
| -2.00 | 1.41 | 17.60 | 675.00 | 16,369 | 4.51 |
| | | | | | |
| -2.34 | 1.70 | 23.10 | 632.00 | 22,485 | 4.81 |
| -2.34 | 1.74 | 23.10 | 639.00 | 21,716 | 4.67 |
| -2.34 | 1.76 | 23.10 | 640.00 | 21,501 | 4.60 |
| -2.34 | 1.72 | 23.10 | 645.00 | 20,965 | 4.59 |
| -2.34 | 1.68 | 22.90 | 643.00 | 21,224 | 4.67 |
| | | | | | |
| | | | | | |
| -2.50 | 1.91 | 17.10 | 685.00 | 16,155 | 3.78 |
| -2.50 | 1.96 | 17.10 | 685.00 | 16,210 | 3.74 |
| -2.50 | 1.96 | 17.10 | 684.00 | 16,298 | 3.76 |
| | | | | | |
| -3.00 | 2.38 | 17.60 | 673.00 | 16,506 | 3.49 |
| -3.00 | 2.34 | 17.60 | 671.00 | 16,750 | 3.55 |
| -3.00 | 2.37 | 17.60 | 672.00 | 16,672 | 3.52 |
| -3.00 | 2.39 | 17.60 | 673.00 | 16,532 | 3.49 |
| -3.00 | 2.37 | 17.10 | 676.00 | 16,762 | 3.53 |
| -3.00 | 2.46 | 17.10 | 675.00 | 16,927 | 3.49 |
| -3.00 | 2.45 | 17.10 | 677.00 | 16,698 | 3.47 |
| -3.00 | 2.36 | 17.10 | 664.00 | 18,280 | 3.72 |
| -3.00 | 2.40 | 17.10 | 676.00 | 16,831 | 3.52 |
| -3.00 | 2.42 | 17.10 | 676.00 | 16,793 | 3.50 |

| No defect end | | | | | |
|---|---|---|---|---|---|
| α [deg] | -Cpmin | $t_w$ [°C] | Δhp [mm] | p [Pa] | v [m/s] |
| -0.75 | 0.60 | 22.90 | 654.00 | 19,957 | 7.56 |
| -0.75 | 0.60 | 22.90 | 656.00 | 19,727 | 7.54 |
| | | | | | |
| | | | | | |
| -1.00 | 0.71 | 22.50 | 658.00 | 20,394 | 7.06 |
| -1.00 | 0.72 | 22.50 | 654.00 | 20,838 | 7.13 |
| -1.00 | 0.68 | 22.90 | 667.00 | 18,375 | 6.79 |
| -1.00 | 0.70 | 22.90 | 664.00 | 18,727 | 6.74 |
| | | | | | |
| | | | | | |
| -1.50 | 0.99 | 22.50 | 667.00 | 19,267 | 5.77 |
| -1.50 | 0.94 | 22.50 | 671.00 | 18,778 | 5.85 |
| -1.50 | 0.95 | 22.50 | 670.00 | 18,855 | 5.82 |
| -1.50 | 0.98 | 22.50 | 668.00 | 19,149 | 5.78 |
| | | | | | |
| -2.00 | 1.33 | 22.50 | 636.00 | 23,037 | 5.52 |
| -2.00 | 1.38 | 22.50 | 633.00 | 23,405 | 5.47 |
| -2.00 | 1.36 | 22.50 | 650.00 | 21,329 | 5.24 |
| -2.00 | | | | | |
| | | | | | |
| -2.34 | | | | | |
| -2.34 | | | | | |
| -2.34 | 1.72 | 23.10 | 643.00 | 21,223 | 4.63 |
| -2.34 | 1.71 | 23.10 | 650.00 | 20,357 | 4.54 |
| -2.34 | 1.73 | 22.90 | 658.00 | 19,542 | 4.41 |
| -2.34 | 1.67 | 22.90 | 658.00 | 19,541 | 4.48 |
| | | | | | |
| -2.50 | | | | | |
| -2.50 | | | | | |
| -2.50 | | | | | |
| | | | | | |
| -3.00 | 2.34 | | | | |
| -3.00 | 2.33 | | | | |
| -3.00 | 2.33 | 17.10 | 677.00 | 16,636 | 3.56 |
| -3.00 | 2.33 | 17.10 | 678.00 | 16,533 | 3.54 |
| -3.00 | 2.42 | 17.10 | 674.00 | 16,979 | 3.51 |
| -3.00 | 2.43 | 17.10 | 677.00 | 16,706 | 3.49 |
| -3.00 | 2.39 | 17.10 | 663.00 | 18,429 | 3.72 |
| -3.00 | 2.42 | 17.10 | 665.00 | 18,086 | 3.66 |
| -3.00 | | | | | |
| -3.00 | | | | | |

Dominis

| No defect start | | | | | |
|---|---|---|---|---|---|
| α [deg] | -Cpmin | $t_w$ [°C] | Δhp [mm] | p [Pa] | v [m/s] |
| -3.50 | 2.23 | 17.60 | 672.90 | 16,571 | 3.62 |
| -3.50 | 2.21 | 17.60 | 671.30 | 16,770 | 3.66 |
| -3.50 | 2.35 | 17.60 | 668.00 | 17,171 | 3.60 |
| -3.50 | | | | | |
| -3.50 | 2.32 | 17.60 | 666.70 | 17,331 | 3.64 |
| -3.50 | 2.33 | 17.60 | 668.60 | 16,571 | 3.62 |
| -3.50 | 2.30 | 17.10 | 661.90 | 18,454 | 3.79 |
| -3.50 | 2.34 | 17.10 | 663.50 | 18,258 | 3.74 |
| -4.00 | 2.00 | 17.60 | 677.00 | 16,013 | 3.74 |
| -4.00 | 2.09 | 17.60 | 673.00 | 16,526 | 3.73 |
| -4.00 | 2.16 | 17.10 | 660.00 | 18,687 | 3.94 |
| -4.00 | 2.15 | 17.10 | 663.00 | 18,360 | 3.91 |
| -4.00 | 2.09 | 17.10 | 664.00 | 18,228 | 3.95 |
| | | | | | |
| | | | | | |
| 3.75 | 0.35 | 19.70 | 745.00 | 10,236 | 6.73 |
| 3.75 | 0.32 | 19.70 | 749.00 | 9,807 | 6.82 |
| 3.75 | 0.33 | 19.70 | 747.00 | 9,975 | 6.80 |
| 3.75 | 0.32 | 19.90 | 746.00 | 10,246 | 7.04 |
| 4.00 | 0.39 | 19.90 | 738.00 | 11,264 | 6.81 |
| 4.00 | 0.38 | 19.90 | 738.00 | 11,262 | 6.84 |
| 4.00 | 0.33 | 19.70 | 731.00 | 10,109 | 6.88 |
| 4.00 | 0.33 | 19.70 | 729.00 | 10,323 | 6.95 |
| 4.25 | 0.42 | 19.70 | 748.00 | 9,927 | 6.01 |
| 4.25 | 0.44 | 19.70 | 737.00 | 11,279 | 6.38 |
| 4.25 | 0.45 | 19.70 | 735.00 | 11,485 | 6.39 |
| 4.50 | 0.45 | 19.70 | 736.00 | 11,336 | 6.38 |
| 4.50 | 0.48 | 19.70 | 732.00 | 11,863 | 6.30 |
| 4.75 | 0.50 | 19.70 | 735.00 | 11,538 | 6.11 |
| 4.75 | 0.51 | 19.70 | 732.00 | 11,838 | 6.12 |
| 5.00 | 0.65 | 15.10 | 746.00 | 9,810 | 4.99 |
| 5.00 | 0.70 | 15.10 | 743.00 | 10,086 | 4.91 |
| 6.00 | 1.48 | 15.10 | 708.00 | 14,441 | 4.15 |
| 6.00 | 1.44 | 15.10 | 710.00 | 14,200 | 4.16 |

| No defect end | | | | | |
|---|---|---|---|---|---|
| α [deg] | -Cpmin | $t_w$ [°C] | Δhp [mm] | p [Pa] | v [m/s] |
| -3.50 | 2.21 | 17.60 | 670.90 | 16,815 | 3.66 |
| -3.50 | 2.30 | 17.60 | 667.20 | 17,267 | 3.65 |
| -3.50 | 2.27 | 17.60 | 668.80 | 17,075 | 3.64 |
| -3.50 | 2.35 | 17.60 | 664.50 | 17,609 | 3.65 |
| -3.50 | 2.37 | 17.60 | 666.20 | 17,396 | 3.60 |
| -3.50 | 2.33 | 17.10 | 658.30 | 18,893 | 3.82 |
| -3.50 | 2.40 | 17.10 | 649.80 | | 3.85 |
| -3.50 | 2.38 | 17.10 | 659.70 | 18,722 | 3.75 |
| -4.00 | 2.05 | 17.10 | 664.00 | 18,227 | 3.98 |
| -4.00 | 2.09 | 17.10 | 664.00 | 18,245 | 3.95 |
| -4.00 | 2.11 | 17.10 | 664.00 | 18,312 | 3.94 |
| -4.00 | 1.96 | 17.60 | 677.00 | 16,022 | 3.78 |
| -4.00 | 1.90 | 17.60 | 678.00 | 15,978 | 3.83 |
| | | | | | |
| | | | | | |
| 3.75 | | | | | |
| 3.75 | 0.37 | 19.70 | 742.00 | 10,657 | 6.69 |
| 3.75 | 0.35 | 19.70 | 745.00 | 10,270 | 6.75 |
| | | | | | |
| 4.00 | 0.35 | 19.70 | 723.00 | 11,038 | 6.80 |
| 4.00 | 0.33 | 19.70 | 730.00 | 10,206 | 6.96 |
| 4.00 | 0.40 | 19.90 | 736.00 | 11,556 | 6.76 |
| 4.00 | 0.40 | 19.90 | 736.00 | 11,508 | 6.77 |
| 4.25 | 0.46 | 19.70 | 740.00 | 10,948 | 6.17 |
| 4.25 | 0.46 | 19.70 | 734.00 | 11,617 | 6.35 |
| 4.25 | | | | | |
| 4.50 | 0.50 | 19.70 | 730.00 | 12,082 | 6.24 |
| 4.50 | 0.51 | 19.70 | 728.00 | 12,321 | 6.27 |
| 4.75 | 0.49 | 19.70 | 735.00 | 11,543 | 6.14 |
| 4.75 | 0.53 | 19.70 | 730.00 | 12,073 | 6.09 |
| 5.00 | 0.68 | 15.10 | 744.00 | 10,009 | 4.93 |
| 5.00 | 0.71 | 15.10 | 742.00 | 10,239 | 4.89 |
| 6.00 | 1.46 | 15.10 | 707.00 | 14,524 | 4.20 |
| 6.00 | 1.51 | 15.10 | 707.00 | 14,541 | 4.12 |

Dominis

| No defect start | | | | | |
|---|---|---|---|---|---|
| α [deg] | $-C_{pmin}$ | $t_w$ [°C] | Δhp [mm] | p [Pa] | v [m/s] |
| 7.00 | 2.64 | 15.10 | 682.00 | 17,705 | 3.48 |
| 7.00 | 2.68 | 15.10 | 680.00 | 17,854 | 3.47 |
| 7.50 | 3.18 | 15.10 | 666.00 | 19,671 | 3.36 |
| 7.50 | 3.19 | 15.10 | 665.00 | 19,758 | 3.36 |
| 8.00 | 3.68 | 15.10 | 651.00 | 21,510 | 3.28 |
| 8.00 | 3.67 | 15.10 | 649.00 | 21,742 | 3.31 |
| 8.00 | 3.64 | 15.10 | 653.00 | 21,234 | 3.28 |

| No defect end | | | | | |
|---|---|---|---|---|---|
| α [deg] | $-C_{pmin}$ | $t_w$ [°C] | Δhp [mm] | p [Pa] | v [m/s] |
| 7.00 | 2.66 | 15.10 | 680.00 | 17,863 | 3.49 |
| 7.00 | 2.64 | 15.10 | 681.00 | 17,753 | 3.49 |
| 7.50 | 3.25 | 15.10 | 663.00 | 19,989 | 3.36 |
| 7.50 | 3.26 | 15.10 | 664.00 | 19,896 | 3.34 |
| 8.00 | 3.58 | 15.10 | 650.00 | 21,601 | 3.34 |
| 8.00 | 3.54 | 15.10 | 652.00 | 21,322 | 3.33 |
| 8.00 | 3.63 | 15.10 | 653.00 | 21,245 | 3.28 |

Dominis

## E2: Measurements for the “as-built” (0.5 mm defect) 2D foil model

NACA 66 Cavitation tunnel tests
Tests performed from 8 Sept. to 19 Dec. 2020

Prepared by Sanja Goles
Received 22 Jan. 2021

| Defect start | | | | | |
|---|---|---|---|---|---|
| α [deg] | -Cpmin | $t_w$ [°C] | Δhp [mm] | p [Pa] | v [m/s] |
| -0.75 | 0.38 | 22.90 | 693.00 | 15,141 | 8.10 |
| -0.75 | 0.40 | 22.90 | 693.00 | 15,157 | 7.87 |
| -1.00 | 0.49 | 22.50 | 690.00 | 16,377 | 7.47 |
| -1.00 | 0.51 | 22.50 | 691.00 | 15,459 | 7.28 |
| -1.00 | 0.50 | 22.90 | 692.00 | 15,335 | 7.12 |
| -1.00 | 0.54 | 22.90 | 693.00 | 15,233 | 6.78 |
| -1.00 | 0.55 | 22.90 | 685.00 | 16,199 | 6.99 |
| -1.50 | 0.78 | 22.50 | 684.00 | 17,085 | 6.09 |
| -1.50 | 0.76 | 22.50 | 686.00 | 16,924 | 6.11 |
| -1.50 | 0.78 | 22.50 | 684.00 | 17,088 | 6.07 |
| -1.50 | 0.79 | 22.50 | 683.00 | 17,320 | 6.07 |
| -2.00 | 1.32 | 22.50 | 636.00 | 23,015 | 5.55 |
| -2.00 | 1.32 | 22.50 | 637.00 | 22,929 | 5.54 |
| -2.00 | 1.34 | 17.60 | 677.00 | 16,124 | 4.58 |
| -2.00 | 1.38 | 17.60 | 633.00 | 23,365 | 5.47 |
| -2.34 | 1.90 | 23.10 | 633.00 | 22,415 | 4.54 |
| -2.34 | 1.92 | 23.10 | 638.00 | 21,770 | 4.45 |
| -2.34 | 1.99 | 23.10 | 636.00 | 22,049 | 4.40 |
| -2.34 | 1.91 | 23.10 | 638.00 | 21,796 | 4.46 |
| -2.34 | 1.92 | 23.10 | 636.00 | 22,066 | 4.48 |
| | | | | | |
| -2.50 | 2.44 | 17.10 | 673.00 | 17,609 | 3.52 |
| -2.50 | 2.42 | 17.10 | 675.00 | 17,380 | 3.51 |
| -2.50 | 2.41 | 17.10 | 678.00 | 17,061 | 3.48 |
| -3.00 | 2.83 | 17.10 | 670.00 | 17,499 | 3.31 |
| -3.00 | 2.85 | 17.10 | 672.00 | 17,281 | 3.28 |
| -3.00 | 2.85 | 17.10 | 669.00 | 17,611 | 3.32 |
| -3.00 | 2.85 | 17.10 | 670.00 | 17,529 | 3.31 |
| -3.00 | 2.86 | 17.10 | 670.00 | 17,553 | 3.30 |
| -3.00 | | | | | |
| -3.00 | | | | | |
| -3.00 | | | | | |
| -3.00 | | | | | |
| -3.00 | | | | | |

| Defect end | | | | | |
|---|---|---|---|---|---|
| α [deg] | -Cpmin | $t_w$ [°C] | Δhp [mm] | p [Pa] | v [m/s] |
| -0.75 | 0.42 | 22.90 | 697.00 | 14,752 | 7.51 |
| | | | | | |
| -1.00 | 0.54 | 22.50 | 683.00 | 17,253 | 7.34 |
| -1.00 | 0.53 | 22.50 | 672.00 | 17,810 | 7.77 |
| -1.00 | 0.53 | 22.90 | 691.00 | 15,433 | 6.94 |
| -1.00 | 0.52 | 22.90 | 687.00 | 15,859 | 7.07 |
| | | | | | |
| -1.50 | 0.79 | 22.50 | 679.00 | 17,714 | 6.16 |
| -1.50 | 0.77 | 22.50 | 684.00 | 17,085 | 6.10 |
| -1.50 | 0.81 | 22.50 | 679.00 | 17,754 | 6.09 |
| -1.50 | 0.81 | 22.50 | 680.00 | 17,597 | 6.08 |
| -2.00 | 1.32 | 22.50 | 677.00 | 16,054 | 4.61 |
| -2.00 | 1.38 | 17.60 | 676.00 | 16,172 | 4.53 |
| -2.00 | 1.36 | 17.60 | 674.00 | 16,408 | 4.60 |
| | | | | | |
| -2.34 | 1.99 | 23.10 | 620.00 | 23,958 | 4.61 |
| -2.34 | 2.00 | 23.10 | 629.00 | 22,938 | 4.49 |
| -2.34 | 1.98 | 23.10 | 631.00 | 22,631 | 4.48 |
| -2.34 | 1.93 | 23.10 | 633.00 | 22,456 | 4.51 |
| -2.34 | 1.91 | 22.90 | 633.00 | 22,458 | 4.54 |
| -2.34 | 1.95 | 22.90 | 647.00 | 20,874 | 4.31 |
| -2.50 | 2.28 | 17.10 | 677.00 | 17,140 | 3.58 |
| -2.50 | 2.33 | 17.10 | 678.00 | 17,037 | 3.53 |
| -2.50 | 2.26 | 17.10 | 677.00 | 17,095 | 3.59 |
| -3.00 | 2.90 | 17.60 | 664.00 | 17,630 | 3.29 |
| -3.00 | 2.90 | 17.60 | 666.00 | 17,409 | 3.26 |
| -3.00 | 3.10 | 17.60 | 664.00 | 17,664 | 3.18 |
| -3.00 | 2.78 | 17.10 | 657.00 | 19,131 | 3.52 |
| -3.00 | 2.99 | 17.10 | 653.00 | 19,582 | 3.44 |
| -3.00 | 2.95 | 17.10 | 655.00 | 19,418 | 3.45 |
| -3.00 | | | | | |
| -3.00 | | | | | |
| -3.00 | | | | | |
| -3.00 | | | | | |

| Defect start | | | | | |
|---|---|---|---|---|---|
| α [deg] | -Cpmin | $t_w$ [°C] | Δhp [mm] | p [Pa] | v [m/s] |
| -3.50 | 2.13 | 17.60 | 676.10 | 16,173 | 3.65 |
| -3.50 | 2.12 | 17.60 | 673.70 | 16,477 | 3.70 |
| -3.50 | 2.27 | 17.60 | 669.60 | 16,978 | 3.63 |
| -3.50 | 2.21 | 17.60 | 664.10 | 17,652 | 3.77 |
| -3.50 | 2.19 | 17.60 | 668.20 | 17,146 | 3.72 |
| -3.50 | | | | | |
| -3.50 | 2.22 | 17.10 | 661.00 | 18,562 | 3.87 |
| -3.50 | 2.26 | 17.10 | 663.80 | 18,219 | 3.80 |
| -4.00 | 2.09 | 17.10 | 676.00 | 16,176 | 3.69 |
| -4.00 | 2.10 | 17.10 | 675.00 | 16,302 | 3.70 |
| -4.00 | 2.28 | 17.10 | 658.00 | 19,014 | 3.87 |
| -4.00 | 2.26 | 17.10 | 662.00 | 18,513 | 3.83 |
| -4.00 | 2.17 | 17.10 | 663.00 | 18,396 | 3.90 |
| 3.50 | 0.41 | 19.70 | 716.00 | 11,918 | 6.83 |
| 3.50 | 0.42 | 19.70 | 714.00 | 12,187 | 6.84 |
| 3.75 | 0.49 | 19.70 | 727.00 | 12,501 | 6.46 |
| 3.75 | 0.50 | 19.70 | 726.00 | 12,575 | 6.44 |
| 3.75 | 0.52 | 19.70 | 717.00 | 13,864 | 6.64 |
| 3.75 | 0.47 | 19.70 | 731.00 | 12,024 | 6.46 |
| 4.00 | 0.47 | 19.70 | 711.00 | 12,470 | 6.56 |
| 4.00 | 0.50 | 19.70 | 707.00 | 13,057 | 6.58 |
| 4.00 | 0.53 | 19.90 | 713.00 | 14,386 | 6.40 |
| 4.00 | 0.54 | 19.90 | 719.00 | 13,639 | 6.47 |
| 4.25 | 0.90 | 19.70 | 710.00 | 14,595 | 5.25 |
| 4.25 | 0.85 | 19.70 | 698.00 | 16,061 | 5.70 |
| 4.25 | 0.88 | 19.70 | 695.00 | 16,425 | 5.67 |
| 4.50 | 0.97 | 19.70 | 693.00 | 16,719 | 5.44 |
| 4.50 | 0.98 | 19.70 | 691.00 | 16,921 | 5.46 |
| 4.75 | 1.13 | 19.70 | 690.00 | 17,033 | 5.12 |
| 4.75 | 1.12 | 19.70 | 688.00 | 17,316 | 5.19 |
| 5.00 | 1.63 | 15.10 | 707.00 | 14,588 | 3.97 |
| 5.00 | 1.61 | 15.10 | 707.00 | 14,603 | 4.01 |
| 6.00 | 2.49 | 15.10 | 684.00 | 17,351 | 3.55 |
| 6.00 | 2.43 | 15.10 | 689.00 | 16,817 | 3.53 |

| Defect end | | | | | |
|---|---|---|---|---|---|
| α [deg] | -Cpmin | $t_w$ [°C] | Δhp [mm] | p [Pa] | v [m/s] |
| -3.50 | 2.11 | 17.60 | 673.50 | 16,492 | 3.71 |
| -3.50 | 2.18 | 17.60 | 671.90 | 16,691 | 3.67 |
| -3.50 | 2.16 | 17.60 | 670.70 | 16,845 | 3.71 |
| -3.50 | 2.21 | 17.60 | 666.80 | 17,316 | 3.72 |
| -3.50 | 2.28 | 17.60 | 667.40 | 17,242 | 3.66 |
| -3.50 | 2.27 | 17.60 | 661.90 | | 3.82 |
| -3.50 | | | | | |
| -3.50 | 2.29 | 17.10 | 662.10 | 18,420 | 3.80 |
| -4.00 | 2.14 | 17.10 | 675.00 | 16,342 | 3.66 |
| -4.00 | 2.11 | 17.10 | 672.00 | 16,732 | 3.73 |
| -4.00 | 2.17 | 17.10 | 662.00 | 18,540 | 3.91 |
| -4.00 | 2.20 | 17.10 | 662.00 | 18,544 | 3.89 |
| -4.00 | 2.21 | 17.10 | 661.00 | 18,596 | 3.88 |
| 3.50 | 0.39 | 19.70 | 719.00 | 11,483 | 6.88 |
| 3.50 | 0.42 | 19.70 | 713.00 | 12,246 | 6.84 |
| 3.75 | 0.50 | 19.90 | 720.00 | 13,460 | 6.66 |
| 3.75 | 0.51 | 19.70 | 726.00 | 12,629 | 6.39 |
| 3.75 | 0.50 | 19.70 | 725.00 | 12,740 | 6.44 |
| 3.75 | 0.50 | 19.70 | 725.00 | 12,777 | 6.50 |
| 4.00 | 0.49 | 19.70 | 708.00 | 12,911 | 6.61 |
| 4.00 | 0.47 | 19.70 | 710.00 | 12,624 | 6.65 |
| 4.00 | 0.54 | 19.90 | 718.00 | 13,690 | 6.49 |
| 4.00 | 0.54 | 19.90 | 717.00 | 13,826 | 6.51 |
| 4.25 | 0.82 | 19.70 | 707.00 | 14,913 | 5.55 |
| 4.25 | 0.86 | 19.70 | 697.00 | 16,209 | 5.69 |
| 4.25 | 0.90 | 19.70 | 694.00 | 16,548 | 5.64 |
| 4.50 | 1.00 | 19.70 | 689.00 | 17,172 | 5.47 |
| 4.50 | 1.00 | 19.70 | 689.00 | 17,106 | 5.46 |
| 4.75 | 1.12 | 19.70 | 688.00 | 17,283 | 5.17 |
| 4.75 | 1.14 | 19.70 | 687.00 | 17,380 | 5.16 |
| 5.00 | 1.58 | 15.10 | 707.00 | 14,555 | 4.03 |
| 5.00 | 1.64 | 15.10 | 706.00 | 14,733 | 3.99 |
| 6.00 | 2.51 | 15.10 | 686.00 | 17,205 | 3.51 |
| 6.00 | 2.46 | 15.10 | 690.00 | 16,733 | 3.50 |

| Defect start | | | | | |
|---|---|---|---|---|---|
| α [deg] | $-C_{pmin}$ | $t_w$ [°C] | Δhp [mm] | p [Pa] | v [m/s] |
| 7.00 | 2.66 | 15.10 | 680.00 | 17,863 | 3.49 |
| 7.00 | 3.38 | 15.10 | 674.00 | 18,592 | 3.16 |
| | | | | | |
| 7.50 | 3.84 | 15.10 | 660.00 | 20,393 | 3.12 |
| 7.50 | 3.90 | 15.10 | 658.00 | 20,586 | 3.11 |
| | | | | | |
| 8.00 | 4.22 | 15.10 | 643.00 | 22,500 | 3.14 |
| 8.00 | 4.13 | 15.10 | 647.00 | 21,931 | 3.13 |
| 8.00 | 4.21 | 15.10 | 646.00 | 22,116 | 3.11 |

| Defect end | | | | | |
|---|---|---|---|---|---|
| α [deg] | $-C_{pmin}$ | $t_w$ [°C] | Δhp [mm] | p [Pa] | v [m/s] |
| 7.00 | 3.42 | 15.10 | 672.00 | 18,896 | 3.17 |
| 7.00 | 3.48 | 15.10 | 672.00 | 18,921 | 3.15 |
| | | | | | |
| 7.50 | 3.80 | 15.10 | 660.00 | 20,406 | 3.14 |
| 7.50 | 3.86 | 15.10 | 660.00 | 20,312 | 3.11 |
| | | | | | |
| 8.00 | 4.10 | 15.10 | 646.00 | 22,096 | 3.15 |
| 8.00 | 4.16 | 15.10 | 647.00 | 21,959 | 3.12 |
| 8.00 | 4.10 | 15.10 | 650.00 | 21,655 | 3.12 |

## Appendix F: Photographs of cavitation inception observations on the 2D foil model at different angles of attack

The 2D foil model tested in the cavitation tunnel was composed of three sections: the “as-designed” section 250 mm in length, the transition section of 25 mm and the “as-built” section of 250 mm. When looking through the observation window of the cavitation tunnel, the “as-designed” section of the 2D foil model is closer to the observation window. Cavitation inception observations are documented with two photographs for each angle of attack. The upper photograph on the page shows the section of the 2D foil model where the cavitation was observed first, either “as-designed” or “as-built”. The lower photograph shows the 2D foil model where both the “as-designed” and the “as-built” sections are cavitating.

**The angle of attack: - 4°**

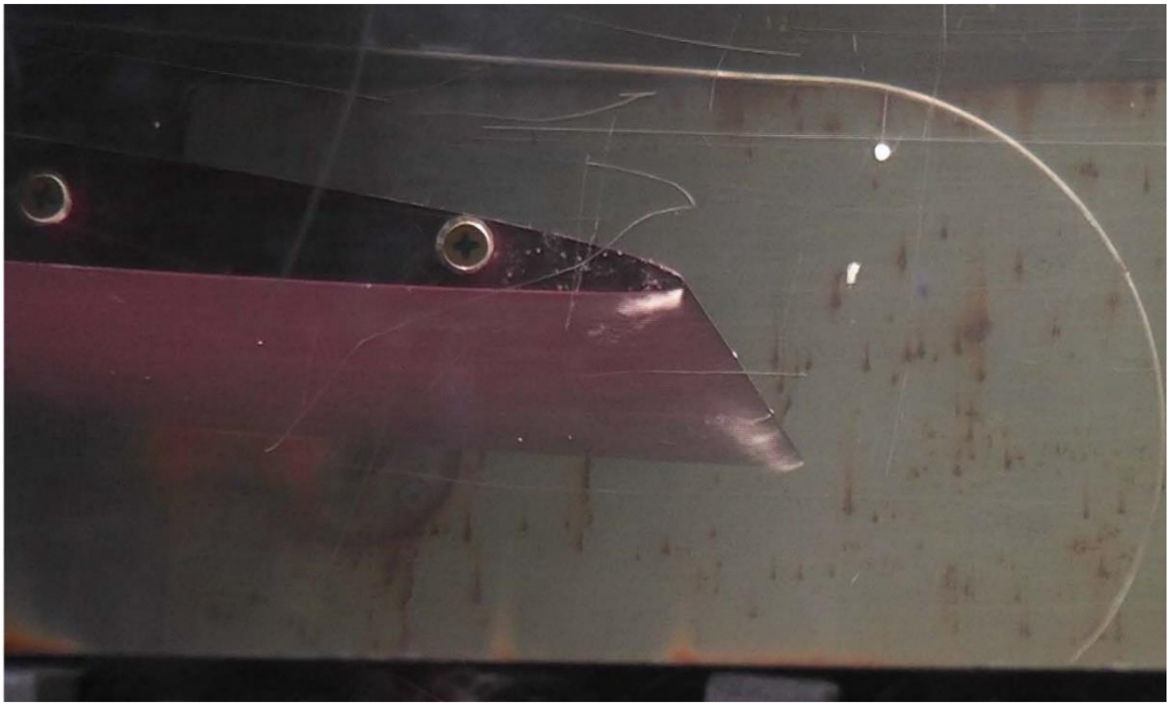

**The “as-built” section cavitates on the lower surface.** **$\sigma_m$ = 2.17**

**The “as-designed” section cavitates on the lower surface.** **$\sigma_m$ = 2.04**

Dominis

**The angle of attack:** **-3.5°**

**The "as-built" section cavitates on the lower surface.** **$\sigma_m$ = 2.20**

**The "as-designed" section cavitates on the lower surface.** **$\sigma_m$ = 2.29**

Dominis

**The angle of attack: -3.0°**

**The “as-built” section cavitates on the lower surface. $\sigma_m = 2.89$**

**The “as-designed” section cavitates on the lower surface. $\sigma_m = 2.39$**

**The angle of attack: -2.5°**

**The “as-built” section cavitates on the lower surface. $\sigma_m$ = 2.35**

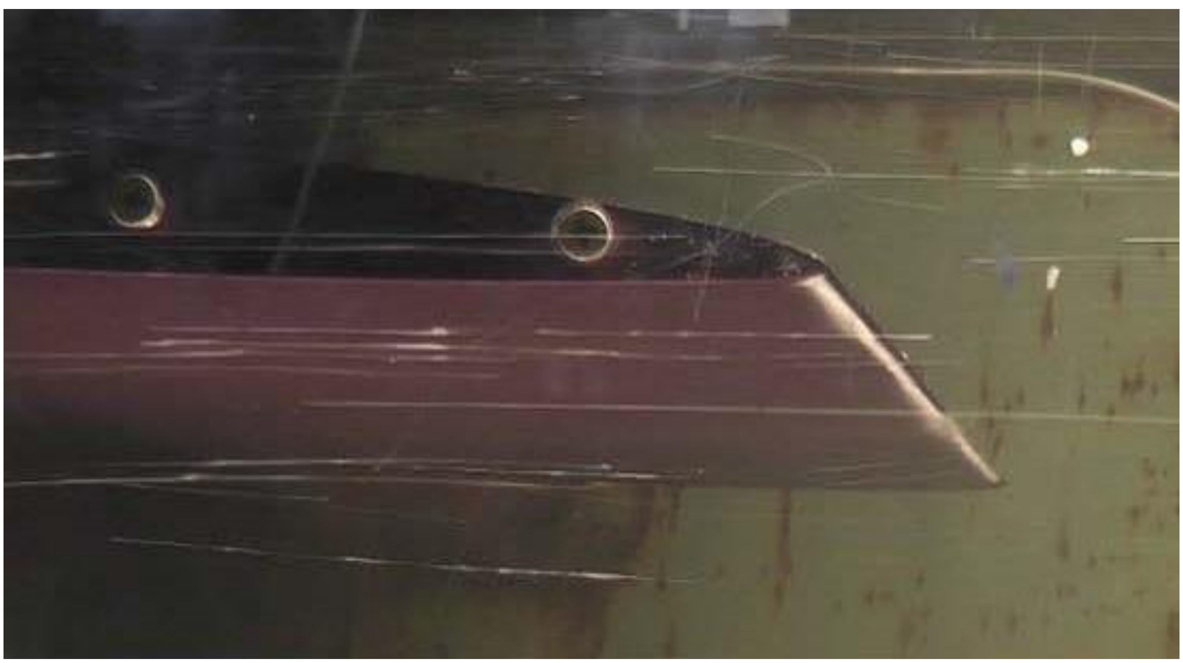

**The “as-designed” section cavitates on the lower surface. $\sigma_m$ = 1.94**

**The angle of attack: -2.0°**

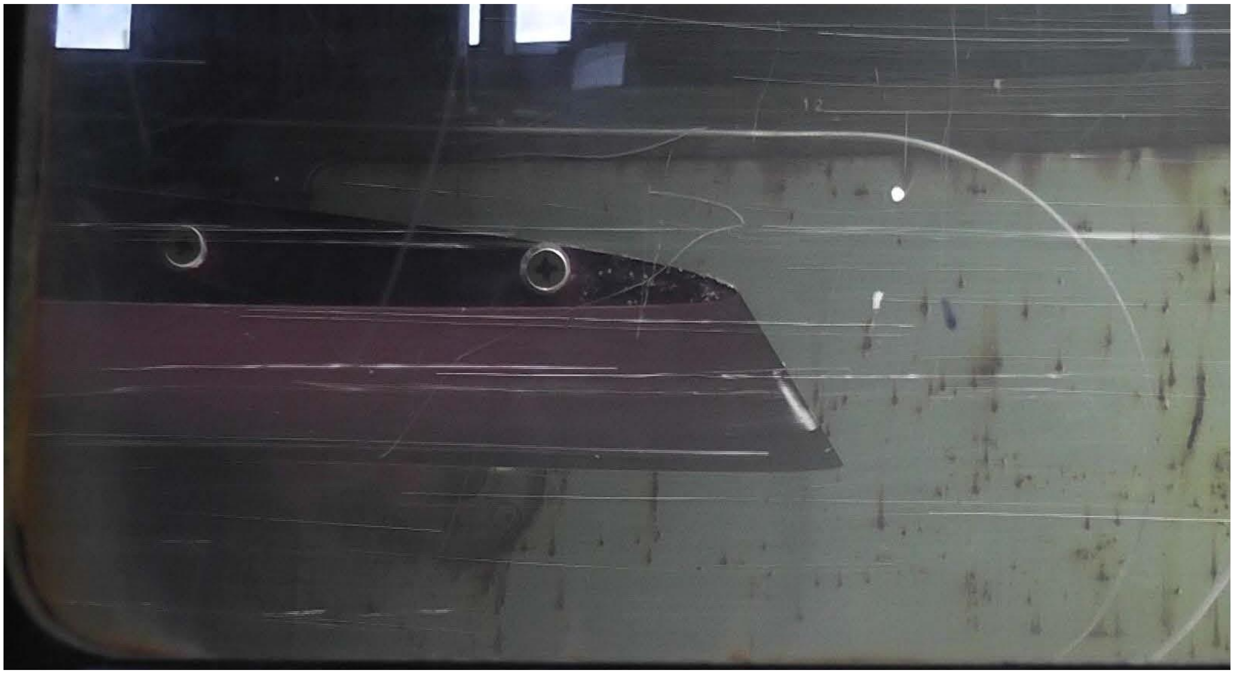

**The "as-built" section cavitates on the lower surface. $\sigma_m$ = 1.35**

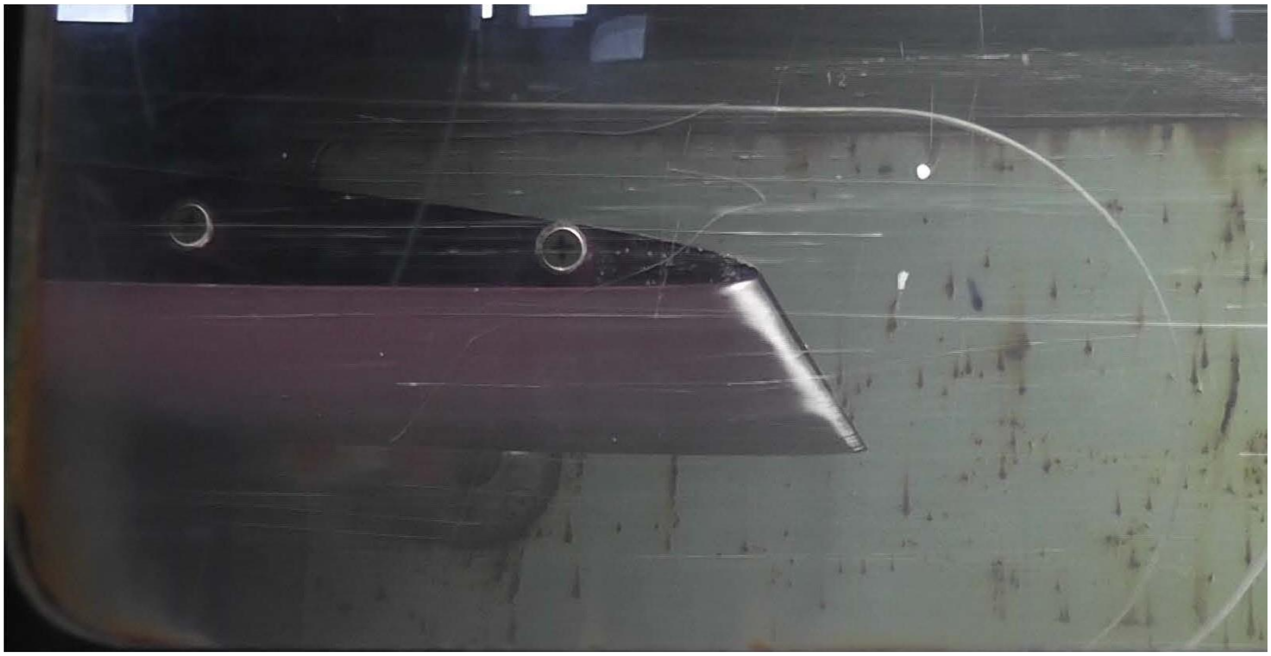

**The "as-designed" section cavitates on the lower surface. $\sigma_m$ = 1.36**

**The angle of attack: -1.0°**

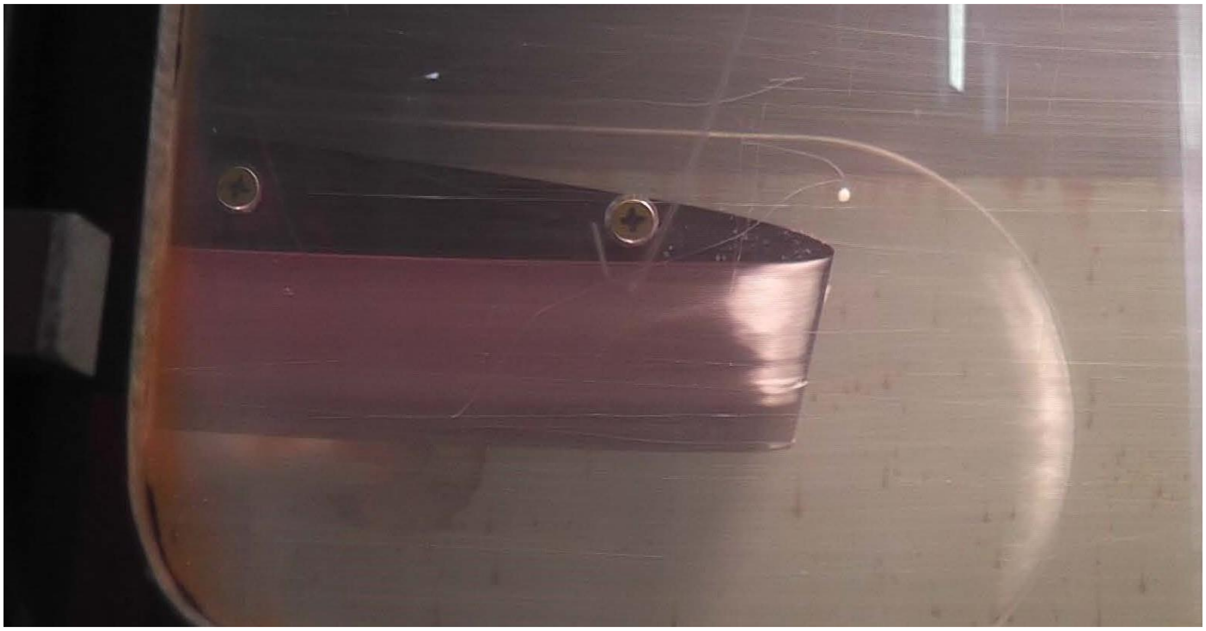

**The “as-designed” section cavitates on the lower surface. $\sigma_m$ = 0.70**

**The “as-built” section cavitates on the lower surface. $\sigma_m$ = 0.53**

Dominis

**The angle of attack: 3.5°**

**The "as-built" section cavitates on the upper surface. $\sigma_m = 0.41$**

**The "as-designed" section did not cavitate even at the lowest σ which can be obtained in the cavitation tunnel.**

Dominis

**The angle of attack: 4.0°**

**The "as-built" section cavitates on the upper surface. $\sigma_m$ = 0.51**

**The "as-designed" section cavitates on the upper surface. $\sigma_m$ = 0.36**

Dominis

**The angle of attack: +4.5°**

**The “as-built” section cavitates on the upper surface. $\sigma_m = 0.99$**

**The “as-designed” section cavitates on the upper surface. $\sigma_m = 0.49$**

Dominis

**The angle of attack: +5.0°**

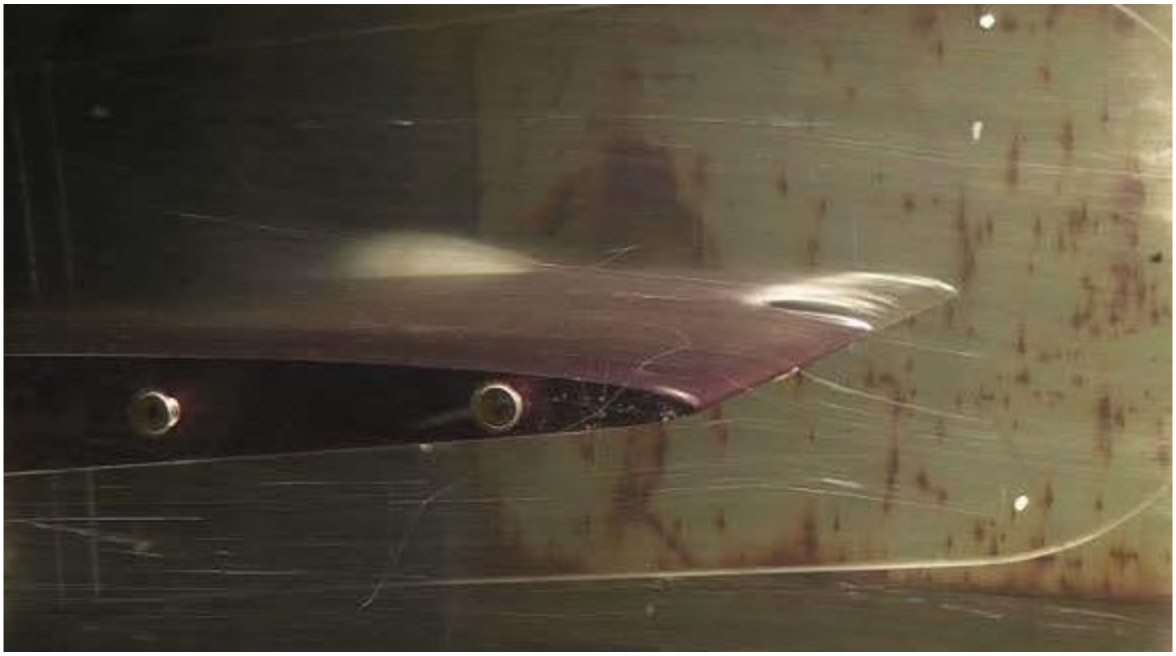

**The “as-built” section cavitates on the upper surface. $\sigma_m$ = 1.62**

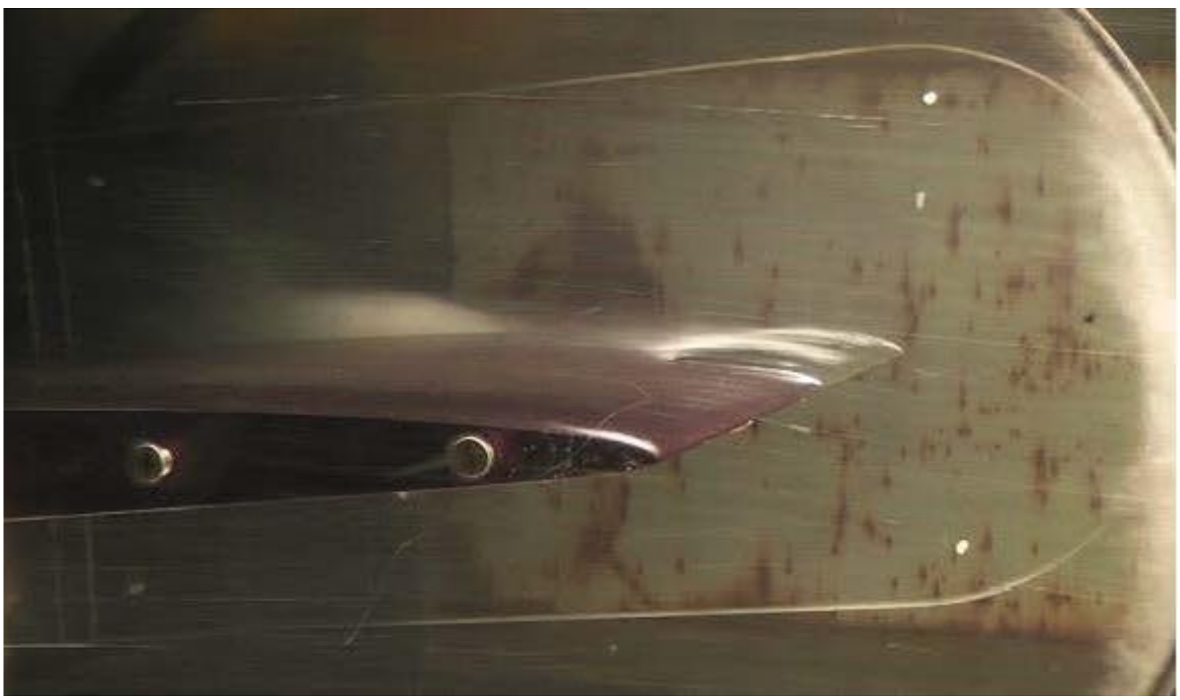

**The “as-designed” section cavitates on the upper surface. $\sigma_m$ = 0.69**

**The angle of attack: +6.0°**

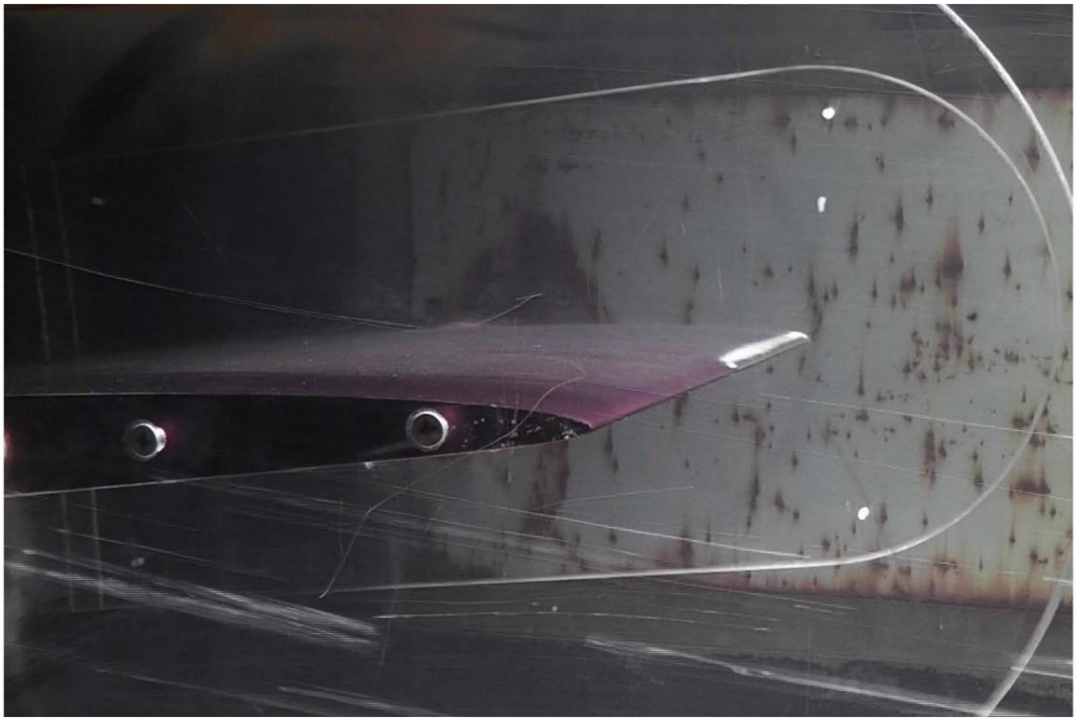

**The “as-built” section cavitates on the upper surface. $\sigma_m = 2.47$**

**The “as-designed” section cavitates on the upper surface. $\sigma_m = 1.47$**

**The angle of attack: +7.0°**

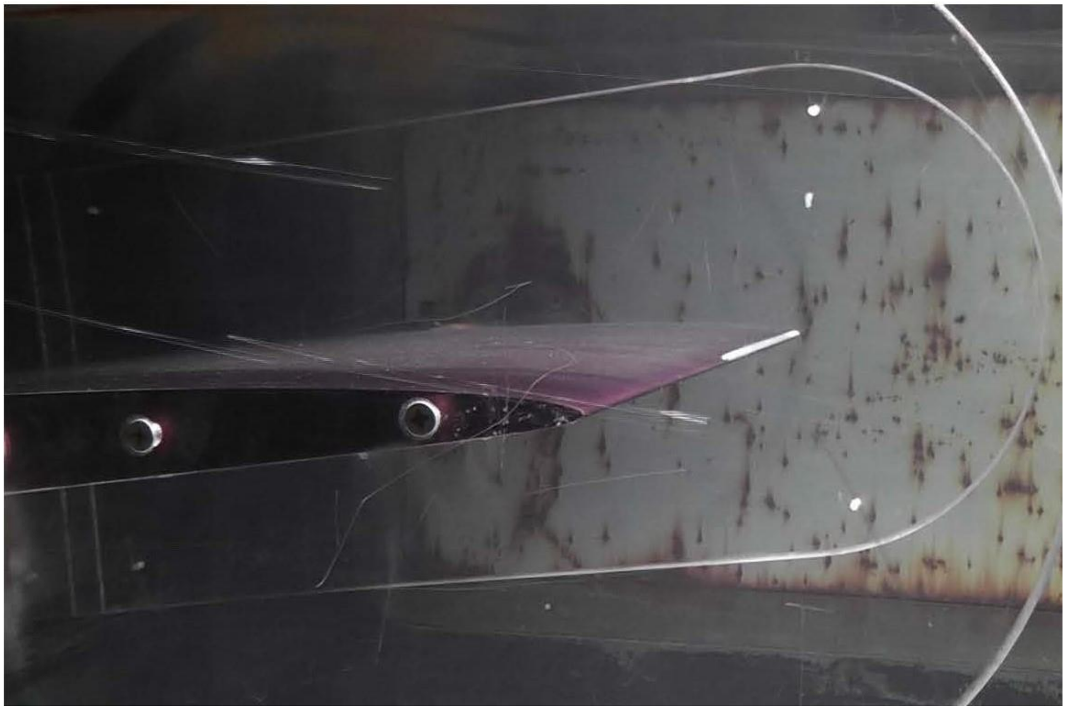

**The “as-built” section cavitates on the upper surface. $\sigma_m = 3.24$**

**The “as-designed” section cavitates on the upper surface. $\sigma_m = 2.66$**

**The angle of attack:** **+7.5°**

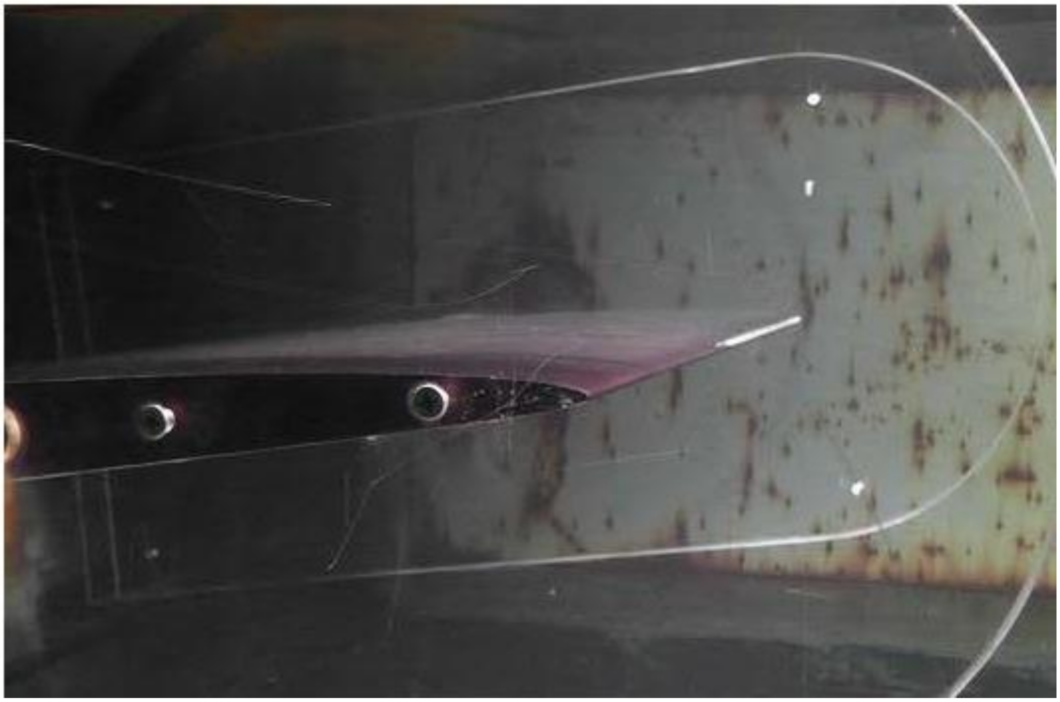

**The "as-built" section cavitates on the upper surface.** **$\sigma_m$ = 3.85**

**The "as-designed" section cavitates on the upper surface.** **$\sigma_m$ = 3.22**

**The angle of attack: +8.0°**

**The “as-built” section cavitates on the upper surface. $\sigma_m$ = 4.15**

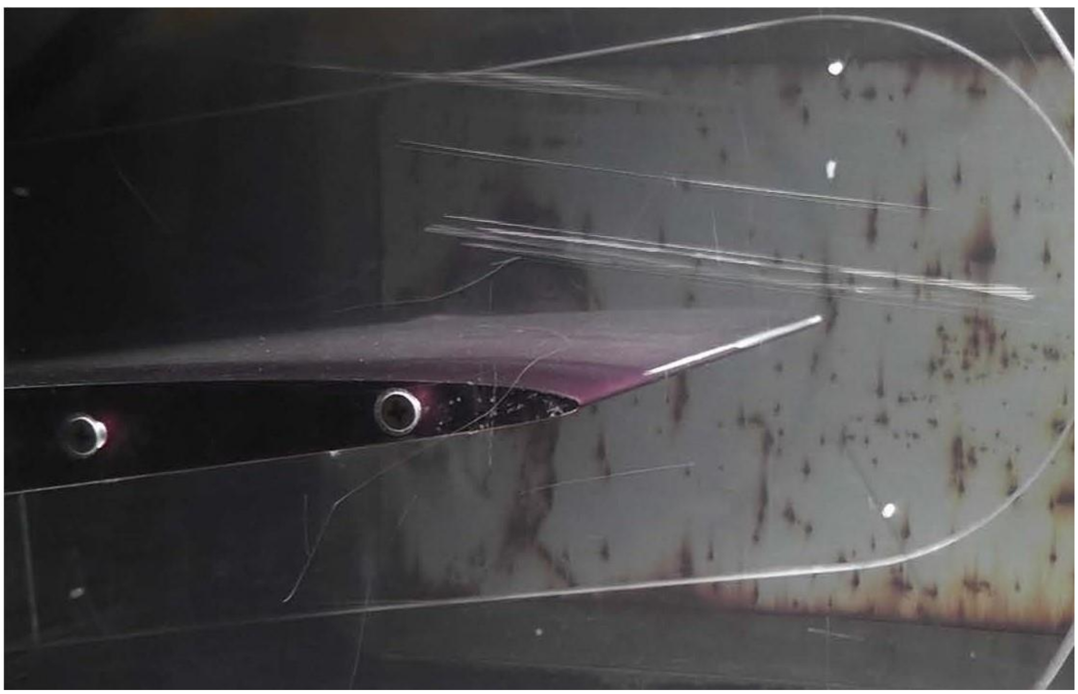

**The “as-designed” section cavitates on the upper surface. $\sigma_m$ = 3.62**

Dominis

**Table of Revisions**

| Rev. No. | Summary of Changes | ID | Date |
|---|---|---|---|
| 1 | Final draft | SG | 30 Mar. 2021 |
| 2 | Final draft, rev. 2 | SG | 8 Feb. 2022 |
| 3 | Final report | SG | 21 Mar. 2022 |